FUNCTIONAL POLYMER COMPOSITE ENCAPSULANTS FOR ELECTRONIC PACKAGING

A Dissertation
Presented to
The Academic Faculty

by

Chia-Chi Tuan

In Partial Fulfillment
of the Requirements for the Degree
Doctor of Philosophy in the
School of Materials Science and Engineering

Georgia Institute of Technology
August 2017

FUNCTIONAL POLYMER COMPOSITE ENCAPSULANTS FOR ELECTRONIC PACKAGING

Approved by:

Dr. Ching-Ping Wong, Advisor
School of Materials Science and Engineering
Georgia Institute of Technology

Dr. Gleb Yushin
School of Materials Science and Engineering
Georgia Institute of Technology

Dr. Zhong Lin Wang
School of Materials Science and Engineering
Georgia Institute of Technology

Dr. John Zhang
School of Chemistry and Biochemistry
Georgia Institute of Technology

Dr. Donggang Yao
School of Materials Science and Engineering
Georgia Institute of Technology

Date Approved: July 10, 2017

To My Family

ACKNOWLEDGEMENTS

I would like to thank my advisor Professor C. P. Wong for the guidance, support and encouragements during my PhD study. I would like to extend my gratitude to my thesis committee members Professor Zhong Ling Wang, Professor Donggang Yao, Professor Gleb Yushin, and Professor John Zhang for providing their critical opinions and suggestions.

I would like to express my gratitude to my current and previous group members including, Dr. Kyoung- Sik Moon, Dr. Yagang Yao, Dr. Yan Liu, Dr. Ziyin Lin, Dr. Zhuo Li, Dr. Zhenkun Wu, Dr. Liyi Li, Mr. Bo Song, Ms. Fan Wu, Dr. Gang Lian, Mr. Cheng Zhang, Dr. Yun Chen, Dr. Pengli Zhu, Dr. Xin Fang, Dr. Pin Hao, Dr. Chia-Yun Chen, Dr. Jakob Gakkestad, Mr. Nathan James, Mr. Jinho Hah, Ms. Maddy Shelton, Ms. Ashanti Turner, Mr. Randy Cheng, and Ms. Shuchen Zhang, for their collaborations, suggestions, and assistance. I would also like to thank my collaborators including Professor Rao Tummala, Dr. Raj Pulugartha, Dr. Vanessa Smet, Dr. Yong Ding, Dr. Ting-Chia Huang, Dr. Sehoon Yoo, Mr. Tae-Young Lee, Dr. Jong-Hyun Choi, Mr. Eun-Soo Ko, Professor Menos Tentzeris, Dr. Taoran Le, and Mr. Chinmay Honrao. I would also like to thank industry liaisons Dr. Yonghao Xiu and Dr. Ravi Mahajan of Intel Corporation for their technical suggestions.

I would like to extend my gratitude to the staff at Institute of Electronics and Nanotechnology and the Materials Characterization Facility at Georgia Tech, including Dr. Walter Henderson, Mr. David Tavakoli, Mr. Eric Woods, Mr. Todd Walters, Mr. Charlie

Suh, Mr. Chris Yang, Ms. Juna Zhang, Mr. John Pham, Mr. Tran-Vinh Nguyen, Ms. Jie Xu, Mr. Chris White, and Mr. Jason Bishop for their technical training and consultancy.

I am grateful to would like to Semiconductor Research Corporation, Korea Institute for Advancement of Technology, Packaging Research Center at Georgia Tech for funding my study.

Finally, I would like to thank my parents, my brother, and my fiancé for their love and support, without which this thesis would not have been possible.

TABLE OF CONTENTS

LIST OF TABLES

LIST OF FIGURES

LIST OF SYMBOLS AND ABBREVIATIONS

cP	Centipoise
CSP	Chip-scale package
CTE	Coefficient of thermal expansion
DMA	Dynamic mechanical analyzer
DSC	Differential scanning calorimetry
K	Kelvin
nm	Nanometer
ppm	Parts per million
RI	Refractive index
RT	Room temperature
SH	Superhydrophobic
T_g	Glass transition temperature
TGA	Thermogravimetric analyzer
TMA	Thermomechanical analyzer

XRD	X-ray diffraction
µm	Micrometer

SUMMARY

Polymer-based materials have attracted more and more interests in recent years for fundamental studies and for practical applications, for they combine material benefits of both the polymer matrix and the inorganic filler. In electronic packages, polymer composites are commonly used for the applications of molding compounds, underfills, and encapsulants using their mechanical, thermomechanical, and optical properties. This thesis is mainly focused on the understanding and applications of nanocomposite materials in electronic packaging.

First, high refractive index, silicone-based LED encapsulants were fabricated by incorporating TiO_2 nanoparticles. The surfaces of nanoparticles were modified with silane surfactants during and after nanoparticle syntheses, and the method of surface modification significantly affected the particle dispersion and size control, both of which were shown to be correlated to the optical performance of nanocomposite encapsulants. Encapsulant with refractive index > 1.7 and relative transmittance > 90% was demonstrated, and the nanocomposite also showed resistance to thermal cycling degradation under high humidity conditions.

Expanding from the study of filler dispersion, the interface between filler and polymeric matrix was further investigated in silica-epoxy nanocomposites for underfill application. A two-layer silica surface modification method was employed, where the inner layer served as coupling agent and the outer polysiloxane layer served to absorb stress and toughen the nanocomposite. Compared to unmodified or silane-modified silica, the two-layer modified silica fillers also showed improved interphase properties as shown in

thermomechanical and mechanical properties, including higher glass transition temperatures, lower thermal expansion in the underfills, and stronger silica-epoxy adhesion.

With the understanding of underfill composition and properties, we further explored methods to control the flow of nanocomposite underfill and to reduce filler entrapment in solders for 3D IC packaging. Fluid control on hydrophobic/hydrophilic patterned surfaces were simulated to determine the critical contact angles the surface. Superhydrophobic Cu bond pads and hydrophilic Si_3N_4 were fabricated according to the computational analyses. Self-patterning of underfill was demonstrated, as well as the interconnection bonding using the superhydrophobic Cu. Filler entrapment is shown to be reduced using this technology for enhanced interconnect reliability.

CHAPTER 1. INTRODUCTION

1.1 Overview of electronic packaging

Ever since 1947, when the first transistor was invented at Bell Labs, semiconductor technology has developed and transformed enormously. Transistors with large size and high cost have developed into highly integrated circuits (ICs) with much smaller size and lower cost. The number and complexity of the functionalities in semiconductor devices have also increased significantly over the years. In today's modern world, electronic products have become increasingly important and can be found in every aspect of daily life, from simple calculators to computers, mobile phones, and autonomous cars.

Electronic packaging, defined as the bridge that interconnects IC and other components into a system-level board to form electronic products, plays an important role in microelectronics through the following four functions [1]:

- Power distribution, providing an electrical path to power the circuits and mainly concerns electromagnetic, structural, and material aspects.
- Signal distribution, including topological and electromagnetic aspects.
- Thermal management, dissipating the heat generated by the circuits via structural and material considerations.
- Environmental protection, including mechanical, chemical, and electromagnetic protections.
- Design and test, to make sure the desired functions work properly.

From bare silicon chip to the final product, electronic packaging can be divided into four levels, from as shown in Figure 1-1:

- Level 0: semiconductor chip (IC)
- Level 1: an IC chip is assembled into a package carrier (substrate or lead frame) with interconnection materials using wire bonding, tape automated bonding, or flip chip assembly methods. The IC chip is protected by a lid or encapsulated with molding compound.
- Level 2: the packaged IC chip is mounted to a printed circuit board (PCB) or other types of substrates.
- Level 3: board to board interconnections.

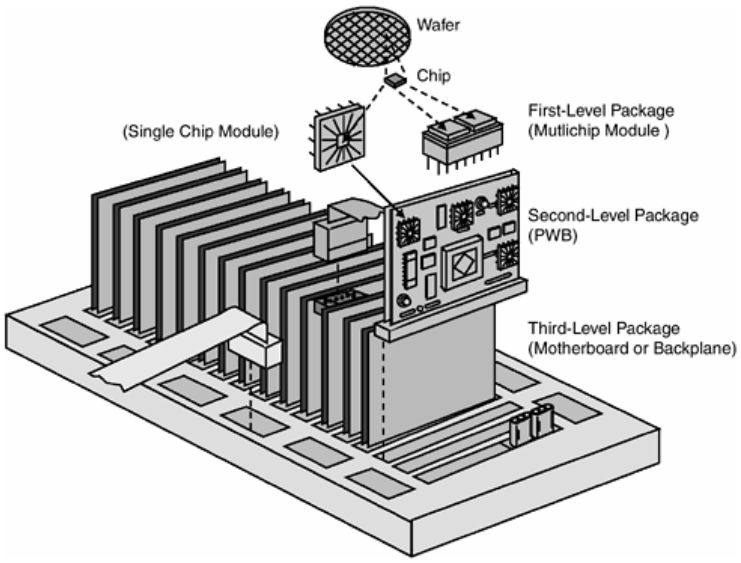

Figure 1-1. Levels of electronic packaging [2].

As electronics have evolved over the years in the areas of computation, telecommunication, automotive, and consumer electronics towards high performance, low

cost, multi-functionality, miniaturization, and environmental friendliness, electronic packaging has also changed dramatically. Emerging packaging structures, such as 3D packaging, fan-out packaging, and system in packaging, as well as new devices and technologies, such as sensors, radio-frequency (RF) devices, optoelectronics, and flexible devices, pose new and more stringent requirements for materials. An example is molding underfill in fan-out packaging, in which the package encapsulants molding compound and underfill are combined into a single material with ultra-low coefficient of thermal expansion (CTE) and yet infiltrates into the gap between chip and substrate. To continue the trend of ever-shrinking microelectronics, new fabrication methods and processing techniques are also required. With appropriate material selection and design, packaging helps to enhance package reliability, extending the lifetime of electronic devices. In the following sections, we will review the use of encapsulant materials in electronic packaging.

1.1.1 Encapsulation in electronic packaging

A major material used in electronic packaging is encapsulant. Figure 1-2 shows the many polymer-based composite materials that can be found in levels 1 and 2 of electronic packages, and many can be categorized as encapsulants: molding and potting compounds, underfills (flip-chip, CSP/BGA), glob top encapsulant, and silicone encapsulant. The rest of materials are generally used for adhesives, substrate, electrically conductive, or thermally conductive applications such as thermal interface material or die attach adhesive. The commonly used polymer matrices are epoxy and silicone. Epoxy resin offers high adhesion to a number of surfaces, high hardness, low processing viscosity, and low cost, whereas silicone resin has the advantage of low moisture uptake, low modulus, and high

thermal stability. Based on the major polymer systems, the many different functionalities and applications of electronic packaging composites are derived from the filler system. For example, silver is used in electrically conductive adhesives for its low resistivity, and silica is used in molding compounds and underfills for its modulus enhancement and low CTE.

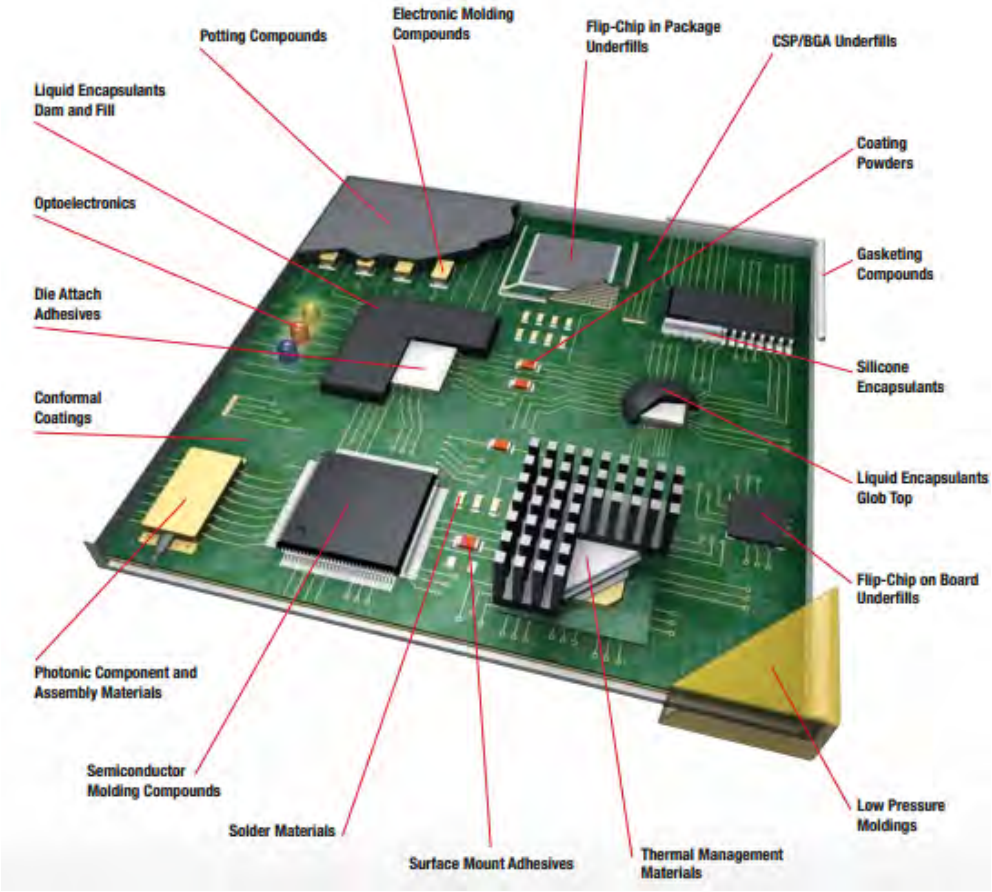

Figure 1-2. Polymer composite materials used in electronic packages [3].

Encapsulant materials are formulated to enhance device reliability. As such, the materials are typically required to meet specific property targets. The most basic requirement for encapsulants is good adhesion to neighboring surfaces. To be used in electronic packages, encapsulants also need high electrical resistivity and low ionic

content. Low moisture absorption is preferred because water can alter the polymer structure, and can be the source of dimensional instability when moisture creates high pressure at elevated temperatures. Additional material property requirements are present for specific encapsulant applications. The present dissertation is focused on encapsulants used for two specific applications: underfill and LED encapsulant. In the following sections, we will review the structures of first-level LED and IC packages, recent developments, and challenges.

1.2 LED packaging

Encapsulants are used in LED packages to provide environmental protection to the LED chip, serving as a barrier against oxygen, humidity-induced corrosion, and mechanical and thermal stresses. An additional and important benefit of encapsulating the chip is to increase light extraction efficiency. In a typical LED package structure (Figure 1-3), the chip is connected to the lead frame via bond wire, and secured to the heat-drawing substrate with die attach adhesive. Without the encapsulant, emitted light directly travels from the chip to air, and is refracted at the interface according to Snell's law:

$$\frac{sin\theta_1}{sin\theta_2} = \frac{n_2}{n_1} \tag{1}$$

Because the chip has much larger refractive index (RI) than air, much of the emitted light is reflected internally. Therefore, encapsulation of the chip using a material with medium RI can reduce internal reflection of light.

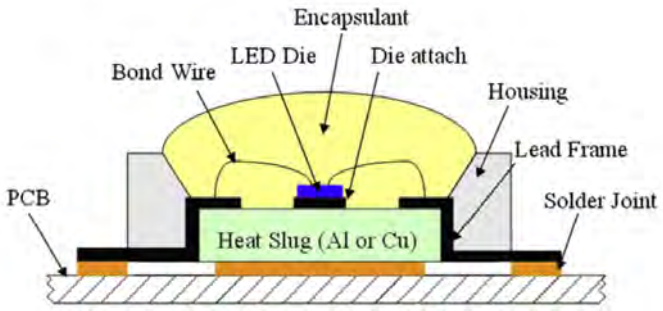

Figure 1-3. Cross-section of typical LED package structure where LED is assembled on PCB [4].

The light extraction efficiency (LEE) of the LED package increases with increasing encapsulant RI, until it approaches ~2.0, at which LEE reaches saturation [5]. RI of the encapsulant can be modified by increasing the RI of the polymer, or by adding high-RI inorganic fillers. Typical polymers have RI in the range of 1.3 – 1.7, and the RI of polymer can be increased by incorporation of high RI atoms or functional groups. The Lorentz-Lorenz equation predicts that substituents with high molar refraction and small molar volume will increase the RI of the polymer [3]:

$$\frac{n^2 - 1}{n^2 + 1} = \frac{R_m}{V_m} \tag{2}$$

where n is refractive index, R_m is molar refraction, and V_m is molar volume. Molar refraction is related to the polarizability and density of the substituent. Generally, more polarizable and higher density substituents give higher molar refraction, because the

electron densities of such substituents are more easily disrupted by the incoming electromagnetic wave, thus slowing down light waves more. Examples of substituents with high molar refraction include halogens (Cl, Br, I), aromatic groups (phenyl, naphthyl), metals, and sulfur-containing moieties (S-H, S-S) [6], [7].

Using typical polymers as the base of encapsulant, RI of the encapsulant can be increased with high-RI fillers. The RI of the composite encapsulant can be estimated by the effective medium approximation, where the composite RI is simply the additive result of the component RI scaled with volume fractions (V_m and V_f for matrix and filler):

$$n_{composite} = V_m n_m + V_f n_f \tag{3}$$

The approximation directly leads to the observation that high RI composite can be obtained with high-RI fillers at high filler loading. The most commonly used fillers materials include amorphous silicon (RI = 4.23), TiO_2 (RI = 2.50-2.90 for different phases), ZrO_2 (RI = 2.10), PbS (RI = 4.20), CeO_2 (RI = 2.18) and ZnS (RI = 2.36) [7]–[11]. The RI of polymer composites have been reported to reach 1.80 with high volume fraction of TiO_2 [11].

In order to enhance LEE and maximize light output, the encapsulant material should also exhibit high transparency, which poses requirement on the size and dispersion of high-RI filler in the composite. Large domains of inorganic fillers will reduce the transparency of the encapsulant due to scattered light beams. Compared to Mie scattering, Rayleigh scattering describes the decrease in light intensity when the particle size is much smaller

than the wavelength of light and is a more appropriate approximation for the transparency loss in nanocomposites:

$$\frac{I}{I_0} = exp\left[\frac{-3V_p x r^3}{4\lambda^4}\left(\frac{n_p}{n_m} - 1\right)\right] \quad (4)$$

Where I_0 is initial light intensity and I is final intensity, V_p is volume fraction of particle, x is path length, r is particle radius, λ is wavelength, and n is refractive index for particle or matrix, as denoted in the subscript. In polymer nanocomposite, the intensity of transmitted light is a function of filler loading, filler size, wavelength, and RI of filler and matrix, and the transparency decays exponentially with volumetric filler loading and with the cube of particle size [12]. Scattering-induced loss of transparency can be minimized for composites where the filler domains are much smaller than the wavelength of light. More specifically, the loss of transparency can be greatly reduced when the filler domain is smaller than one-tenth of the wavelength [7]. Considering visible spectrum as 400 – 800 nm, the filler domain in the encapsulant should be smaller than 40 nm. Furthermore, Cai *et al*. reported the simulated transmittance of composite materials with nanoparticle fillers, and concluded that nearly 100% transmittance can be achieved in composites up to 40 vol.% loading with < 10 nm nano-fillers [13]. However, as filler size increases, transmittance decreases rapidly. With ~ 30 nm fillers, transmittance drops to ~ 85% at 40 vol.% loading (Figure 1-4).

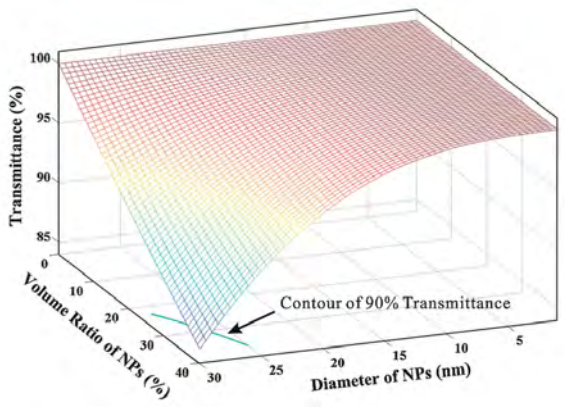

Figure 1-4. Transmittance of polymer composite as a function of filler loading and filler size [13].

To reduce light scattering, the synthesis and dispersion of nanoparticle fillers become important. Sol-gel synthesis of nanoaprticles can achieve good control over particle size and dispersion. Kim *et al.* reported direct grafting of siloxane monomers on Zr nanoparticles in the sol-gel synthesis, and the siloxane-Zr particles undergo crosslinking by hydrosilylation during curing [14]. However, transparency > 80% was limited to composites with < 5 wt.% Zr, limiting the RI of the composite. In sol-gel synthesis of Si-based composite material, RI was reported to achieve 1.56 [15]. Compared to Zr and Si, TiO_2 has higher RI, and sol-gel synthesis of TiO_2 has increased the RI of polymer composite to 1.7 [16]. Methods other than sol-gel synthesis have also shown success in enhancing the composite RI. Synthesis of Si nanoparticles via a reverse micelle method gave vinyl-grafted Si fillers that can crosslink with silicone resin. The composite RI was reported at 1.73 with 15 wt.% of filler [17]. Olefin-based nanocomposite with surface-

modified TiO_2 gave RI above 1.80 [18]. However, in the previous reports, long-term stability of the nanocomposites is rarely discussed.

1.3 Integrated circuit packaging

1.3.1 Flip-chip technology

Flip chip is the first level IC packaging approach in which the active side (with IC) of the silicon chip is faced down and connected to the substrate, printed wiring board (PWB), printed circuit board (PCB), or interposer [19]. The active sides of the chips are bumped with solders (Figure 1-5). During thermal reflow or thermocompression bonding process, the solder melts and wets on the metal contact pad of the substrate to form the electrical and mechanical connections between the IC and the substrate. Compared to wire bonding, where the active side of IC faces upwards and connects to the lead frame via gold, copper, or alloyed aluminum wires, flip chip offers many advantages: 1) higher input/output density and better use of real estate due to full utilization of the chip area for interconnection, 2) shorter lead length, lower inductance, smaller device footprint, and lower profile, and 3) higher throughput and yield due to simultaneous self-aligned interconnect formation of all solders [20], [21].

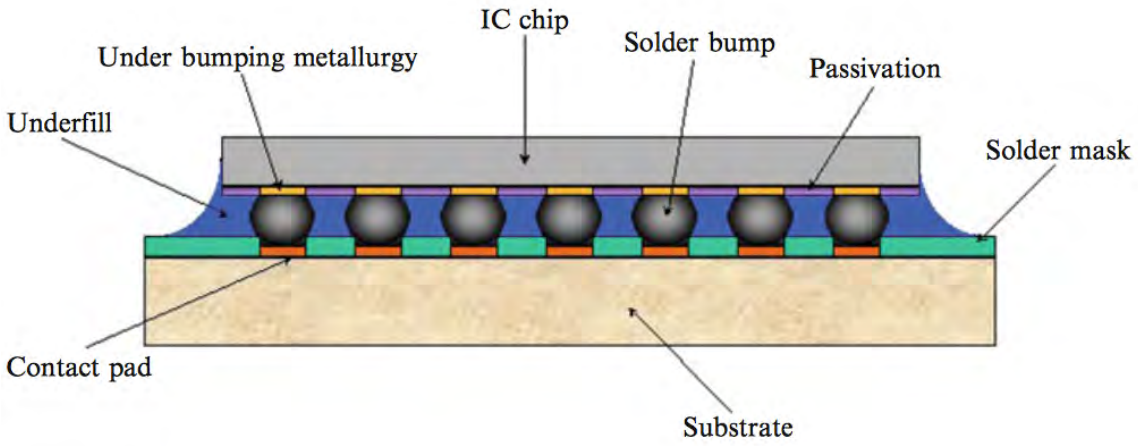

Figure 1-5. General configuration of a flip-chip package with underfill. Reprinted with premission from [22].

The thermomechanical fatigue life of the solder joints is a major concern in flip-chip technology. The thermomechanical stress is mainly derived from the CTE mismatch among Si die (2.5 ppm/K), solder joints (18-22 ppm/K), and substrate (4-10ppm/K for ceramics and 16-24 ppm/K for organic FR4 board) [23]:

$$\sigma = E \cdot \varepsilon = \int_{T}^{T_b} E \cdot \Delta\alpha \cdot dT \tag{5}$$

Where σ is stress, E is modulus, ε is strain, α is CTE, and T is temperature. The bonding temperature T_b is typically defined as the stress-free temperature, and the stress is integrated over temperature. It should be noted that E and α are not necessarily constants over the temperature range. In a bonded flip-chip structure, the shear stress experienced by the solder joints increases with increasing distance from the central neutral point.

Due to the above-mentioned thermomechanical stress concerns, early flip chip packages used high cost ceramic or silicon materials as substrates. It was until Hitachi first demonstrated improved solder fatigue life with resin infiltrated under the chip for stress redistribution that cheaper plastic substrates could be used to replace the ceramic or silicon substrates. The infiltrated resin material is a liquid encapsulant called underfill typically composed of epoxy resin matrix and silica fillers. Underfill can be applied to the package before (pre-applied) or after (post-applied) interconnect formation. After deposition, underfill can be thermally cured to form a cross-linked network and converted to a thermoset polymer. Highly filled underfill exhibits high modulus, low moisture absorption, and low CTE matching that of the solder joint, as well as good adhesion to mechanically couple the chip to substrate to restrain most of the lateral movement between two interfaces. Thermomechanical stresses on the solder joints are redistributed among the chip, underfill, substrate and all the solder joints, instead of concentrating on the peripheral joints. Figure 1-6 shows the effect of underfill on enhancing package reliability. The package is stress-free at solder bonding temperature (210-225˚C for eutectic $Sn_{63}Pb_{37}$, 235-250˚C for $Sn_{96.5}Ag_{3.0}Cu_{0.5}$, 250-270˚C for eutectic $Sn_{96.5}Ag_{3.5}$). As package temperature decreases, the differential thermal shrinkage results in large shear stress on the peripheral solder joints. Without underfill and under cyclic stress, the joints begin to crack and fail. When underfill is infiltrated into the package, the stress is redistributed across all solder joints and each join is able to sustain the stress under cyclic loadings. Cured underfill can reduce the solder strain level to 0.10-0.25 of the strain in joints which are not encapsulated, and increase the fatigue lifetime of the solder by a factor of 5-24, with filled underfills

giving much longer lifetime than the unfilled counterpart [24]–[26]. In addition to dissipating thermomechanical stress, underfill also provides the environmental protections to the solder joints.

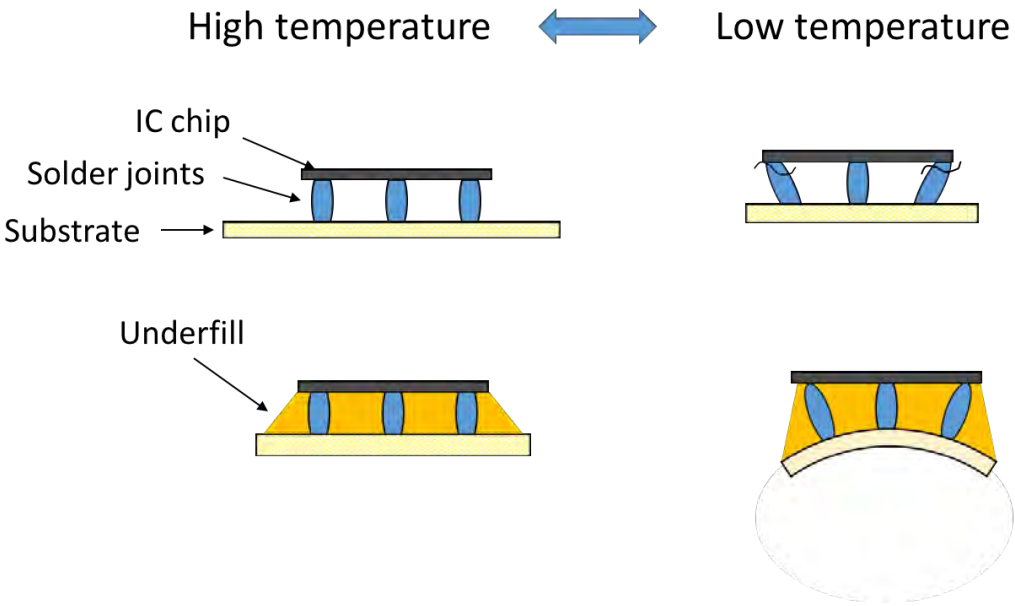

Figure 1-6. Effect of underfill on redistribution of thermomechanical stress.

1.3.1.1 Capillary underfill technology

The conventional, post-applied underfilling method involves infiltrating the underfill into the gap between already-bonded chip and substrate. Because infiltration relies on the capillary action of drawing underfill into the gap, the method is also called capillary underfill technology. Figure 1-7 shows the process of capillary underfilling. First, flux is dispensed onto the metal bond pads to remove the metal oxides from the surface. After chip is landed face-down on the substrate and bonded by high-temperature reflow or

thermocompression process, flux is cleaned from the package. Then underfill is dispensed from a syringe and pulled into the package by capillary force, and finally heated and cured to give the crosslinked composite.

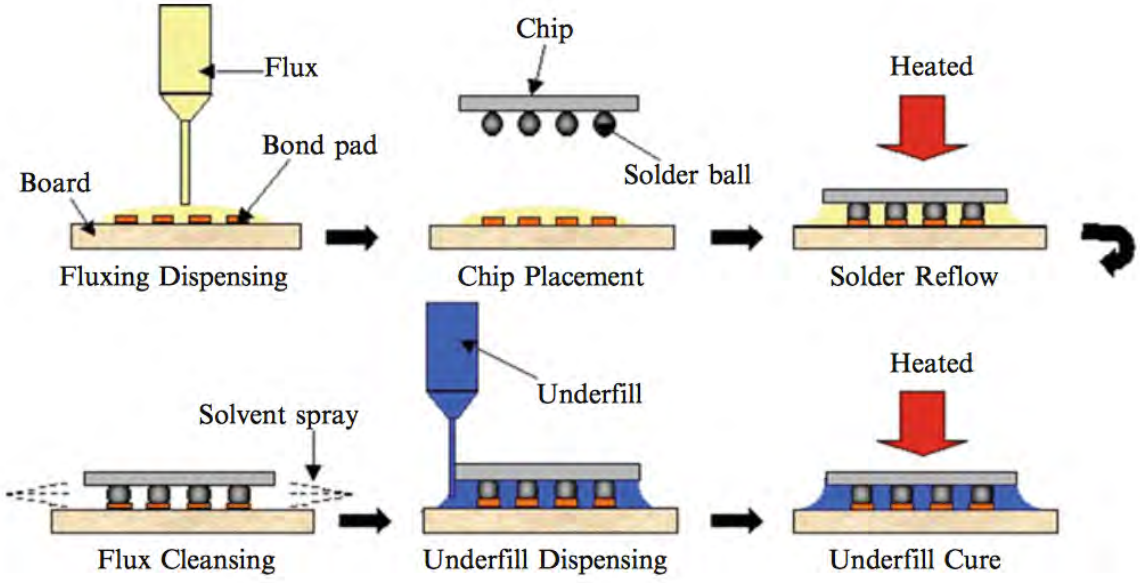

Figure 1-7. Capillary underfill process. Reprinted with permission from [22].

With the current microelectronics trend of reducing size and lowering cost, it is inevitable that chip dimension and I/O counts increase, and the gap height between chip and substrate decreases. Reduced gap height makes flux cleaning more difficult, and flux residues can lead to interfacial issues in the package, such as reduced adhesion, due to the incompatibility between underfill and flux [27], [28]. In addition, the capillary flow is often the limiting step in the capillary underfilling process. The flow is slow, and imperfect flow results in voids in the interconnection layer. Filler settling and non-homogeneity can also result in the silica filler-epoxy matrix system. The chip-on-substrate structure can be

modelled as two parallel plates and the underfill can be modelled as a viscous flow. The Hele-Shaw model can be used to simulate the flow [29]:

$$t_{fill} = \frac{3\eta L^2}{\sigma h \cos\theta} \tag{6}$$

Where t_{fill} is the time required to fill the gap between the parallel plates, η is the viscosity of the underfill, L is the length of the chip, σ is the coefficient of surface tension, h is the gap height, and θ is the underfill contact angle. From equation above, it is clear that longer fill time is required to underfill a package with a larger chip and a smaller gap height. Solder bumps and surface roughness are not considered in the Hele-Shaw model. It has been shown that, because of the low underfill contact angle on solder, the presence of solder bumps increases the capillary force drawing the underfill into the gap. Assuming constant gap height, the capillary force increases with decreasing bump pitch till it reaches a maximum. After which the capillary force drops to zero rapidly as the bump pitch approaches the bump diameter [30].

Reduced gap height also introduces limitation on the filler size. For capillary flow, the filler size should be half of the gap height. When bonded to PWB, the filler size should be limited to one-third of the gap height because plastic-laminate boards have higher surface roughness [31]. Therefore, filler size is required to go into nano-regime as package size decreases. The side effect of reducing filler size include increased filler surface area and increased viscosity, making it more difficult to completely underfill the gap.

To reduce the viscosity at underfill dispense, a common practice is to increase the temperature, either by pre-warming the underfill or heating the substrate. A typical underfill having viscosity of above 4,000 cP at room temperature can reduce its viscosity to 200 – 400 cP when heated to 80˚C [32], [33]. However, the practice of heating the underfill is limited by the curing activity and pot life of the underfill. Underfill dispense and flow cannot continue when gelation occurs.

1.3.1.2 No-flow underfill technology

Due to the many steps involved in the capillary underfilling process and the flow difficulties with fine pitch and small gap packages, a simpler and less time-consuming process was sought after. In 1992, a process later termed "no-flow" underfilling was invented [34]. In this process, flux and underfill are combined. As shown in Figure 1-8, the underfill is dispensed on the substrate with metal bond pads, and then bumped chip is aligned and placed on the substrate. The final step is solder bonding by reflow or thermocompression process. During interconnection formation, fluxing agent is activated, metallurgical bonding is formed between solders and bond pads, and underfill is cured, although additional post-cure may be required in an oven. In this process, flux dispensing and flux cleaning steps are eliminated, and the solder bump reflow and underfill curing steps are combined. It also removes the capillary flow step and eliminates the defects such as voids and flow marks that result due to the shorter gap height and larger chip dimensions.

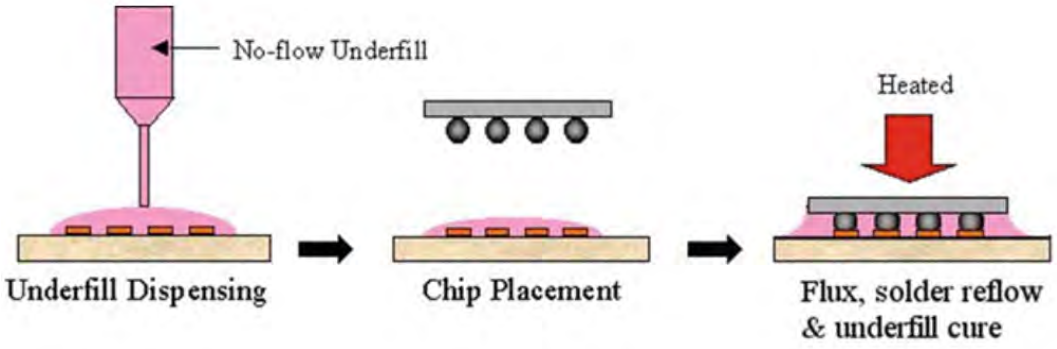

Figure 1-8. No-flow underfill process. Reprinted with permission from [22].

The underfill material is critical for the no-flow process. The key-enabler properties of no-flow underfills include build-in fluxing capability and latent curing ability [35], [36]. In addition to the requirements of capillary underfills such as low CTE, strong adhesion, and appropriate modulus, no-flow underfills should also meet the following requirements:

- Have curing profile that matches the interconnect bonding profile. Curing latency is desired so interconnections are formed before the underfill is cured. When underfill is gelled or cured prematurely, the solder bumps cannot properly collapse onto the bond pads with the desired yield or interconnect reliability.
- Provide sufficient fluxing power to reduce the surface metal oxides on the solders bumps and metal bond pads into metal so that metallurgical bonding can take place.
- Be fully cured during the reflow or thermocompression process, or in an additional post-cure step below 175˚C after package is interconnected.
- Have zero or low filler entrapment in the solder joints. More detailed discussion will be presented in Section 1.3.4.

The first requirement, curing latency, varies by the solder and the bonding process: mass reflow or thermocompression. For lead-containing solders, the peak temperature is lower due to the lower melting point. The difference in peak temperature lead to higher underfill curing latency requirement for lead-free bonding processes. For lead-free solder, a typical mass reflow profile is shown in Figure 1-9, and a typical thermocompression bonding profile is shown in Figure 1-10. Both processes have a soaking step designed to activate the flux, and a peak temperature designed to melt the solder. Higher curing latency is required for lead-free solder interconnects since higher temperature is reached before solder joints are formed.

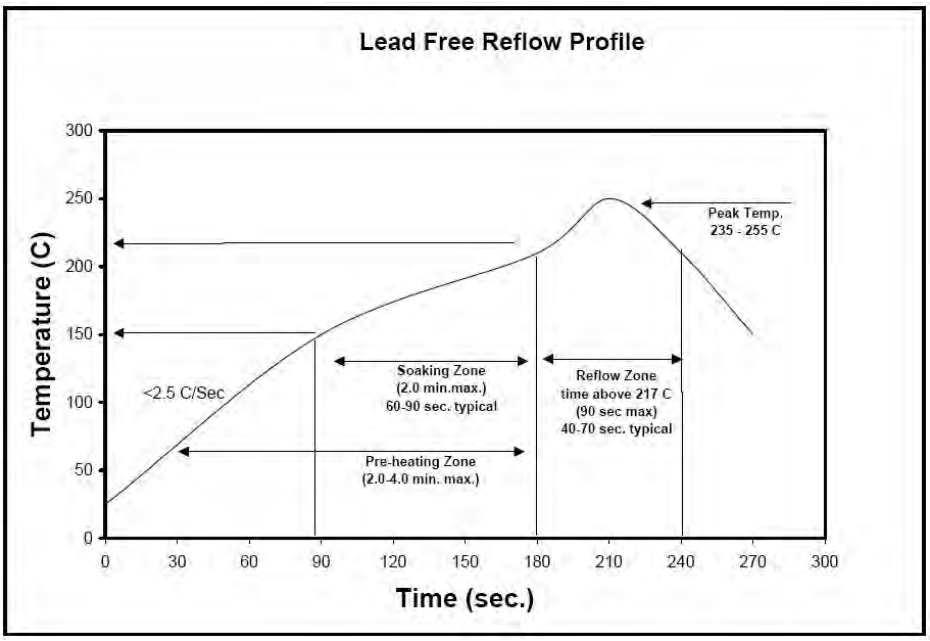

Figure 1-9. Reflow profile for lead-free solder [37].

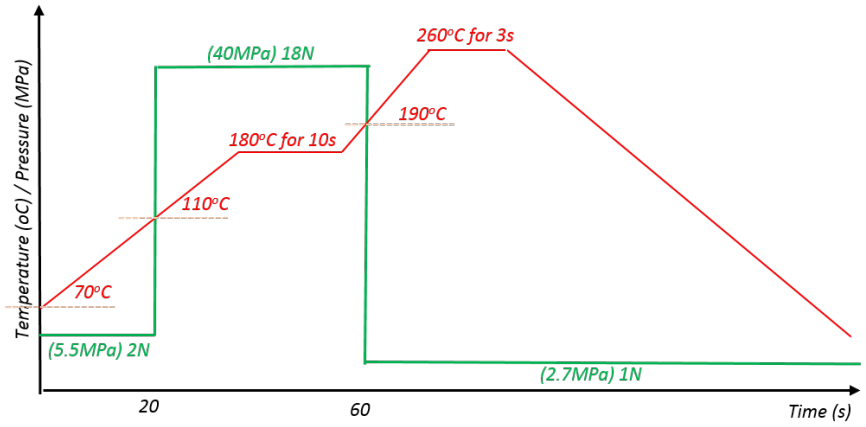

Figure 1-10. Thermocompression bonding profile for lead-free solder.

The major differences between the two bonding processes are process time and pressure. Compared to the mass reflow process, the thermocompression bonding process takes much shorter time and involves an applied pressure. Pressure is applied during the soaking stage to facilitate solder-bond pad contact and to remove volatile species generated by the flux. Small pressure remains during the peak temperature stage to secure and align the chip in place without forcing the molten solder to flow out. The shortened process time in thermocompression bonding means the curing kinetics of underfill should be modified to match the time factor. The ramp rate in thermocompression bonding is ~ 6 K/sec in lab-scale bonders and up to 400 K/sec in industrial production tools [38]. The high ramp rate essentially "delays" underfill gelation to a higher temperature. Therefore, underfills for thermocompression bonding should have less curing latency such that, when combined with the high ramp rate, the underfill cures shortly after interconnections are formed.

The comparison of capillary and no-flow underfilling processes are summarized in Table 1-1. Capillary underfilling technology is able to use highly filled underfill systems through filler system engineering, but flow issues remain challenging. In particular, in fine-pitch and small gap height packages, flow issues aggravate and capillary underfill is not compatible with the package structure. On the other hand, no-flow underfilling combines fluxing, solder bonding and underfill curing into one step, saving time and cost, but it is challenging to eliminate filler entrapment and design the curing kinetics such that the curing and bonding profiles match.

Table 1-1. Comparison of capillary and no-flow underfilling processes.

Property	Capillary underfilling	No-flow underfilling
Dispending time	After solder bonding	Before solder bonding
Apply to	Die attached substrate	Substrate or wafer
Flux process	Required	Not needed
Interconnection process	Mass reflow or thermocompression bonding	Mass reflow or thermocompression bonding
Advantages	Compatible with highly filled underfills (low CTE)	▪ Eliminates capillary flow and separate fluxing steps ▪ Streamlined process with combined fluxing, solder bonding and underfill curing
Challenges	▪ Flow-related: slow flow, voids, filler settling and flow marks ▪ Difficulty in flow in fine-pitch and small gap height packages	▪ Filler entrapment with highly filled underfills ▪ Matching curing and bonding profiles

1.3.2 Underfill materials

Underfill materials are composed of three major components: resin, filler, and additives. Organic resin serves as binder and should meet requirements including high

dimensional stability, good chemical resistance, high mechanical strength, and strong adhesion to surfaces in the package. Thermosetting epoxy resins are most commonly used for this role. The resin system also includes a curing agent that forms crosslinked structure with epoxy resin upon curing, and a curing catalyst that is selected specifically for the underfilling and solder joint formation processes. Resin modifiers can be added to form hybrid polymers with epoxy and to introduce additional functionalities for improved package reliability. Rubberizing polymers with low T_g and low modulus, such as polysiloxane, have been added to reduce the stress in the underfill and to improved underfill toughness [39], [40]. The resin components extensively used in the present thesis are shown in Figure 1-11. The reaction pathways of the curing reactions have been studied extensively [41], [42]. It is generally accepted that the pyridine N on the imidazole catalyst initiates the reaction via nucleophilic attack on the anhydride curing agent [43]–[45]. After the attack, the opened anhydride ring can continue the curing reaction by a second nucleophilic attack on the epoxide ring (Figure 1-12). An alternative reaction route involves the bond formation between epoxy and imidazole, also via nucleophilic attack (Figure 1-13). A 3D crosslinked structure is formed after the curing reaction.

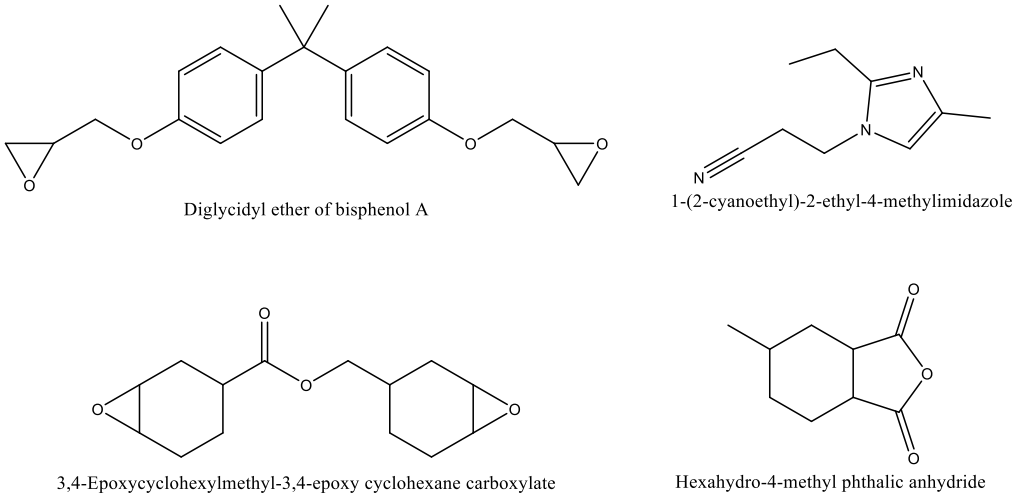

Figure 1-11. Chemical structures of epoxy resin system.

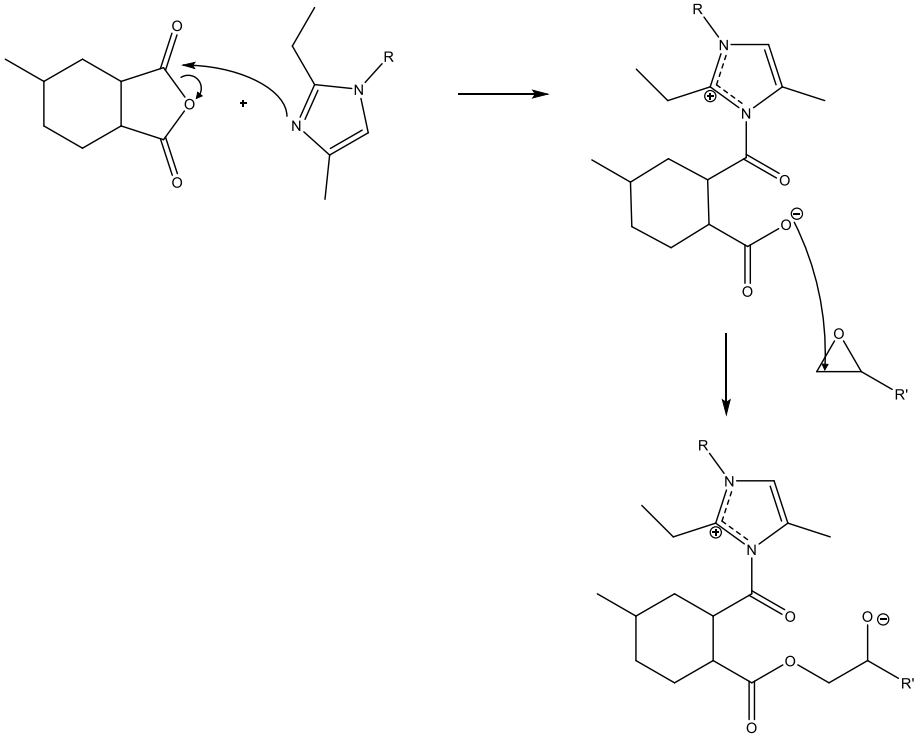

Figure 1-12. Curing reactions in the epoxy resin. R = cyanoethyl, and R represents the rest of epoxy monomer that is not involved in the reaction.

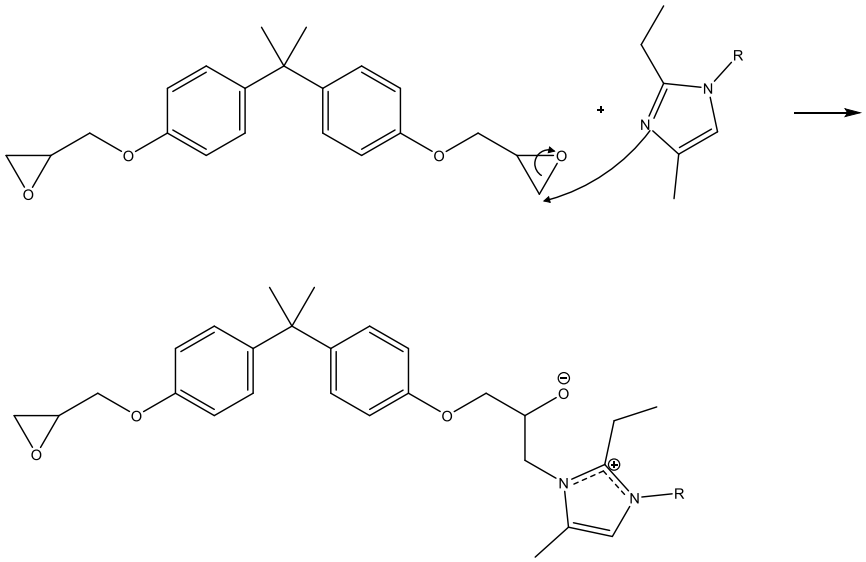

Figure 1-13. Nucleophilic attack reaction of imidazole with epoxy. A bisphenol-A epoxy is shown as a representative epoxy structure. R = cyanoethyl.

Silica fillers are the most commonly used filler material in underfill, for their low-CTE of 0.5 ppm/K can effectively reduce the underfill CTE. Others benefits of incorporating silica fillers include reduced moisture absorption, higher fracture toughness, and higher modulus to match that of the solders, leading to improved mechanical properties in the package [46], [47]. For packages such as high power devices, where thermal management is a concern, highly thermally conductive fillers can be used. Examples of such fillers include aluminium nitride, boron nitride, and diamond [48]–[51]. Because solid fillers impede the flow of polymer resin, the loading, size, shape and surface chemistry of fillers have an important consequence on the viscosity of the underfill. Comparing underfills with the same loading of mono-dispersed fillers, micron-sized silica fillers give lower underfill viscosity, and nano-fillers of the same shape and surface chemistry have

the opposite effect due to difference in surface area. As a result, processing limitation is quickly reached at relatively low content of nano-fillers. However, higher filler loadings (50-70 wt.%) is important in reducing the underfill CTE. Therefore, fillers are typically not mono-sized but over a size distribution. Filler size distribution has been widely studied for enhancing solid packing, reducing percolation threshold, reducing filler settling, and reducing viscosity [52], [53]. In a binary system, the optimal proportion of large particle is about 0.75 when the size ratio of small to large spheres is less than 0.1 [54], [55]. Figure 1-14 shows that, for epoxy composite with 65 vol.% of AlN and silica fillers, the optimal filler size distribution gives the highest packing fraction and the lowest viscosity as represented in longer spiral flow length [56]. Beneficial properties such as higher thermal conductivity, higher flexural strength, and lower moisture absorption are results of high packing fraction. In practical usage, underfills contains multiple filler sizes, which allows even better optimization of composite viscosity and filler packing.

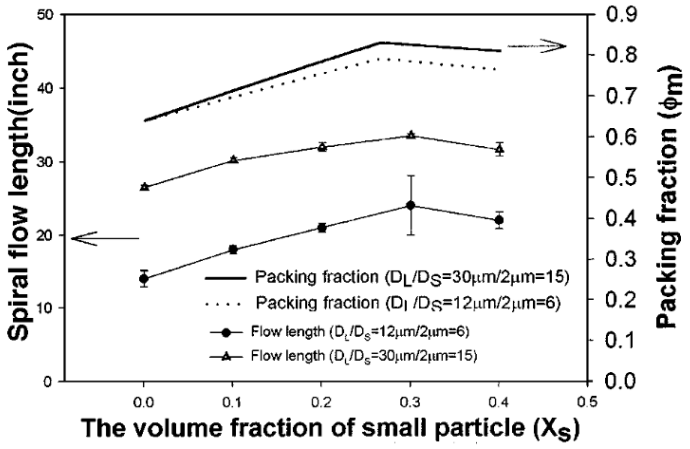

Figure 1-14. Effect of filler size distribution on composite viscosity and packing fraction. Reprinted with permission from [56].

Spherical fillers also give lower underfill viscosity because they have the smallest rotational diameter when compared to elliptical or flake-type fillers. In fact, flake morphology of fillers will give paste instead of flowable composite. The effect of surface chemistry on underfill viscosity will be discussed in more detail in the next section. In general, filler surfaces that have favourable interactions with the resin gives lower viscosity due to less and smaller agglomerates in the system.

Additives are introduced into underfill systems to enhance the properties of cured underfill. Interfacial agents such as silane molecules can bond dissimilar surfaces and are commonly used for the roles of adhesion promoters and filler dispersing agents. An example is γ-glycidoxypropyltrimethoxysilane (Figure 1-15) that can be used to disperse silica fillers. The hydrolyzed methoxy group can bond with silica via a dehydration reaction and the epoxide end group interacts with the resin. Detailed description of the silane-silica reactions will be reviewed in Section 1.3.3.2. In no-flow underfills, fluxing agents such as polyol or organic acids are also added [57]. The fluxing agents work by a redox reaction where the metal oxide on solders and bond pads are reduced to metal, and the fluxing agent is oxidized.

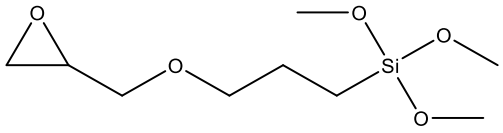

Figure 1-15. Structure of γ-glycidoxypropyltrimethoxysilane.

The ideal underfill properties are presented Table 1-2. Low curing temperature and short curing time are desired to limit high-temperature exposure of other package components. High T_g over 125˚C gives better thermal stability of underfill in the temperature range (-55 ~ 125˚C) of typical thermal cycling and thermal shock reliability tests (JEDEC standards) by avoiding the glass transition region in the polymer and avoiding the rubbery phase in epoxy. The significance of the filler system is shown in the many filler-related properties, such as CTE, modulus, fracture toughness, moisture absorption, etc. Because underfill is used to encapsulate electronic components, dielectric and electrical property requirements are also listed. In order to satisfy the material requirements for high-performance underfills, existing and new challenges in filler dispersion, thermomechanical performances, and flow control of underfills should be investigated.

Table 1-2. Ideal underfill properties [58].

Curing temperature	< 150˚C
Curing time	< 30 min
T_g	> 125˚C
Working life	> 16 hr
Viscosity (RT)	< 25 mPa·s
CTE (α_1)	22 -27 ppm/K
Modulus	5 – 10 GPa
Fracture toughness	> 1.3 MPa·$m^{½}$
Moisture absorption (8 hr in boiling water)	< 0.25 %
Filler loading	50 – 70 wt.%
Alpha particle emission	< 0.005 counts/cm^2/hr
Shore D hardness	> 85
Volume resistivity (RT)	> 10^{13} Ω-cm
Dielectric constant (RT and 1 kHz)	< 4.0
Dielectric loss (RT and 1 kHz)	< 0.005
Ionic content (Cl, Na, K, Fe, etc)	< 20 ppm

1.3.3 Filler-matrix interface

Typical functional polymer composite materials are consisted of filler and polymer matrix. At first glance, one might oversimplify the interface to a two-dimensional area. However, in polymer composite systems, it has been shown that the interphase between filler and bulk polymer matrix has a volume, and exhibit properties that differ from both the filler and the matrix [59]. The adsorption of polymer chains to the filler surface is the reason for interphase formation, and the effect of the interphase on the properties of the composite is a complex function of interfacial interactions, interfacial area, inter-filler distance, and spatial distribution of fillers.

1.3.3.1 Interphase effects

The nature of interfacial interactions play an important role in determining the properties of the interphase— attractive interactions lead to slower polymer chain dynamics in the interphase, while repulsive interactions have the opposite effect. With the large area of interfaces in nanocomposites, substantial deviation of nanocomposite T_g can be observed, and the direction of change is attributed to the nature of the interfacial interactions. In the case of repulsive interfacial interactions, free volume results at the interface, leading to decreased T_g [60]–[62]. On the other hand, attractive interactions lead to partially immobilized polymer chains close to the filler surface, subsequently result in T_g increase [63]–[65]. Rittigstein *et al.* reported that hydrogen bonding between silica and poly(methyl methyacrylate) (PMMA) and poly(2-vinyl pyridine) (P2VP) lead to up to 10 K at 0.4 vol. % loading, while non-attractive silica-polystyrene (PS) lead to T_g decrease

[66]. Furthermore, the T_g of PMMA and P2VP polymer films increase with decreasing distance to silica surface, indicating the confinement effects as the main contributor to increased T_g in nanocomposites, and the effect of confinement can extend to hundreds of nanometers in nanocomposites [67]. Because of the significant interphase thickness relative to the filler radius, the "effective particle volume fraction," which includes both the filler volume and the interphase volume, is larger than the actual particle volume fraction, the interphase can greatly affect bulk material properties of nanocomposites. Nanofiller-incoporated polymer composites with attractive interfacial interactions show reduced CTE and increased modulus, while those with limited filler-matrix interactions and interfacial free volume show reduced elastic modulus and reduced viscosity [62], [68]–[70].

Assuming ideally dispersed filler particles in polymer matrix, filler size will directly influence the interfacial area and inter-filler distance. For composites with the same filler loading, the one with nanosized fillers will have considerably larger filler-matrix interfacial area than that with micro-fillers. As the interphase can be approximated as a layer of a certain thickness extending from the surface of filler, the interphase volume increases linearly with interfacial area. Reports show that the interphase thickness is roughly on the same order for varying particle size and filler loading [71]–[74]. Using molecular dynamics simulations, Brown *et al.* have concluded that the thickness of the interphase layer is ~ 2 nm and is independent of filler size and filler loading for inclusions of 3 ~ 12 nm diameter [75]. At the same time, Zhang *et al.* showed that the interphase thickness for 25-nm silica particles uniformly dispersed in epoxy ranges from 2.79 to 10.55

nm, and Petrovicova *et al.* reported that the interphase thickness of 7-12 nm silica/nylon composite ranges from 3.6 to 22.4 nm [76], [77]. More recent study by Harton *et al.* showed that the interphase thickness of a silica/poly(2-vinylpyridine) system ranges from 1 to 5 nm for particle diameters of 15 nm to infinity, which is essentially a flat silica surface [78]. For composites with the same filler loading, inter-particle distance τ scales linearly with particle diameter according to the following relationship [76]:

$$\tau = d\left[\left(\frac{\pi}{6\phi}\right)^{1/3} - 1\right] \tag{7}$$

where d is particle diameter and ϕ is volumetric filler loading. Assuming that the interphase thickness is roughly on the same order for fillers of different sizes, it is clear that the inter-particle distance determines the volume ratio of the interphase to the composite. As particle size decreases, the relative interphase volume increases due to increased interfacial area and reduced inter-particle distance, and the effect of interphase becomes increasingly pronounced. For example, compared to micro-sized fillers, nano-silica, silver, aluminum, or carbon black reduced the T_g of epoxy composites due to the extra free volume at the filler-epoxy interfaces [79].

The underlying assumption to the above approximation is ideal dispersion of fillers. Due to high surface energy of nanoparticles and unfavorable filler-polymer interactions relative to filler-filler interactions, fillers agglomerate to reduce the interfacial area exposed to the polymer matrix for energy minimization [80]. As the result of particle agglomeration, the interphase volumes enclosing neighboring particles are merged and the total interphase

volume is reduced. In addition, in composite systems where the filler loading reaches the percolation threshold, increasing the degree of clustering lead to loss of percolated interphase network. In nanocomposites where attractive filler-matrix interaction is expected to increase composite T_g, filler clustering results in reduced T_g increase due to the reduced interphase volume [81]. Compared to the case of well-dispersed filler in matrix, additional effects of filler clustering include reduced modulus, reduced degradation temperature, and increased viscosity [82]–[85].

1.3.3.2 Chemical modifications on filler surfaces

Chemical modifications on filler surfaces are often performed to decrease surface free energy, ensure favorable filler-matrix interactions and improve filler dispersion in the polymer matrix, thus enhancing composite properties. The choice of method and modification agents is highly dependent on the surface chemical environment of the filler material. For example, metal oxide fillers with surface hydroxyl groups such as titanium dioxide, zirconium dioxide and silicon dioxide, can be modified with silanes, phosphonic acids, and carboxylates, while metal fillers such as silicon, can be modified with thiols, disulfides, amines, and carboxylic acids [86]–[90]. Because silica is the most widely used filler in electronic encapsulants, the following discussion will focus on the surface modification of silica for incorporation in polymer matrices. Reactive hydroxyl groups on the surface of silica can be used as the reaction sites to form densely packed monolayers in surface modifications, and the number of hydroxyl groups per unit area on SiO_2 is 4.6-4.9 OH/nm^2 according to the Kiselev-Zhuravlev constant [91], [92]. Surface modification on silica is commonly achieved using organosilanes, and the high reaction rates of silanes

towards Si-OH surface groups make them a popular class of surface modification agent for applications in different areas [93], [94]. Functionalization of silica surfaces can be obtained with the functional terminal group on at the end of the alkyl chain, and a second reaction on the end group of a silane layer can be used to modify the functionalization for different applications. In the latter case, the secondary functionalization reaction allows attachment of functional groups that would not be easily attached to surface [95], [96]. Some examples of applications of silane functionalization include aminopropyltrimethoxysilane and aminopropyltriethoxysilane as adhesion promoter, the latter of which has also shown applications in protein binding [97], [98]. Surface hydrophobicity can be achieved with a monolayer coating of fluorinated silane, and the surface can be used towards inactivation of viruses [99].

The structure of organosilanes can be represented as $R_aSi(OX)_b$, where R is an alkyl group, OX is a leaving group, and a and b denote the number of different groups, and can be further classified as monofunctional (a = 1, b = 3), bifunctional (a = b = 2), or trifunctional (a = 3, b = 1) (silane structure scheme). In monofunctional silanes, each silane molecule forms one covalent bond with the silica surface, but the two methyl groups on the Si atom sterically hinders the bonding of neighboring silanes, resulting in lower functionalization density. Trifunctional silanes can react with the silica surface with the three hydrolysable groups, achieving higher grafting density and crosslinking in the monolayer. However, oligomerization of silane molecules can create disordered surface structures and increased surface roughness. Reactive organofunctionality can be incorporated into silane via reactive R groups such as amino, vinyl, and mercapto groups.

The reactive terminal offers the advantage of covalent bond formation with the polymer matrix in composites, whereas non-reactive alkyl R groups can only provide physical compatibility with non-polar matrices.

The reaction of silane on silica surface proceeds in three steps [100] (Figure 1-16). Firstly, silane undergoes hydrolysis with water to produce Si-O-H groups and alkoxy (H-OX) leaving group. In addition to the nature of the R group, the reactivity and strength of the leaving group influence the reactivity of silane and the appropriate reaction conditions for the surface modification. For example, the methoxy groups of methoxysilane can be hydrolyzed faster than the ethoxy groups of ethoxysilane, and aminopropyltrimethoxysilane can react on surfaces at a lower temperature than aminopropyltriethoxysilane [101], [102]. After hydrolysis, the hydrolyzed group form hydrogen bonding with the hydroxyl group on the silica surface. Last step is condensation reaction between Si-OH of silane and of silica to form Si-O-Si covalent bonds, anchoring silane on the silica surface. In the case of bi- or tri-functional silanes, condensation also occurs between neighboring silane molecules, and a crosslinked layer of silane can be obtained.

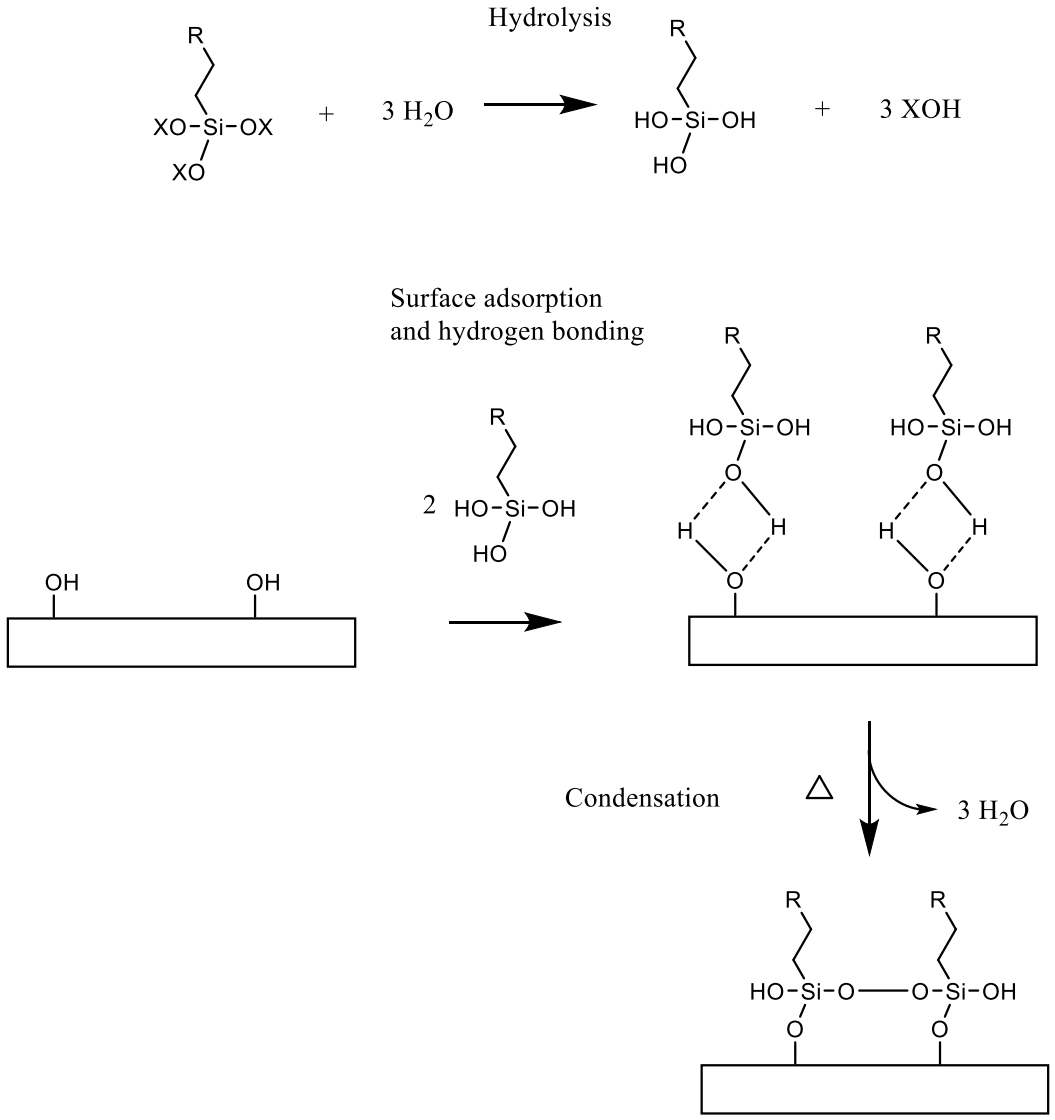

Figure 1-16. Hydrolysis, surface adsorption and hydrogen bonding, and condensation reactions of silane in the surface modification reactions. A trifunctional silane with leaving group X and alkyl group R is shown here.

For the majority of silanes, hydrolysis activation proceeds at a more acceptable rate under either acid or base catalysis. In acid-catalyzed hydrolysis, the leaving group is protonated, and a subsequent S_N2 substitution reaction with a water molecule attacking the

Si atom yields hydroxyl groups bonded to Si. In base catalyzed hydrolysis, hydroxyl ion attacks the Si atom, forming a pentacoordinate intermediate, which proceeds with the hydroxyl displacing the alkoxy group. In acidic conditions, the rate of hydrolysis is increased and the rate of condensation is reduced, thus limiting the formation of siloxane networks that have limited number of silanol groups exposed to the filler surface. In fact, acidic condition stabilizes the hydrolyzed silanes, and the formation of three-dimensional siloxane structures required one month [103]. Temperature effects on the quality of the silane layer have been reported. Pasternack *et al.* showed that *in-situ* annealing at 70˚C produced both denser and thinner silane layer compared to that without annealing due to the thermal-activated organization of silane molecules. The highly packed silane layer is also more resistant against degradation by hydrolysis [104]. Soliveri *et al.* identified the optimal deposition condition of triethoxy(octyl)silane and 1*H*,1*H*,2*H*,2*H*-perfluoroctyltriethoxysilane on silica surfaces to be 90 – 100˚C [105]. Higher deposition temperatures led to more lateral polymerization and vertical polymerization.

Silane deposition can be obtained via vapor phase or solution phase deposition. Haller first reported the vapor phase deposition of 3-aminopropyltriethoxysilane on the surface of Si and GaAs in 1978 [106]. The vapor phase process has advantages in good reproducibility of silane monolayers and reduced formation of siloxane oligomers [107]–[109]. However, the vapor phase silanization process is challenging for filler treatments due to difficulties in achieving uniform exposure of filler surfaces to the silane vapor and in particle collection. Therefore, solution phase deposition is often used for monolayer silane coating on particles. Typically, filler particles are dispersed and reacted with silane

in solution phase, unreacted silane molecules are washed away after the reaction, and treated fillers are collected in the final step [110], [111]. The fillers can be subsequently mixed with polymer to prepare polymer composites [112].

In epoxy matrix composites, fillers are typically coupled to the matrix via amino-functional or glycidoxy-functional silanes [100]. Silane coupling of filler and matrix can enhance thermostabilization, filler dispersion, flowability, moisture resistance and mechanical and dielectric properties. Sun *et al.* reported that, compared to non-treated fillers, silane treatment of nanosilica prior to mixing with epoxy resin reduced moisture uptake and improved filler dispersion, the latter of which contributed to reduced viscosity [110]. Chang *et al.* showed that epoxy composite with aminosilane-treated silica fillers exhibit higher thermal degradation temperature, and reduced moisture absorption and gas permeability [113]. More recently, Guo *et al.* showed that adding silica treated with aminosilane or glycidoxysilane to epoxy matrix improved silica-epoxy interactions and reduced composite viscosity. However, reactive silane affected the stoichiometry of resin components, leading to reduced T_g [114]. Epoxy composite with glycidoxysilane-treated silica fillers show higher volume resistivity, lower dielectric loss, and higher breakdown voltage, and the improved dielectric properties can be attributed to improved dispersion and better filler-matrix interfacial adhesion [115]. When untreated silica particles are added into polymer matrix, tensile strength of the composite was increased, but tensile elongation and impact energy decreased. When silane-treated silica particle are used, similar tensile strength is obtained but tensile elongation and impact energy are increased, suggesting improved composite toughness by the silane layer [116].

1.3.4 Filler entrapment in no-flow underfill technology

As microelectronics evolved over the years, new packaging challenges arise, one of which is trapped fillers in pre-applied underfilling scheme. Device miniaturization drives packages towards fine pitch, low profile, and stacked dies (3D IC). With such package design, traditional post-applied capillary underfilling technology is insufficient and pre-applied no-flow underfilling methods should be used.

However, highly filled no-flow underfills often see fillers trapped between solder joints and bonding pads, compromising interconnection formation, signal transmission, and package reliability. Therefore, current technologies are limited to using underfills with low filler contents. Underfills, as composite materials, derive many of their properties from the silica fillers, and the reduced filler loading level affects the material behavior in multiple ways. As shown in Table 1-3, no-flow underfills exhibit higher CTE and lower modulus, both of which are related to the volume fraction of silica fillers and can be directly attributed to lower filler content. Lower fracture toughness can be attributed to fewer crack deflection sites, and higher moisture absorption because epoxy matrix absorbs water.

Table 1-3. Property comparison of typical capillary underfill and no-flow underfills

	Capillary underfill	**No-flow underfill**
CTE (ppm/K)	22 – 27	60 – 80
Modulus (GPa)	8 – 10	2 – 3
Fracture toughness (MPa-m$^{1/2}$)	> 1.3	Typically lower
Moisture absorption	< 0.25%	Typically higher
Filler content	< 70 wt.%	< 30 wt.%

Few approaches to reducing filler entrapment and thus allowing the use of highly-loaded underfills in no-flow packages have been reported. Zhang *et al.* reported a double-layer underfilling process, in which a high-viscosity and filler-free layer of epoxy resin is dispensed on the bottom and a layer of filled underfill is dispensed on the top [117]. The bottom layer helped to prevent filler entrapment due to the viscosity difference. However, the homogeneity of the underfill was not addressed, and filler separation within the interconnection layer is likely. Another process involving slicing through the underfill-covered solder posts has been reported to eliminate filler entrapment [118]. In this process, the initial filler placement had little impact since the top layer is removed. However, this process may not be ideal for low profile packages due to difficulty in handling thin wafers for slicing. More recently, Kester developed underfill with curing profile closely matching the reflow profile to reduce filler entrapment [119], but the method requires customization for each underfill, bonding profile, and dispense condition.

We propose a more general approach to reduce filler entrapment at interconnects commonly observed in no-flow underfills by surface-patterned hydrophobic – hydrophilic domains that help to control the flow of underfill on the substrate.

Controlling fluids by hydrophobic – hydrophilic patterns on surfaces is not new. As summarized in Table 1-4, such surface patterns have been used for patterning of cell microarrays, microfluidic channels, precision solution arrangement and generation, and even fog collection. However, in the reported applications of surface patterning, the test liquids are typically water, buffered saline solutions of biological fluids, or other low-viscosity solvents and fluids. In the literature, the highest viscosity reported for surface patterning is 0.02 Pa-s, which is lower than the minimum viscosity of underfills by two orders of magnitude. In order to develop surface patterning for controlling the flow of underfill and reducing filler entrapment, a thorough understanding of underfill material and processes is necessary.

Table 1-4. Recent reports on liquid manipulation using hydrophilic – hydrophobic surface patterns.

Preparation of hydrophilic surface	**Preparation of hydrophobic surface**	**Test liquid**	**Application**	**Reference**
Porous copolymer of hydroxyethyl methacrylate [120]	Photografted pentafluoropropyl methacrylate [121]	Mouse and rat cells in medium (viscosity ~0.0011 Pa·s)	Patterned cell microarrays	[122]
Sodium hydroxide and potassium persulfate solution treatment on copper [123]	Copper immersion in n-tetradecanoic acid solution [124]	Water vapor	Fog collection	[125]
Silver metal [126]	Teflon-like polymer [127]	Water (viscosity 0.0009 Pa·s)	Solution arrangement in 2D array	[128]
SiO_x by pulsed plasma chemical vapor deposition [129]	Perfluoropolymer on silicon substrate [130]	Water (viscosity 0.0009 Pa·s)	Precise water droplet generation	[131]
Vacuum ultraviolet (VUV) irradiation [132], [133]	Vapor-phase treatment of octadecyltrimethoxysilane on Si [132], and PECVD deposition of SiO_2 [134]	10% fetal bovine serum and 90% phosphate-buffered salines (viscosity ~ 0.001 Pa·s)	Micropatterend cell culture	[135]
Photografting of hydrophilic methacrylate [121], [136]	Nanoporous copolymer of butyl methacrylate [121]	Water (viscosity 0.0009 Pa·s)	Microfluidic channels	[137]

Table 1-4 continued.

Masked glass slide, followed by plasma treatment [138]	Commercially available WX2100 spray (Cytonix Corp.)	Various solutions of PEG 4000 in Dulbecco's phosphate buffered saline (highest viscosity 0.02 Pa·s)	Gradient generation in microarray	[139]

1.4 Research objectives

The research objective of this thesis is focused on the understanding and application of nanocomposite materials in order to improve their performance in electronic packages, including:

1) Rational design of polymeric composite materials, including filler, matrix, and interphase, for applications in optical and thermomechanical solutions in electronic packaging;

2) Study how the properties of the filler – matrix interface manifest in bulk composite properties, and methods to improve the interface; and

3) Develop materials and interconnection processes for defect reduction in advanced underfilling technology.

CHAPTER 2. HIGH REFRACTIVE INDEX NANOCOMPOSITE WITH HIGH TRANSPARENCY FOR HIGH BRIGHTNESS LED PACKAGING

2.1 Introduction

Light-emitting diode (LED) is a solid-state lighting device that has many advantages over conventional incandescent and fluorescent light sources and has great potential in future lighting. The attractive features of LED include small volume, high efficiency, low power consumption, long lifetime, and environmentally friendliness [140]–[142]. The major components of LED device include substrate, heat sink, die attach, LED chip, bond wire, and encapsulant (in the order of backside to the light-emitting side) [143]. The encapsulant provides environmental protection to the LED chip, serving as a barrier against oxygen, humidity-induced corrosion, and mechanical and thermal stresses. Another important function of the encapsulant is enhancing light extraction. Due to the large refractive index (RI) mismatch between LED chips (RI= 2.47 for GaN at the emission wavelength of 460 nm) and air (RI = 1), about 74% of the emitted light is internally reflected back into the chip [144]. The reflected light not only result in low light extraction efficiency (LEE), but also converts to heat, and the increased device temperature changes light color and further reduces the luminous efficiency [145], [146]. Therefore, an encapsulant is needed to reduce the RI contrast at the interface and to increase LEE.

Epoxy resins can be used as LED encapsulants for their good adhesion to other surfaces in the package, but their chemical structures often render them brittle. Furthermore, epoxy resins degrade when exposed to radiation and high temperatures which results in discoloration, and are unideal for LED packaging [147]. Silicone resins are also widely studied as encapsulant matrices, and they offer higher thermal stability than epoxies. LEE can be improved significantly by increasing the RI of the encapsulant. When a single layer of encapsulant with uniform RI is coated on GaN LED, LEE increases with increasing RI until it reaches saturation with RI approaching 2.0 [5]. The ratio of LEE of encapsulated and non-encapsulated LED chips can be calculated using the equation:

$$\frac{n_{encapsulant}}{n_{air}} = \frac{1 - cos\,\theta_{c,encapsulant}}{1 - cos\,\theta_{c,air}} \tag{8}$$

Where n is the refractive index of the medium, and θ_c is the critical angle at which light is internally reflected back to the LED chip. The LEE ratio for GaN LED as a function of encapsulant RI is shown in Figure 2-1. It is clear that LEE ratio increases with increasing RI of encapsulant. However, the RI of both epoxy and silicone resins lie in the range of 1.40 to 1.55 in the visible wavelength, and are still too low to produce high-efficiency and high-brightness LEDs [148]. Recent reports suggest that modifications on the polymer structure lead to mediocre RI enhancements. Cycloaliphatic epoxy oligosiloxane with high phenyl content show a RI of 1.583 at 633 nm [149]. Hydrosilylation of phenyl-vinyl-oligosiloxane with phenyltris(dimethylsiloxy)silane produced a siloxane with RI of 1.56 at 633 nm [150].By incorporating phenoxyphenyl and phenylthiophenyl groups in polysiloxane, RI of 1.60 and 1.62 at 633 nm were achieved for the two systems,

respectively [151]. However, the RI of the neat polymers are still insufficient to yield high brightness in LED.

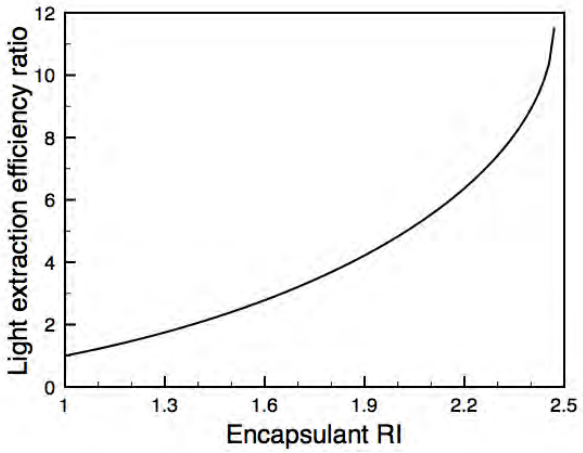

Figure 2-1. Ratio of light extractions from GaN LED chip (RI = 2.47) with encapsulant of RI varying from 1 to 2.5 compared to without encapsulant where the light is directly emitted to air.

Inorganic fillers with high refractive indices are commonly incorporated into the polymer to increase the RI of the encapsulant. The size and dispersion of inorganic fillers should be carefully controlled in order to fabricate encapsulant with uniform refractive index and high transmittance. Loss of transparency in encapsulant can be attributed to light scattering by large inorganic domains and RI mismatch between the filler and the polymer matrix, as described by Rayleigh scattering [12]. Since transparency improvement by RI matching between filler and polymer is not practical for preparation of high-RI composites, it is important that the inorganic filler domains are small. It has been reported that light scattering can be greatly reduced when the inorganic domain size is less than one-tenth of

the wavelength of the incoming light (400 – 800 nm for visible light) [7]. Recently, a sol-gel method was used to fabricate Zr-containing siloxane hybrid material with RI of 1.58. Although the hybrid material showed higher transparency than commercial silicone-based LED encapsulant, the RI was still insufficient [152]. Titanium dioxide (TiO_2) has been studied as a promising filler material for high RI applications. Epoxy with 30 wt.% of TiO_2 nanoparticles prepared by sol-gel method have been reported to achieve RI of 1.7 at 633 nm. For RI of 1.8, it is estimates that 60 wt. % of inorganic filler is required [16]. High RI (RI = 1.81) TiO_2/epoxy composite can be prepared by modifying the nanoparticle surface with carboxylic acid and alkyl amines, but mechanical properties at such high filler loadings were not reported [153]. Takahashi *et al.* reported high RI (1.83 at 633 nm) and high transparency TiO_2/cycloolefin polymer nanocomposites via oleyl phosphate surface modification reactions [18]. However, the polymer is limited in its heat distortion temperature of 120˚C and is not suitable for LED encapsulation application.

Here we report two synthesis methods of TiO_2 nanoparticles and the optical performance of encapsulants prepared using the said TiO_2 nanoparticles. The first method involves two steps, including hydrothermal synthesis of TiO_2 from precursor chemical, and subsequent surface modification of the synthesized particles by silane grafting. It was observed that the synthesis condition gives high-RI rutile phase of TiO_2, but the nanoparticle size and dispersion in the silicone matrix were not ideal, leading to low optical transparency, albeit high RI, at high filler loadings. Therefore, the second method of one-pot reaction involving the *in-situ* surface silanization of TiO_2 nanoparticles during synthesis was adapted. In this method, because the surfactant is grafted onto the

nanoparticle surface as the particles form, improved nanoparticle size control and dispersion in matrix are observed, and highly optically transparent nanocomposite with high RI was successfully prepared.

2.2 Methods

2.2.1 Materials

Titanium (IV) isopropoxide (97%) and ethanol were obtained from Sigma Aldrich, hydrochloric acid (36.5-38%), toluene, formic acid (88%) and isopropyl alcohol (IPA) were obtained from BDH, 7-octenyltrimethoxysilane (95%) was obtained from Gelest. Triethylamine was obtained from Alfa Aesar. Deionized (DI) water was produced from a Barnstead Smart 2 Pure Water Purification system (Thermo Scientific). The two-parts Dow Corning OE6630A-B was used as the polymer matric for the encapsulant. The mixing ratio was 4 parts base to 1 part catalyst by weight or volume. All chemicals were used as received.

2.2.2 Two-step, hydrothermal TiO_2 preparation

TiO_2 nanoparticles were synthesized by a hydrothermal method. The hydrolysis of titanium (IV) isopropoxide in 6 M hydrochloric acid (10 mL deionized water and 10 mL concentrated hydrochloric acid) was performed by adding 3 mL of titanium (IV) isopropoxide into the acidic solution at a rate of 0.6 mL/min using a syringe pump under ambient conditions. After 8-12 hours of stirring and sonication, the reaction mixture was sealed in an autoclave and heated to 120˚C at 10˚C/min and held for 6 hours. After the

autoclave was cooled, the precipitated TiO_2 was cleaned and dispersed using water and ethanol.

The synthesized TiO_2 nanoparticles were surface-modified with 7-octenyltrimethoxysilane. The nanoparticles were collected by centrifugation and re-dispersed in a 95-5 wt. % ethanol-water mixture, which was adjusted to pH 4~5 by formic acid. The concentration of nanoparticle in the dispersion was 10% by mass. The amount of silane added was equivalent to 1 wt. % of the reaction mixture, and was refluxed at 100ºC for 24 hours and cleaned with ethanol. Finally, the cleaned nanoparticles were dispersed in toluene by sonication prior the mixing with the silicone resin.

It was observed that the nanoparticle cleaning process can cause curing issues in the silicone-based composites. It was concluded experimentally that the as-synthesized TiO_2 particles should be cleaned thoroughly to remove residual acids from the synthesis. Cleaning should be performed for as many times as necessary until neutral suspensions of TiO_2 in water were obtained.

2.2.3 One-step, in-situ surface modified TiO_2 preparation

In order to obtain better dispersion of TiO_2 nanoparticles, we modified the synthesis procedure reported by Monson *et al.* [154]. Two reagent vessels were prepared: (a) a mixture of isopropanol (IPA) and deionized water at a volume ratio of 400:1, and (b) a mixture of IPA, titanium (IV) isopropoxide, 7-octenyltrimethoxysilane, and triethylamine at a volume ratio of 100:1:3.38:1.69, respectively. Reagent mixture (a) was dropwise added to reagent mixture (b) under vigorous stirring, and the reaction mixture was kept at room

temperature overnight. The reaction mixture was then heated to 80ºC for 2 days. The TiO_2 nanoparticles were collected by centrifugation and re-dispersed in toluene.

2.2.4 Encapsulant preparation

The TiO_2-toluene suspension was added to the base part of the silicone resin (part B) and mixed. Homogeneous mixture was obtained after 3 hours of sonication. Toluene was removed from the composite mixture by vacuum evaporation at 60˚C. The curing agent (part A) was subsequently added to the mixture and mixed until homogeneous. The curing schedule was 150˚C for one hour. The solvent evaporation process should be performed at temperatures lower than 70ºC. Although raising the temperature would accelerate the solvent removal process, prolonged high-temperature solvent removal process would lead to color changes in the composite.

The encapsulant was coated on a Si substrate for RI characterization, and coated on glass slide for transparency characterization. The Si and glass substrates were cleaned with solvent rinse (ethanol) and UV-ozone treatment prior to coating. A spin coater was used to obtain encapsulant films of uniform thickness. The two-step spinner procedure included 1 min at 500 rpm and 1 min at 6000 rpm.

2.2.5 Characterizations

The dimension of the nanoparticles was determined using transmission electron microscopy (TEM) images, which were acquired using a JEOL 100CX TEM. Dispersion of nanoparticles in the nanocomposite encapsulant was prepared by observing slices of

cured samples of 150 – 170 nm thickness using a diamond blade on a microtome. X-ray diffraction (XRD) analysis was performed using Cu Kα radiation (45 kV and 40 mA) on a Philips X-pert alpha-diffactometer. Optical transparency of coated samples in the wavelength range of 300-800 nm was measured by a Shimadzu Co. UV-2450 UV-vis spectrophotometer. Relative transparency was calculated by dividing the transmittance of the nanocomposite by the transmittance of the neat silicone control sample at the same wavelength. Differential scanning calorimeter (DSC, Q5000, TA Instruments) was used to study the curing reaction of nanocomposites.

The optical properties of composite samples containing hydrothermal TiO_2 nanoparticles were characterized by ellipsometry from 400 to 1,000 nm using a Woollam M2000 ellipsometer. Three incident and reflection angles were used: 65˚ to 75˚ at 5˚ increments. In ellipsometry, a beam of polarized light is directed at the sample, and the reflected light is detected. The change in polarization is characterized by the amplitude ratio Ψ and the phase difference Δ, which are used in subsequent model fitting. A three-layer model is used for the analyses of the composite coatings: silicon, SiO2, and Cauchy film (from substrate to coating). The refractive index of the Cauchy film is related to the wavelength and optical coefficients by the following equation:

$$n(\lambda) = A + \frac{B}{\lambda^2} + \frac{C}{\lambda^4} \tag{9}$$

where *A, B,* and *C* are optical coefficients, and λ is the wavelength. Multiple measurements were taken for each composite coating sample, and the fitting results from the datasets were compared against each other for acceptable differences.

Reliability test of the TiO_2 nanocomposites under thermal cycling test conditions and under 90 % relative humidity was carried out according to the JEITA ED-4701/200 203 standards. The cycles consisted of temperature soaking from 25ºC to 65ºC, to -10ºC, and back to 25ºC, totaling 24 hours per cycle (Figure 2-2). Up to 500 hours of reliability test was performed on the encapsulant material. The optical transparency and RI of the encapsulant were measured before and after the reliability test using the same characterization conditions.

Figure 1 COMPOSITION OF ONE CYCLE

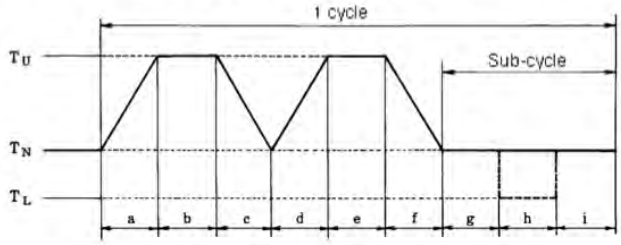

T_U, T_N, and T_L indicate the various temperatures.

Table 1 TEMPERATURE AND HUMIDITY CYCLE CONDITIONS

Conditions / Step	Time (h)	Temperature (°C)	Relative humidity (%)
a	2.5	-	90 ~ 96
b	3.0	65±2	90 ~ 96
c	2.5	-	80 ~ 96
d	2.5	-	90 ~ 96
e	3.0	65±2	90 ~ 96
f	2.5	-	80 ~ 96
g	1 ~ 4	25±2	90 ~ 96
h	3.0	-10^{+3}_{-3}	Arbitrary
i	1 ~ 4	25±2	90 ~ 96
1 cycle	24	-	-

Figure 2-2. Reliability test cycle conditions.

2.3 Results and discussion

2.3.1 Neat silicone resin

The silicone resin used in this study is a commercial, high-RI resin. Table 2-1 lists some of the material properties of the silicone resin. The silicone is designed to meet the challenging needs of the LED market, including high purity, high moisture resistance, high thermal stability, and most importantly, high optical transparency. It also meets processing requirements, such as medium viscosity that is suitable for dispensing and molding processes. Silicone also can act as a stress-absorber in the package to reduce the thermal cycling stress, thus protect the LED chip and wiring components.

Table 2-1. Properties of silicone resin (OE-6630)

Viscosity (mixed)	2,200 mPa-sec
Heat cure time at 150˚C	60 min
Non-volatile content	99.8%
Unprimed adhesion (die shear on Al)	6.7 MPa
CTE	210 ppm/K
Refractive index	1.53
Transparency (450 nm)	99.1 %
Impurity (Na+)	0.1 ppm
Impurity (K+)	0.2 ppm

Table 2-1 continued.

Impurity (Cl-)	0.5 ppm
Volume resistivity	1E16 Ω-cm

The optical properties of the neat silicone resin were characterized before incorporating any nanoparticle fillers. Figure 2-3 shows the refractive index and transmittance of the neat silicone, respectively. At the blue LED emitting wavelength of 460 nm, the refractive index is 1.55 and the transmittance is 97.8%. Typical silicone resins have RI of ~ 1.4. The high RI of OE-6630 silicone is attributed to the phenyl groups in the polymer chain (RI = 1.53).

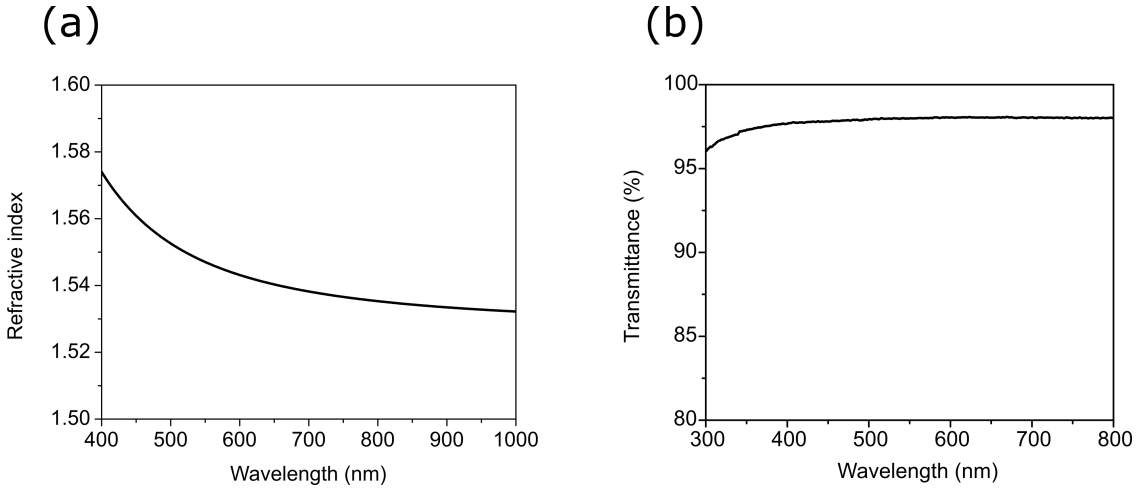

Figure 2-3. (a) Refractive index and (b) transmittance of neat silicone resin.

The silicone resin cures via the following hydrosilylation reaction catalyzed by a Pt complex (Figure 2-4) [155], [156]:

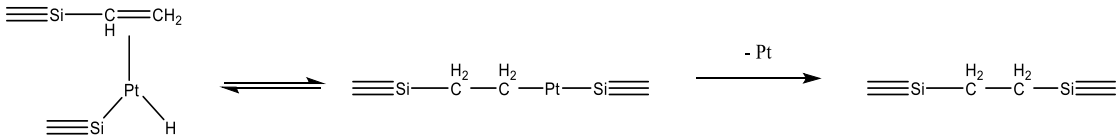

Figure 2-4. Mechanism of silicone crosslinking reaction. Pt ligands and Si substituents are omitted for clarity, and ≡ represents the remaining valence on Si.

In the first step, oxidative addition of ≡Si-H on Pt catalyst takes place, and then H transfer on the C=C double bond and reductive elimination of the product follows [157]. The overall hydrosilylation addition reaction is (Figure 2-5):

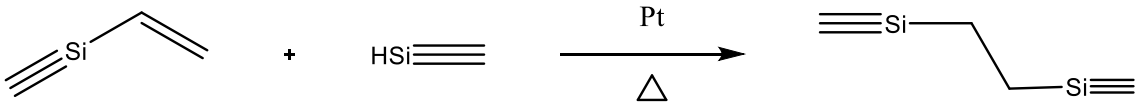

Figure 2-5. Silicone crosslinking by hydrosilylation. Si substituents are omitted for clarity and ≡ represents the remaining valence on Si.

Curing conditions for the silicone resin were studied using DSC. It is known that the hydrosilulation reaction is associated with a strong exotherm [158]. The neat silicone sample showed an exothermic peak with peak onset at 85.45°C, peak just below 100˚C and the total enthalpy of reaction 135.6 J/g (Figure 2-6). The curing scan indicate that the crosslinking reaction can be completed by the curing schedule of 150˚C for 1 hour.

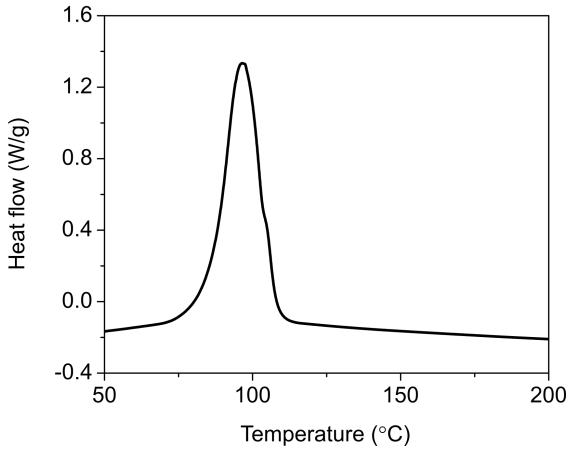

Figure 2-6. DSC scan of the crosslinking reaction of silicone resin.

2.3.2 Two-step, hydrothermal TiO_2 preparation

Under ambient conditions, TiO_2 can exit in three different phases: anatase, brookite, and rutile. The RI and band gap for the three phases are listed in Table 2-2. All three phases have band gap > 3 eV. The smallest band gap is 3.03 eV of rutile, and the equivalent wavelength for band excitation is ~ 409 nm. Therefore, it is reasonable to conclude that light absorption in the visible range is minimal for the TiO_2 phases. The RI of brookite and rutile are 2.70 and 2.90 at 589 nm, and that of anatase is slight lower at 2.50.

Table 2-2. RI and band gap of TiO_2 phases [159], [160].

Crystalline phase	RI	Band gap (eV)
Anatase	2.5	3.20
Brookite	2.7	3.19
Rutile	2.9	3.03

The crystalline phase of the synthesized nanoparticles was determined using XRD. By tuning the synthesis condition, the crystalline phase can be controlled [161]. The XRD pattern of as-synthesized TiO_2 nanoparticles prepared by the hydrothermal method is shown in Figure 2-7. The XRD pattern of rutile phase TiO_2 show strong diffraction peaks at 27˚, 36˚, and 54˚. The experimentally obtained diffraction peaks agree with the rutile phase pattern according to the standard pattern (ICDD PDF #01-072-7374). The rutile phase of the synthesized TiO_2 can be attributed to the acidic synthesis environment. In the reaction mixture, Ti^{+4} from the titanium isopropoxide precursor coordinate with the chloride ions in an octahedral structure. The 6M solution of HCl leads to many Cl^- coordinating with Ti^{+4} ion, and the deoxolation between octahedral coordinate structure is dominated by corner-shared bonding, producing rutile phase TiO_2 in the synthesis.

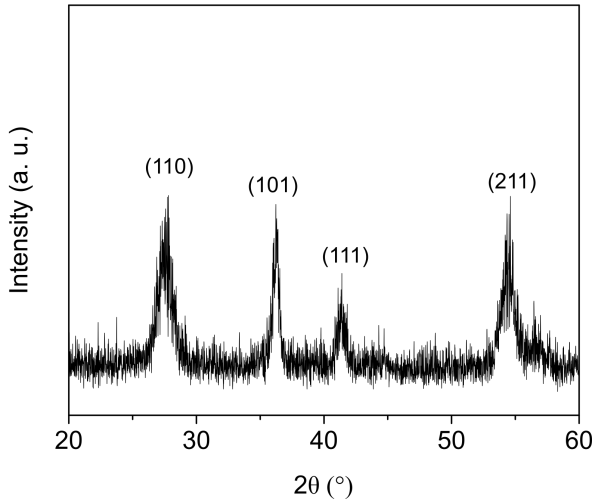

Figure 2-7. XRD of TiO_2 nanoparticles synthesized by hydrothermal method.

Figure 2-8 shows the morphology of the as-synthesized TiO_2 nanoparticles. The nanoparticles show a size distribution ranging from 10 to 20 nm. It is also observed that the dispersion of the nanoparticles was not ideal. Upon mixing with silicone resin, the poorly dispersed nanoparticles would result in large agglomerates in the composite, and light scattering is expected to occur. The surface energy of TiO_2 is about 60 mN/m, while the surface energy of cured and solid polydimethylsiloxane is ranges from 15.7 to 24 mN/m [162]–[164]. The hydrophobic nature of the silicone matrix is not compatible with the hydrophilic TiO_2 surface. When TiO_2 nanoparticles are added to silicone resin without any surface treatments, the incompatible surfaces lead to agglomeration of TiO_2 in the polymer matrix in order to minimize the exposed nanoparticle surface area and minimize the total energy. In TiO_2 – silicone composite, agglomerates larger than 400 nm can be observed,

which is on the same order of the wavelength visible light, and light scattering would result in reduced encapsulant transparency.

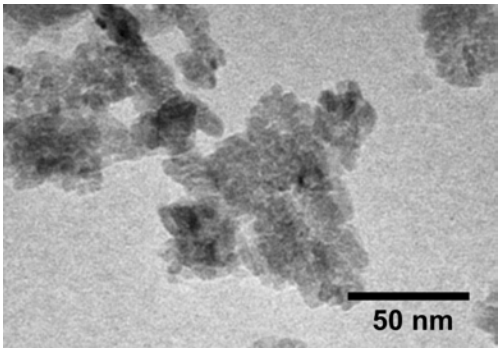

Figure 2-8. (a) As-synthesized TiO_2 nanoparticles dispersed in ethanol.

To make the TiO_2 surface more compatible with the silicone resin matrix, surface modifications on the nanoparticles is needed to reduce the surface energy of the inorganic nanoparticles. More specifically, low-surface energy surfactants consisted of hydrocarbon or fluorocarbon chains are preferable. At room temperature, the surface tensions of fluorosurfactant aqueous solutions have been reported to range from 14 to 27 mN/m, and those of hydrocarbon surfactants range from 20 to 38 mN/m, with longer tail length having lower surface energy [165]–[167]. The surface energy difference can be attributed to the molecular structures of fluorosurfactant and hydrocarbon surfactants. The low surface tension of hydrocarbons stems from the low intermolecular forces (London dispersion and van der Waals forces). Compared to hydrogen, fluorine has a larger size, much stronger electronegativity, and smaller polarizability, resulting in the very strong C-F bond that gives fluorocarbons strong chemical and thermal resistance. The low polarizability of

fluorine gives weak London forces between fluorinated chains, since London forces-derived energy varies with the square of polarizability [168]. So low cohesive energy and low surface tension result [165]. Comparing different functional groups, it is known that the surface energy decreases for hydrocarbons and fluorocarbons in the order of CH_2 > CH_3 > CF_2 > CF_2H > CF_3 [169]–[172]. However, although fluorocarbon gives lower surface energy than the hydrogenated counterpart, additional considerations present in the selection of the surfactant for TiO_2 nanoparticle. The RI of the surfactant should be considered for the preparation of high-RI encapsulant, and the interfacial adhesion and compatibility with the polymer resin should be considered for nanoparticle dispersion. Comparing silane molecules with hydrocarbon and fluorocarbon tails of the same carbon chain length, it is found that the fluorinated silanes have lower RI of 1.31 – 1.35 whereas that of hydrogenated chains have RI of 1.43 – 1.45. Because the RI of fluorosilanes are significantly lower than that of hydrogenated silanes, and fluorinated chains have poor interactions with the silicone resin, silane with long chain, eight-carbon hydrocarbon functional group is selected as the surfactant in the modification of TiO_2 nanoparticles in this study. More specifically, vinyl-terminated silane is selected in this study because the vinyl terminal can participate in the crosslinking reaction of the silicone matrix to improve the filler-matrix interactions.

The vinyl-modified TiO_2 nanoparticles can form covalent bonding with the silicone resin, thus enhancing the adhesion at the filler-matrix interface. The surface modifier also improves the interaction of TiO_2 with silicone to help better disperse the nanoparticles in the polymer matrix. As Figure 2-9 shows, the dispersion of the nanoparticles was improved

after the nanoparticle surfaces were treated with 7-octenyltrimethoxysilane because of reduced surface tension of TiO_2 nanoparticles and enhanced interfacial interactions with the polymer matrix. However, nanoparticles clusters smaller than 50 nm were still observed, because stirring and sonication were not able to break up the clusters after they form during synthesis.

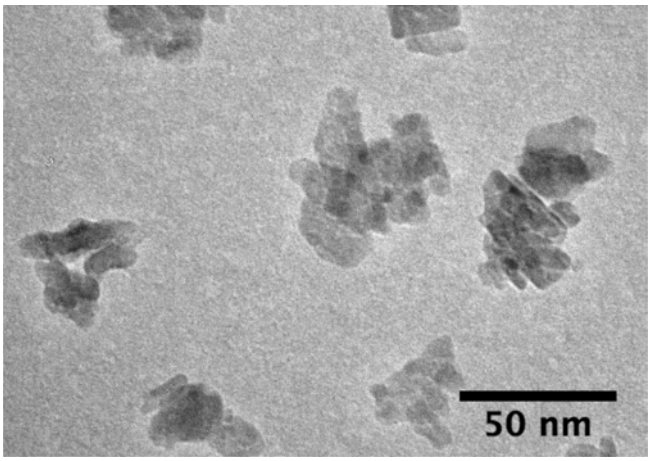

Figure 2-9. TiO_2 nanoparticles after surface treatment with 7-octenyltrimethoxysilane and solvent exchange to toluene.

The crosslinking reaction of TiO_2-incorporated nanocomposites were studied using DSC. It was found that the incorporation of TiO_2 nanoparticles does not have significant effect on the curing of the encapsulant. The 10 wt.% loading nanocomposite is shown to represent the filled nanocomposite samples (Figure 2-10). The curing peak shows the same shape as that of the neat resin, and the normalized enthalpy of reaction (124.6 J/g) is also close to that of neat silicone resin (136.5 J/g). Therefore, the same curing schedule is used to cure the nanocomposites.

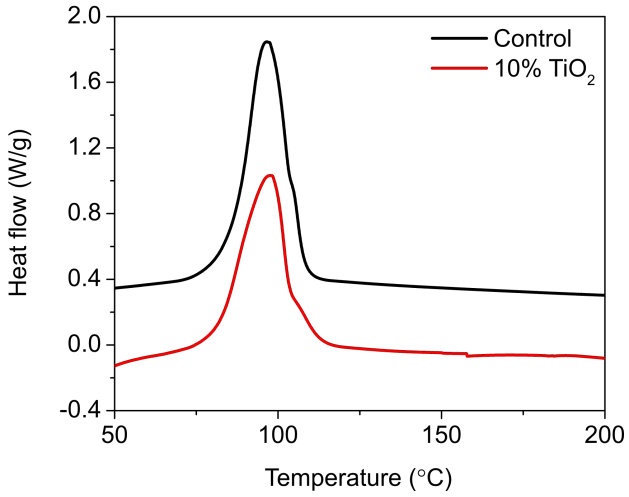

Figure 2-10.DSC scans of nanocomposite and neat silicone resin.

The optical properties of nanocomposite with silane-treated TiO_2 nanoparticles were studied. The filler loadings of the nanocomposites range from 5 to 30 wt.%. Figure 2-11 shows the refractive indices of the nanocomposites as a function of wavelength from 400 to 1,000 nm. It is clear that the refractive index of the encapsulant film increases with the amount of incorporated TiO_2 nanoparticles. The refractive indices of the encapsulants at the blue LED wavelength of 460 nm is summarized in Table 2-3. Increasing the filler loading from 0 to 30 wt.%, the refractive index was increased by nearly 0.25, equivalent to a 16% enhancement compared to the neat silicone. Using LEE ratio as defined by Mont *et al.* and discussed earlier [173], the large enhancement in refractive index is expected to give four times the improvement in LEE ratio for GaN LED with refractive index of 2.5 compared to a package where the light is directly emitted to air (RI = 1). Compared with

typical encapsulants (RI = 1.4-1.5), the nanocomposite with n = 1.806 is expected to double the LEE ratio.

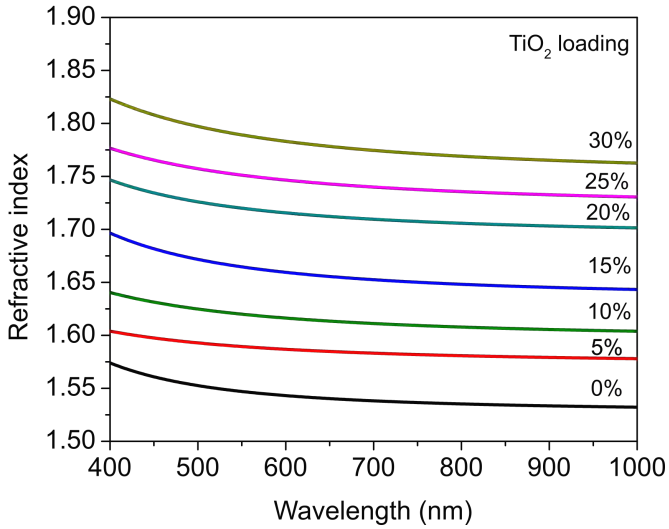

Figure 2-11. Refractive indices as a function of incident light wavelength for TiO_2 nanocomposites containing 0-30 wt.% TiO_2.

Table 2-3. Refractive indices of TiO_2 nanocomposites at 460nm. Relative RI was obtained by taking the ratio of the RI of the composite to that of the neat silicone resin (OE 6630).

Sample	**RI**	**Relative RI (%)**
OE6630	1.559	-
5% TiO2	1.596	102
10% TiO2	1.630	105
15% TiO2	1.679	108
20% TiO2	1.732	111
25% TiO2	1.764	113
30% TiO2	1.806	116

The optical transparency of the nanocomposites in the wavelength region from 400 to 800 nm were characterized using encapsulant-coated glass slides (Figure 2-12). The nanocomposite containing 5 wt.% TiO_2 exhibit > 80% transparency. However, the rest of encapsulants, containing 10-30 wt.% of TiO_2, showed unsatisfactory optical transmittance results. The transmittance at 460 nm is 53.3% at 10 wt.% filler loading, and below 20% at higher filler loadings. Considering that the nanocomposite is designed as an optical encapsulant, light transmittance is of great significant for its application. Therefore, the nanocomposite with reasonable transparency (> 80% at 460 nm) is limited to RI below

1.65. Compared to the initial RI of 1.56 of neat silicone resin, the increased RI improves the LEE ratio from ~2.6 to nearly 3.

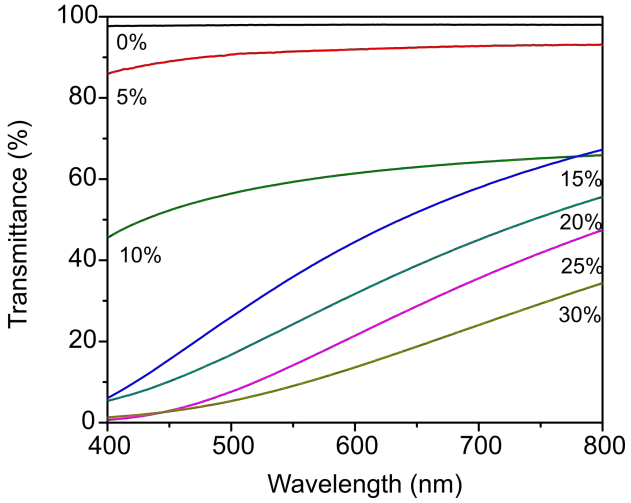

Figure 2-12. Optical transmittance results of TiO_2 nanocomposites containing 0-30 wt.% TiO_2. Neat resin (0% filler) is labeled as control sample.

Table 2-4. Optical transmittance of TiO_2 nanocomposites at 460nm. Relative transmittance was obtained by taking the transmittance ratio of the composite to the reference (OE6630).

Sample	**Transmittance (%)**	**Relative transmittance (%)**
OE6630	97.8	-
5% TiO2	89.4	91.4
10% TiO2	53.3	54.5
15% TiO2	17.6	18.0
20% TiO2	11.4	11.7
25% TiO2	3.7	3.8
30% TiO2	3.2	3.3

Coatings of the nanocomposites were tested for reliability by thermal cycling under high moisture environment (90-96 R.H.). The temperature cycled between 65°C and -10°C for 500 hours. The changes in transparency and RI after the reliability test were monitored. The 15 – 30 wt.% loaded encapsulants are not reported here due to their low initial transmittance. The reliability test results are shown in Figure 2-13 and Table 2-5. The reference sample (0% loading) showed negligible change in RI at 460 nm, and the 5 wt.% and 10wt.% loaded samples showed ≤ 2% decrease in RI after the reliability test. Figure 2-14 shows that the largest decrease in transmittance after reliability test was below 2%. Reliability test results suggest that the incorporation of TiO_2 nanoparticles into silicone resin does not have adverse effects on the long-term performance of the encapsulants.

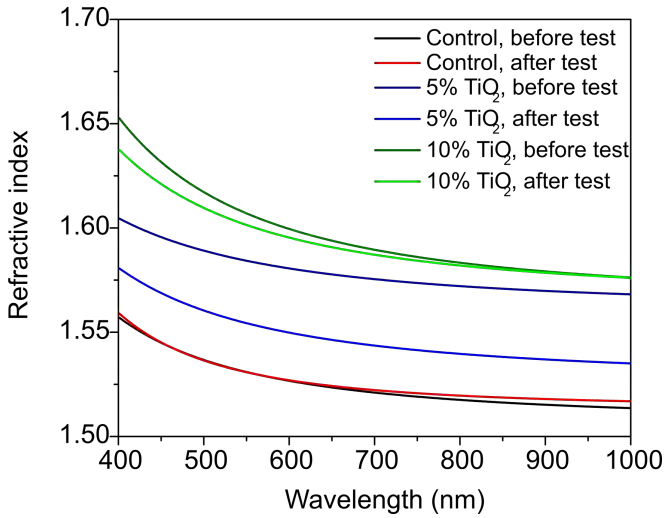

Figure 2-13. Refractive indices of the composites before and after 500 hours of reliability test.

Table 2-5. Refractive indices of TiO_2 nanocomposites at 460 nm. Relative RI was obtained by taking the ratio of the RI of the composite to that of the reference.

Loading	**Sample**	**RI**	**Relative RI (%)**	**RI change (%)**
0%	As prepared	1.54	100.0	0
	500h reliability test	1.54	100.0	
5% TiO2	As prepared	1.59	103.2	- 2.0
	500h reliability test	1.56	101.2	
10% TiO2	As prepared	1.63	105.8	- 1.3
	500h reliability test	1.61	104.5	

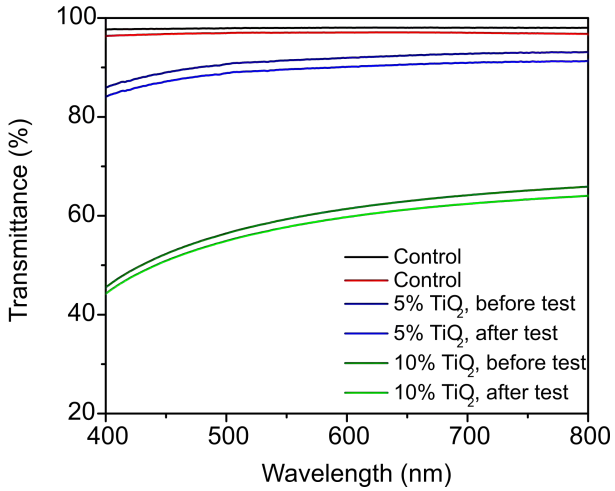

Figure 2-14. Transmittance of TiO_2 nanocomposites before and after 500 hours of reliability test.

Table 2-6. Optical transmittance of TiO_2 composites at 460 nm. Relative transmittance was obtained by taking the ratio of the RI of the composite to that of the reference.

Loading	**Sample**	**Transmittance**	**Relative T (%)**	**T change (%)**
0%	As prepared	97.3	100.0	- 0.5
	500h reliability test	96.8	99.5	
5% TiO_2	As prepared	89.3	91.7	- 1.7
	500h reliability test	87.6	90.0	
10% TiO_2	As prepared	53.9	55.4	- 1.2
	500h reliability test	51.8	53.2	

We show that the incorporation of TiO_2 nanoparticles into silicone resin increases the RI of the composite. The reason is attributed to the high RI of rutile phase TiO_2 synthesized in the hydrothermal reaction. However, the optical transparency remains a challenge especially for highly loaded nanocomposites. It is suspected that nanoparticle dispersion is the reason for the low transmittance at high filler loadings. Imperfect dispersion of nanoparticles leads to agglomerations that easily scatter light and reduce transmittance. Results suggest filler size and dispersion control is not ideal. The current TiO_2 preparation method has separate synthesis and surface modification steps, and nanoparticles can easily agglomerate after being synthesized and before surfactant treatment. Therefore, we propose to improve the size control and filler dispersion by combining the synthesis and surface modification steps. The results will be presented in the next section.

2.3.3 One-step TiO_2 preparation with in-situ surface functionalization

We used an alternative synthesis method where surface functionalization is performed during synthesis, thus "*in-situ*" functionalized. The same surfactant molecule (7-octenyltrimethoxysilane) as in the two-step method is used here. The synthesis condition is modified in two ways: 1) continuous stirring to prevent particle settling and agglomerate formation, and 2) low Ti^{+4} precursor concentration for slow nanoparticle growth. The modified process has the advantages of better nanoparticle size control and improved dispersion.

The synthesized nanoparticles were characterized using XRD and TEM to determine their crystalline phase, and size distribution and dispersion, respectively. The nanoparticles are mainly brookite TiO_2, with observed diffraction peaks at 25˚, 31˚ and 36˚ matching those assigned to the brookite phase of TiO_2 (ICDD PDF #00-016-0617) (Figure 2-15). Although the RI of brookite TiO_2 is lower than that of the rutile phase by 0.2 at 589 nm, the difference is relatively small and it is possible to compensate for the lower filler RI with higher transparency. Indeed, TEM observations show that the synthesized TiO_2 nanoparticles are both smaller and better dispersed than those prepared using the two-step method (Figure 2-16). The nanoparticles are ~ 10 nm in diameter, which is much smaller than the wavelength of the LED light, thus minimizing light scattering. In comparison, the method discussed earlier produced TiO_2 nanoparticles of 10 – 20 nm. The smaller particle size helps to minimize Rayleigh scatting, and improved nanoparticle dispersion helps to maintain the cluster size below 40 nm, which is the cluster size threshold for transparent composite.

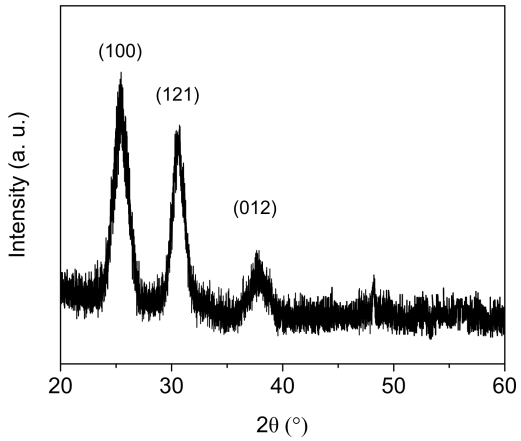

Figure 2-15. XRD pattern of TiO_2 synthesized using the *in-situ* surface modification method.

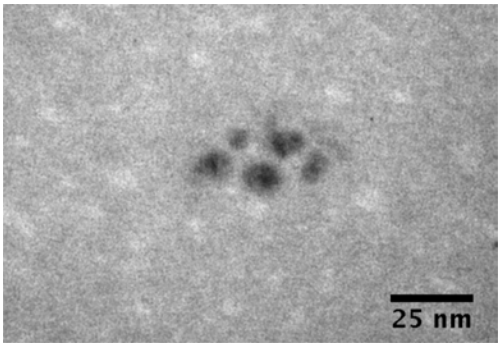

Figure 2-16. TEM image of synthesized TiO_2 dispersed in toluene.

After the TiO_2 nanoparticles were added to silicone resin, the curing behavior of the nanocomposite was examined using DSC. The curing profile of 10 wt.%-filled nanocomposite suggest that the incorporation of TiO_2 fillers does not significantly affect the curing reaction of the polymer matrix (Figure 2-17), and the same curing schedule as the neat silicone resin was used.

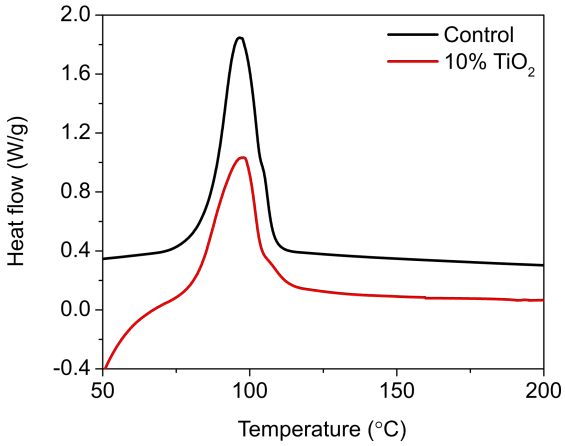

Figure 2-17. DSC curing profile of nanocomposite with 10 wt.% of *in-situ* synthesized TiO_2.

Nanocomposite coatings on Si substrates were characterized for RI using ellipsometry. Because the synthesis method uses low precursor concentration in the reaction mixture, TiO_2 yield was lower than that for the two-step synthesis method, and the filler loading level was limited to 10 wt. %. The RI of nanocomposite with 5 wt.% filler is 1.63 at 460 nm, and continues to increase with increasing filler loading. The encapsulant material with a 10 wt.% filler loading further improved the RI up to 1.71, which is about 10% increase compared to the silicone resin (RI = 1.56) (Figure 2-18 and Table 2-7). In LED packages using GaN LED (RI = 2.5), LEE ratio is expected to increase by more than threefold compared to a package with no encapsulant.

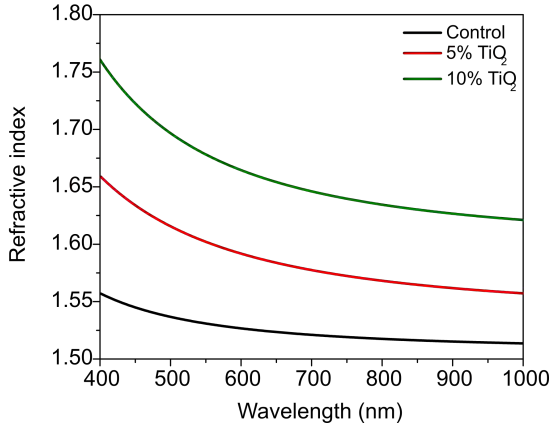

Figure 2-18. Refractive indices for TiO_2 nanocomposites containing 0 – 10 wt.% TiO_2 in the wavelength range of 400 – 1,000 nm.

Table 2-7. Refractive indices at 460 nm for nanocomposites with 0 – 10 wt.% TiO_2.

Sample	**RI**	**Relative RI (%)**
OE6630	1.56	-
5% TiO2	1.63	106
10% TiO2	1.71	110

Using the *in-situ* surfactant modification method that gives well-dispersed nanoparticles of smaller diameter, highly transparent nanocomposite material can be prepared. Figure 2-19 shows the optical transmittance of the encapsulant material in the wavelength rage of 300 – 800 nm and Table 2-8 summarizes the transmittance at of our material with different filler loading levels at 460 nm. With 5 – 10 wt.% TiO_2, the

nanocomposites showed > 87% transmittance in the visible spectrum range, which is equivalent to 90% relative transmittance. Compared to the encapsulants prepared with two-step synthesized TiO_2, the nanoparticles fabricated with the *in-situ* method are better dispersed in the matrix and can greatly reduce the change of Rayleigh scattering. Therefore, optical transmittance is improved. Because the material is highly transparent, it is suitable as a LED encapsulation material.

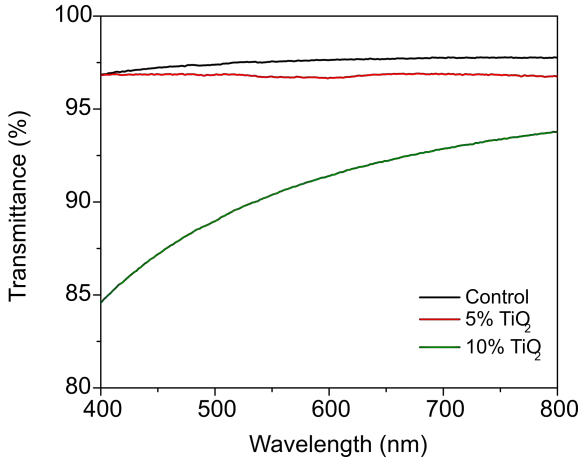

Figure 2-19. Optical transmittance of encapsulants in the wavelength range of 300 to 800 nm.

Table 2-8. Optical transmittance of TiO_2 composites at 460 nm. Relative transmittance was obtained by taking the ratio of the RI of the composite to that of the reference.

Sample	**Transmittance (%)**	**Relative transmittance (%)**
OE6630	97.3	-
5% TiO_2	96.8	99
10% TiO_2	87.6	90

The encapsulants were subjected to accelerated reliability test with the same test conditions as previously described. It was found that the optical transparency of the material was hardly affected by the reliability test, with < 2% change measured at 460 nm (Figure 2-20 and Table 2-9). For RI, the nanocomposite material showed a < 1.5% decrease after the temperature-humidity test (Figure 2-21 and Table 2-10). The results of reliability test suggest that the TiO_2 – silicone nanocomposites have long-term stability in their optical performances and are good candidates as LED encapsulants.

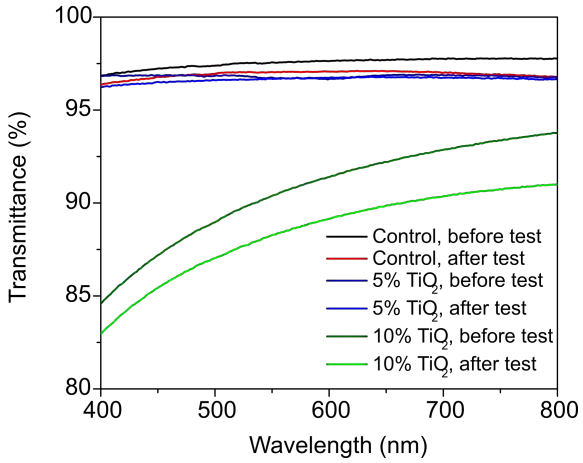

Figure 2-20. Optical transmittance of TiO_2 nanocomposites.

Table 2-9. Optical transmittance of TiO_2 composites at 460 nm. Relative transmittance was obtained by taking the ratio of the RI of the composite to that of the reference.

Loading	**Sample**	**Transmittance**	**Relative T (%)**	**T change (%)**
0%	As prepared	97.3	100.0	- 0.5
	500h reliability test	96.8	99.5	
5% TiO_2	As prepared	96.8	99.4	- 0.3
	500h reliability test	96.5	99.1	
10% TiO_2	As prepared	87.6	90.0	- 1.9
	500h reliability test	85.8	88.1	

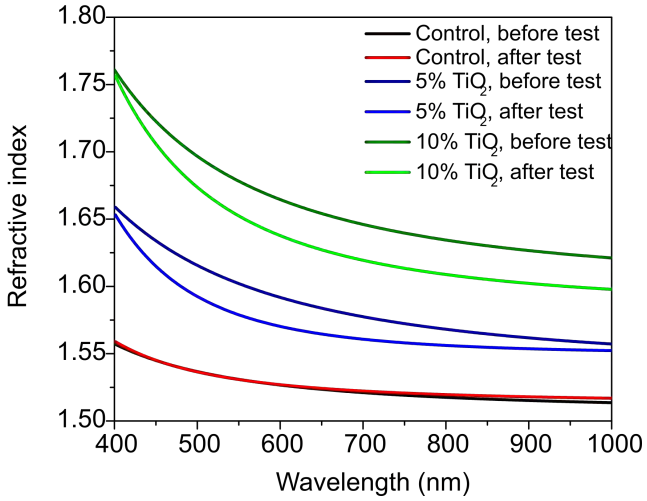

Figure 2-21. Refractive index of nanocomposites.

Table 2-10. Refractive indices of TiO_2 nanocomposites at 460 nm. Relative RI was obtained by taking the ratio of the RI of the composite to that of the reference.

Loading	**Sample**	**RI**	**Relative RI (%)**	**RI change (%)**
0%	As prepared	1.54	100.0	0
	500h reliability test	1.54	100.0	
5% TiO2	As prepared	1.63	105.8	- 1.3
	500h reliability test	1.61	104.5	
10% TiO2	As prepared	1.71	110.4	0
	500h reliability test	1.70	110.4	

2.4 Conclusion

TiO_2 nanoparticles were synthesized using two methods. In the first method with two steps, hydrothermal reaction of Ti^{+4} precursor gave rutile TiO_2 nanoparticles of 10 – 20 nm diameter, and the particles were surface modified with silane surfactant in a subsequent reaction. In the second method where TiO_2 nanoparticle synthesis and surface treatments were carried out simultaneously, smaller particles (10 nm) of brookite phase and with improved particle dispersion were fabricated. Encapsulants were prepared by incorporating the synthesized TiO_2 nanoparticles into silicone resin. With the well-dispersed TiO_2 in silicone, > 90% optical transparency was achieved at the GaN LED emission wavelength of 460 nm, and the RI of encapsulant reached 1.73, which is expected to improve light extraction efficiency of LED packages by threefold. Furthermore, the nanocomposites showed good reliability under high humidity temperature cycling conditions. This study reports the effect of filler preparation on the performance of nanocomposites, and the highly transparent and high-RI encapsulant material reported here has potential for applications in LED packaging.

CHAPTER 3. ENHANCED FILLER-MATRIX INTERPHASE PROPERTIES VIA TWO-LAYER FILLER SURFACE MODIFICATION

3.1 Introduction

Epoxy-based composites are widely used as encapsulants, adhesives, and interface materials in electronic packages, for epoxy offers a number of material advantages in the areas of superior adhesion, processability, mechanical and electrical properties, and low cost [174]–[176]. Spherical silica particles are often incorporated into epoxy resin for enhanced rheological control, fracture resistance, dimensional stability, and thermomechanical compatibility with the package structure [177]–[180]. As package size shrinks with the trend of microelectronic miniaturization and multi-functionalization, the dimension of the silica particles used in the epoxy composites are also required to shrink in order for the composite to flow into smaller gaps [110], [181], [182].

Compared to the introduction of micro-size fillers into polymer resins, the introduction of nanoparticle fillers results in several orders of magnitude increase in the filler-matrix interfacial area in the composite, and the effect of filler-matrix interphase properties on the bulk material properties of the nanocomposite is dramatically amplified [63], [183], [184]. Because of the large volume of interphase region in nanocomposites, the attractive or repulsive interactions between filler and polymer chains can have a significant impact on filler dispersion, and composite glass transition temperature (T_g),

viscosity, mechanical properties, and shelf life [68], [79], [80], [185]. Specifically, attractive interactions at the filler-matrix interface can lead to large positive T_g deviation in nanocomposites relative to the bulk polymer by chain immobilization in the interphase, and repulsive interactions result in free surfaces and result in negative T_g deviations [186], [187]. When attractive filler-matrix interactions are present, the polymer chains in contact with the filler surface are partially immobilized in the interphase region, leading to changes in mechanical properties, such as reduced thermal expansion and increased modulus [69]. Furthermore, because cracks often propagate along weakly interacting filler-matrix interfaces, surface-treated fillers have shown to enhance the yield stress, fracture energy release rate, and strain energy of polymer composites when the interfacial interactions are improved [188]–[190].

In this study, well-controlled filler-matrix interphase and additional functionality of improved composite toughness are demonstrated via a two-layer silica filler surface modification method. The inner layer of reactive silane molecules serve as the coupling agent for the grafting of the outer polydimehylsiloxane (PDMS) layer (Figure 3-1), and the soft segment-containing outer layer acts as a toughening agent while also increasing the volume of the interphase. Surface wetting properties and chemical analyses show the successful surface modifications on the silica surface, and the silica fillers are well-dispersed as show by light scattering and transmissions electron microscopy (TEM) results. The silica fillers were introduced to epoxy resin to fabricate epoxy nanocomposites with silica fillers of pristine, silanized, or PDMS surfaces at different loadings. The thermal and

thermomechanical properties of the nanocomposites including curing behavior, T_g, and thermal expansion are studied, and fracture and toughness behaviors are investigated.

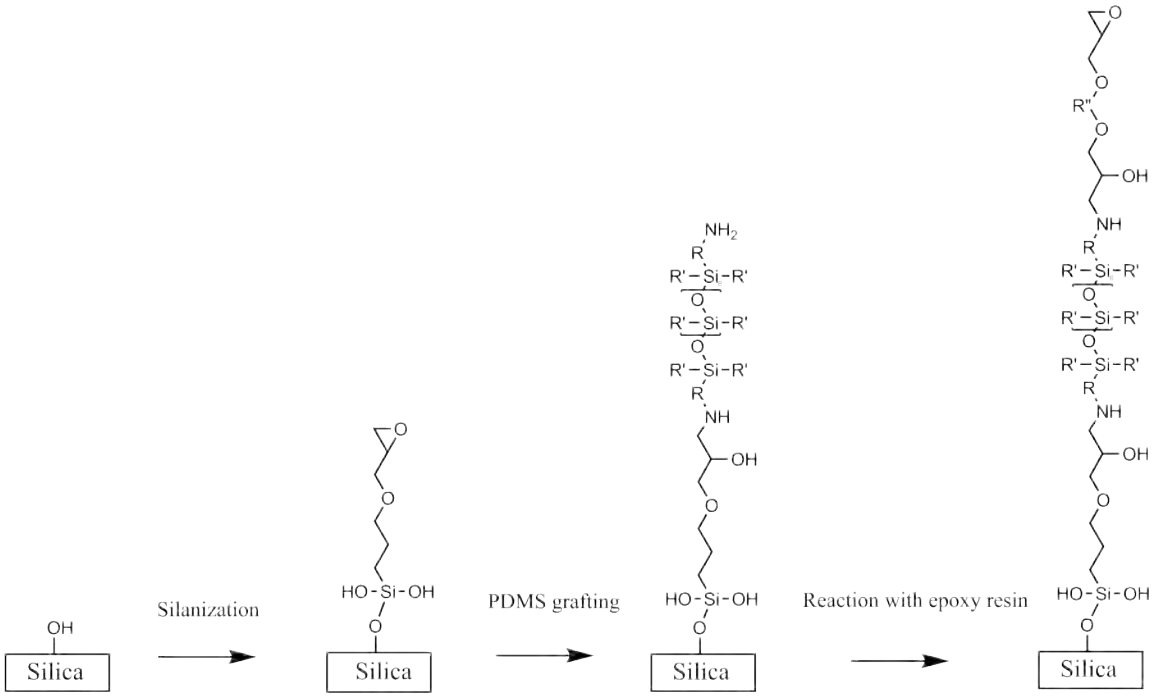

Figure 3-1. Reaction of epoxy-terminated silane and amine-terminated PDMS.

3.2 Method

Epoxy resins 3,4-epoxy cyclohexylmethyl- 3,4-epoxy cyclohexyl carboxylate (ERL-4221E) and diglycidyl ether of bispenol A (Epon 828) were obtained from Synasia and Shell Chemicals, respectively. Curing agent hexahydro-4-methylphthalic anhydride (HMPA, Lindride 52D) was obtained from Lindau Chemicals, and curing catalyst 1-cyanoethyl-2-ethyl-4-methylimidazole was obtained from Sigma-Aldrich. Silica nanoparticles of 100-200 nm diameter (KE-P10) were obtained from Nippon Shokubai,

Japan. (3-glycidyloxypropyl)trimethoxysilane (GPTS, 98%) was obtained from Sigma-Aldrich, and aminopropyl-terminated polydimethylsiloxane (PDMS, molecular weight 850-900) was obtained from Gelest. Deionized (DI) water was produced from a Barnstead Smart 2 Pure Water Purification system (Thermo Scientific). Ethanol (Sigma Aldrich), formic acid (88%, BDH), acetone (BDH), isopropanol (BDH), hydrogen peroxide (30 % w/w, VWR), and sulfuric acid (96%, J. T. Baker) were used as received.

GPTS is grafted onto the surface of silica using a method modified from elsewhere [191]. In a typical process, 10 g silica powder was dispersed in a 100 g mixture containing 95% ethanol and 5% water by stirring and sonication. 0.50g of GPTS was added to the dispersion and the solution was adjusted to pH 4-5 by formic acid. The dispersion was refluxed at 100˚C for 24 hours, and GPTS-silica nanoparticles were rinsed three times with ethanol. The PDMS grafting reaction is modified from a method reported elsewhere [192]. Briefly, 10 g GPTS-silica is dispersed in 100 g ethanol, and 2 g of PDMS was added to the dispersion. The mixture was refluxed at 100˚C for 24 hours, and reacted silica was rinse three times with ethanol and dispersed in acetone prior to mixing with the epoxy resin.

Epoxy resins ERL-4221E and Epon 828 were mixed at 1:1 molar ratio by equivalent epoxide weight. Silica dispersion in acetone was added to the epoxy resin at the desired filler loading level and mixed by stirring and sonication, and acetone was removed by vacuum at elevated temperature. Curing agent was added to the mixture at the ratio of 1:0.88 weight ratio of epoxy:curing agent. Curing catalyst was added to the mixture at the ratio of 1% by weight to the mixed epoxy-curing agent resin mixture. The nanocomposite was cured at 150˚C for one hour.

Thermal-oxidized silicon wafers were used for x-ray photoelectron spectroscopy (XPS) and contact angle characterizations. (100) silicon wafers were thermally oxidized to produced silicon dioxide on the surface, and were cleaned by acetone, isopropanol, and dried with nitrogen. The wafers were subsequently cleaned in Piranha solution (1:3 volume ratio of H_2O_2 and H_2SO_4 at 120˚C for 10 min to remove organic residues, and rinsed with water and dried with nitrogen. Si wafers were immersed for one day at 85˚C in an ethanol-water solution containing the same concentration of GPTS and formic acid as used in the particle treatment, and were subsequently immersed for one day at 85˚C in ethanol solution containing the same concentration of PDMS as used in the particle treatment. Surface-treated wafers were cleaned with ethanol.

The chemical states on the sample surfaces were analyzed using x-ray photoelectron spectroscopy (XPS, Thermo K- Alpha) using the monochromic Al Kα line with photon energy of 1486.6 eV. Reaction heats were analyzed using differential scanning calorimetry (Q2000 DSC, TA Instruments) in nitrogen atmosphere. A dynamic DSC procedure with about 10 mg sample and a ramping rate of 10˚C/min under nitrogen atmosphere was used. DSC T_g were measured using modulated mode, with modulation amplitude of 1˚C and modulation period of 30 sec. The reversible heat signal was used for T_g analyses. Water and epoxy contact angles were measured using a contact angle measurement system equipped with a Rame-Hart goniometer and a built-in CCD camera. The test liquid size was 2 μL. A Hitachi HT7700 TEM was used to characterize filler dispersion. Silica fillers were dispersed in solvent using sonication, and then the dispersion was dropped onto copper TEM grid and dried prior to analysis. A Zetasizer (Melvern

Instruments, Nano ZS) was used to measure size distribution of silica fillers in solvent. A thermogravimetric analyzer (Q5000 TGA, TA Instruments) was used to measure mass loss and filler loading under nitrogen atmosphere. Ramping rate of 10˚C/min and sample size of about 10 mg were used. Glass transition temperatures of cured underfill samples were characterized using a dynamic mechanical analyzer (Q800 DMA, TA Instruments) with the single-cantilever bending mode, a ramping rate of 3˚C/min, and 1 Hz under air atmosphere. The peak temperature of tan delta curve was taken as the DMA T_g temperature. A thermomechanical analyzer (Q400 TMA, TA Instruments) was used to measure the volume expansion of the nanocomposites using a quartz expansion probe. Cured nanocomposites were polished to ~ 1 mm thickness, and within 0.1 mm thickness difference across the sample surface. Samples were heated from 35 to 250°C at 5°C/min under nitrogen atmosphere and 0.050 N force. and the coefficients of thermal expansion (CTE) were obtained from the slope of the expansion curves below the glass transition region. Scanning electron microscopy (SEM) images were obtained using a Hitachi SU8010 FE-SEM using an acceleration voltage of 5 kV. Nanocomposite samples were gold-sputtered prior to SEM analyses. Nanocomposite samples were gold-sputtered prior to SEM analyses. Naonindentation (Hysitron TriboIndenter) with a Berkovich diamond probe was used to characterize the response of nanocomposites under mechanical stress. The loading function is a trapezoid function with 10 s holding at the maximum load of 1 N. Flat nanocomposite samples were polished with 800 grit and 1200 grit SiC sanding papers and 0.05 μm aAl_2O_3 slurry prior to indentation tests.

3.3 Results and discussion

3.3.1 Nanoparticle surface modifications

The validity of the two-step surface modification reaction was examined using DSC, and the reactions were confirmed with contact angle, TGA, and XPS analyses. The reaction between silica and GPTS is well-understood [110]. The surface of silica nanoparticles is covered with abundant silanol groups [91], [193], which is used as the reactive site for grafting GPTS via dehydration reaction. The monolayer of GPTS on nanosilica surface lead to exposed epoxide groups, allowing for reaction with PDMS. Dynamic DSC scans show an exothermic peak onset at 83˚C and peak at 125˚C corresponding to the PDMS grafting reaction (Figure 3-2). The surface wettability of untreated and surface-modified oxidized silicon wafers were examined by contact angle measurements using water and epoxy liquids (Figure 3-3). Cleaned silicon dioxide surface has many silanol groups and is very hydrophilic, exhibiting water contact angle of 8.0˚ ± 5.3˚. Due to the hydrocarbon chain and an epoxide end-group in GPTS, and methyl-substituted polysiloxane chain in PDMS, water contact angle increased after surface silanization and subsequent PDMS grafting to 48.0˚ ± 0.8˚ and 66.8˚ ± 0.6˚, respectively. The PDMS chain is even more hydrophobic than GPTS, and therefore, PDMS-grafting lead to an even higher contact angle. On the other hand, epoxy contact angles on silicon oxide show a different trend. Clean silicon dioxide surface showed an epoxy contact angle of 32.7˚ ± 3.9˚. Moderate epoxy wettability was observed on silanized and PDMS-grafted silicon dioxide surfaces, which exhibited epoxy contact angles of 29.5˚ ± 3.9˚ and 34.7˚ ± 3.4˚, respectively. Surface wettability difference is further supported by TGA results. Dynamic TGA scans of untreated and surface-modified nanosilicas from ambient to 900˚C

show different weight loss behaviors of nanosilicas (Figure 3-4). Compared with surface-modified nanosilica, untreated nanosilica is most hydrophilic and absorbs the most amount of moisture when stored in ambient environment, leading to the highest weight loss below 200˚C. Consistent with contact angle measurements, the PDMS-grafted nanosilica showed the smallest weight loss in the moisture loss region (< 200˚C). The residue weights at 900˚C suggest that grafted GPTS contribute to 0.79% of total weight, and grafted PDMS contribute to 0.60% of total sample weight.

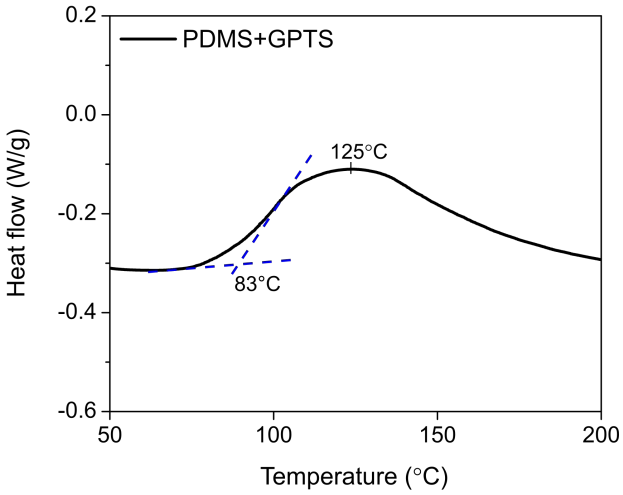

Figure 3-2. DSC scan of GPTS reaction with PDMS.

(a)

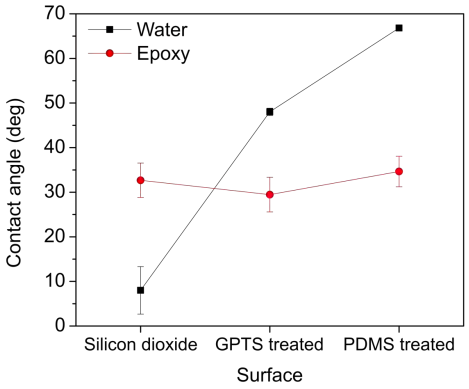

(b)

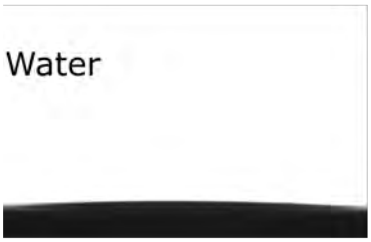

SiO_2

(e)

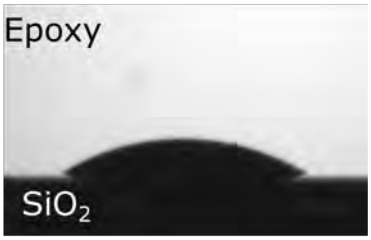

(c)

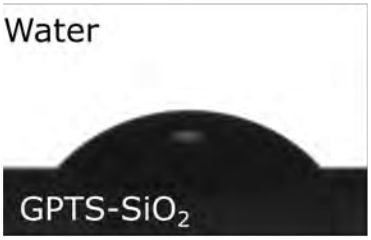

(f)

(d)

(g)

Figure 3-3. (a) Water and epoxy contact angles on silica surfaces. Contact angle images of water on (b) silica, (c) GPTS-silica, and (d) PDMS-silica, and of epoxy on (e) silica, (f) GPTS-silica, and (g) PDMS-silica.

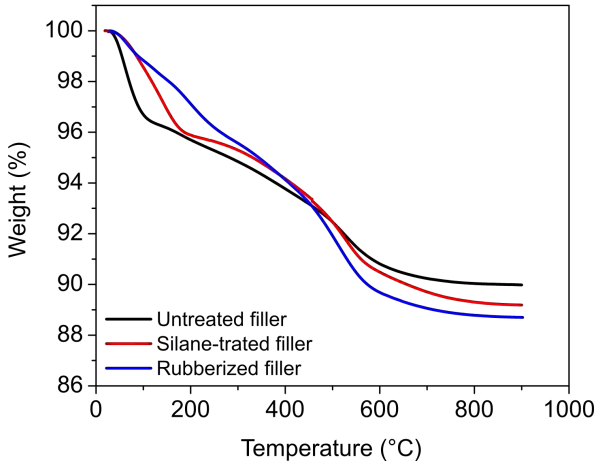

Figure 3-4. TGA scan of pristine silica fillers and surface modified silica fillers.

XPS technique is commonly used to characterize the chemical composition of surfaces. Here, we use XPS to study the chemical groups present on the different silica surfaces, and spectra of pristine, GPTS-grafted, and PDMS-grafted silica are shown in Figure 3-5. The C1s spectrum of pristine silica is dominated by the C-C/C-H peak at 285.0 eV. After GPTS grafting reaction, the area of C-O peak at 286.9 eV significantly increased due to the epoxide group and ether linkages in GPTS. C1s core level XPS on the PDMS-grafted surface also show the peaks corresponding to the same functional groups (C-C/C-H at 285.0 eV, and C-O at 286.9 eV), with an additional C-N peak at 286.1 eV [194], [195]. The area ratio of C-O peak to total C peak decreased from 56% to 12% due to the absence of C-O linkages in PDMS. As shown in Figure 3-5d-e, he surfaces of pristine silica and

GPTS-grafted silica are free of nitrogen. Because the PDMS use in this study is amine-terminated, N1s core level XPS spectra show the fingerprint C-NH_2 peak at 400.0 eV after the PDMS is grafted onto GPTS-reacted silica. (Figure 3-5d-f).

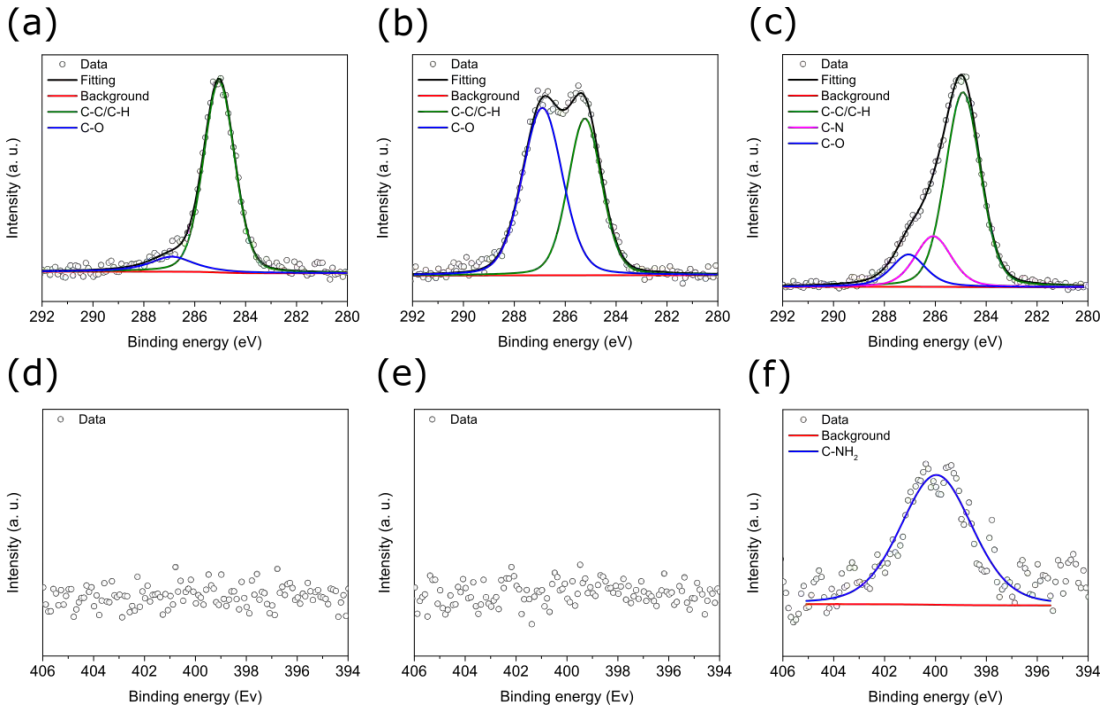

Figure 3-5. XPS C1s spectra of (a) silica, (b) GPTS-grafted silica, and (c) PDMS-grafted silica, and XPS N1s spectra of (d) silica, (e) GPTS-grafted silica, and (f) PDMS-grafted silica.

DLS technique and TEM were used to examine the dispersibility of surface-modified silica nanoparticles. Although the silica nanoparticles are of the size 100-200 nm in diameter, untreated silica nanoparticles are prone to aggregate into clusters larger than 2 μm in diameter (Figure 3-6a, d). The formation of micron-size aggregates can be attributed to the fact that pristine silica is covered with silanol groups, which does not have good

wetting with epoxy or acetone. Moreover, the silanol groups allow silica nanoparticles to form hydrogen bonding with each other. When pristine silica is added to acetone, the solvent used here, the combined effects of moderate solvent wetting to silica and hydrogen bonding between silica result in cluster formation as to minimize surface exposure to the solvent. The introduction of GPTS groups on silica allows silica and solvent to engage in interfacial dipole-dipole interactions, thus enhancing nanoparticle dispersibility. DLS result shows that the average size of GPTS-silica is 157 nm diameter, a narrower size distribution is obtained when compared to that of pristine silica, and no large aggregate is found (Figure 3-6b). TEM observation also supports the conclusion derived from DLS (Figure 3-6e). The short polysiloxane chain of PDMS and the amine terminals allow us to achieve good nanoparticle dispersibility. DLS analysis show a slightly increased average size of 184 nm, and TEM observations also suggest good particle dispersion in solvent (Figure 3-6c, f).

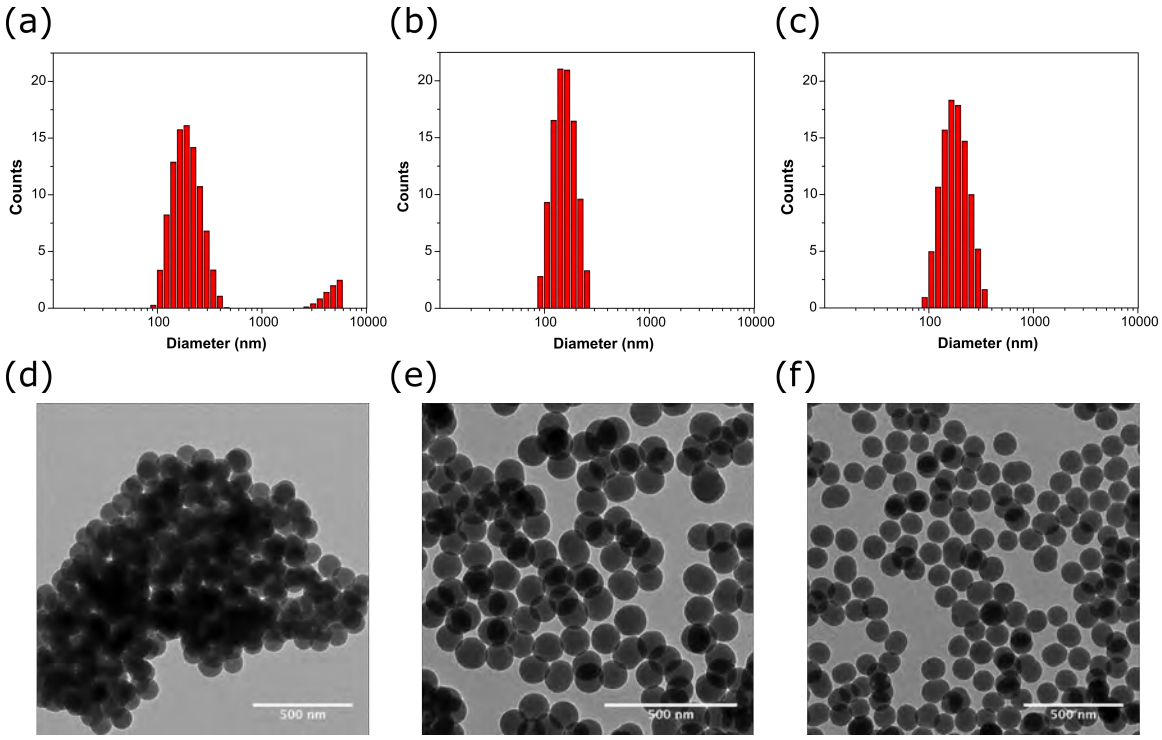

Figure 3-6. DLS particle size distributions of (a) silica, (b) GPTS-grafted silica, and (c) PDMS-grafted silica, and TEM images of (d) silica, (e) GPTS-grafted silica, and (f) PDMS-grafted silica.

3.3.2 Nanocomposites: thermal and thermomechanical properties

The effect of PDMS grafting on the curing, glass transition, thermomechanical, and fracture resistance properties of epoxy nanocomposites are studied. The curing profiles of neat epoxy resin and nanocomposites incorporating GPTS- and PDMS-grafted silica fillers are shown in Figure 3-7a-c. Curing and thermomechanical properties are summarized in Table 3-1. Comparing the different profiles, it is clear that the curing peak temperature is maintained with addition of surface-modified fillers. Although all samples showed an exothermic peak at 151.4 ± 2.4˚C, the normalized enthalpy of curing, $\Delta H_{curing,}$ of

nanocomposite samples slightly decreased when compared to that of neat epoxy resin, and the difference among samples with different filler loadings is insignificant. ΔH_{curing} in neat epoxy resin is 328.3 ± 7.0 J/g, and the that of nanocomposites normalized by filler loading is 296.6 ± 11.7 J/g. ΔH_{curing} in nanocomposites can be attributed to reduced polymer chain mobility by the addition of silica fillers. Because polymer chains are localized by both filler particles and reacted polymers in the 3D space, some functional groups are left unreacted, contributing to the lower total enthalpy of curing.

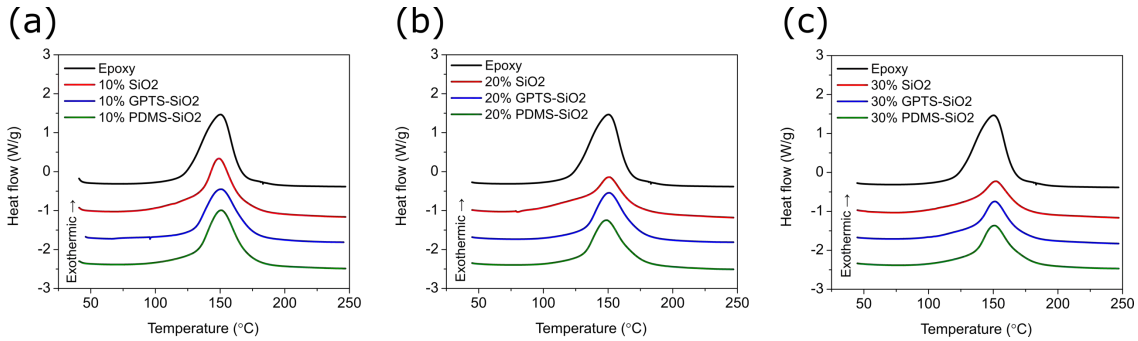

Figure 3-7. DSC scans of curing reactions of epoxy and of nanocomposites with (a) 10 wt.%, (b) 20 wt.%, and (c) 30 wt.% filler loading.

Table 3-1. Thermomechanical properties of epoxy-based nanocomposites

Silica type	Loading (wt.%)	Exothermic peak (˚C)	Heat of curing (J/g)	tan δ Tg (˚C)	CTE below Tg (ppm/K)
	0	150.24	328.30	172.60	64.89
Pristine silica	10	149.56	315.11	174.89	61.46
	20	151.31	285.63	166.31	56.73
	30	152.56	280.86	141.11	47.09
GPTS-silica	10	151.41	292.44	182.80	61.44
	20	151.31	297.38	177.20	55.72
	30	151.73	295.00	169.18	47.38
PDMS-silica	10	151.22	290.63	185.08	52.64
	20	149.40	307.78	189.61	47.06
	30	154.41	303.00	182.65	41.33

The viscoelastic properties of the cured silica-filled nanocomposites were characterized using DMA. Storage moduli of 10 wt.%- filled nanocomposites are shown in Figure 3-8a. The modulus of cured epoxy at 50˚C is 1450 MPa. With added silica, the modulus increases to 2000 – 2700 MPa. The nanocomposite with 10 wt.% untreated silica shows a modulus just above 2000 MPa. When silica fillers are treated with GPTS, the

modulus increases to ~ 2750 MPa. Compared to the pristine silica case, the increased modulus is attributed to larger surface area from uniform filler dispersion, and the improved interface that partially immobilized polymer chains. The load transfer to the stiff silica fillers becomes more efficient, leading to higher modulus [196]. In the PDMS-silica case, the modulus of 10 wt.% filled nanocomposite lies between those corresponding to untreated and GPTS-treated fillers. This observation is attributed to the soft segments in PDMS.

The viscoelastic properties of the cured silica-filled nanocomposites were characterized using DMA. Figure 3-8b shows the changes of loss factor (tan δ) curves as a function of temperature in the range of 40 to 200˚C for the cured neat epoxy resin and the 10 wt.%-filled nanocomposites incorporating silica fillers with different surfaces. The loss factor, also commonly called tan δ, is the ratio of loss modulus to storage modulus, and peak temperature is commonly accepted as one method of determining T_g. Above T_g, the mobility of polymer chains is increased, and bulk material properties such as storage modulus, heat capacity, and CTE are changed dramatically compared to those in the glassy state. As shown in Figure 3-8b, the tan δ peaks of neat epoxy and the 10 wt.% pristine silica-filled nanocomposite are close to each other, and are lower than those of composite containing 10 wt.% surface-modified silica. The highest T_g is found at 185.08˚C for the PDMS-silica nanocomposite, and is about 2.2˚C and 12.5˚C higher than that of GPTS-silica composite and neat epoxy, respectively.

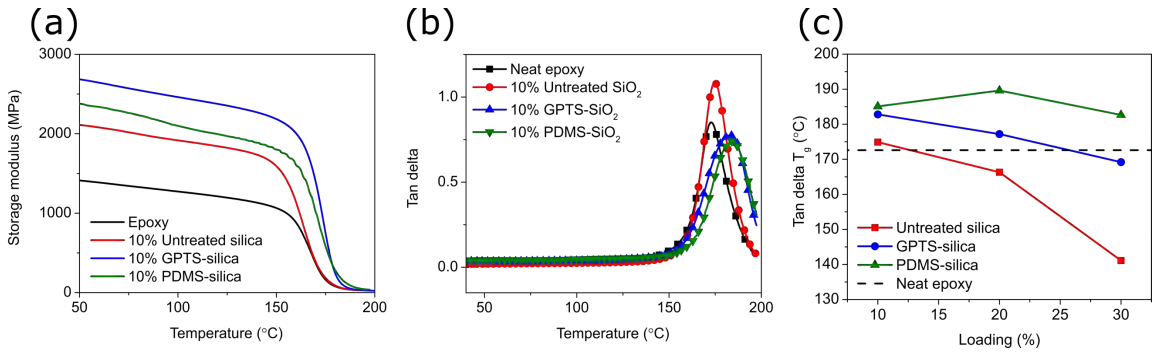

Figure 3-8. (a) Storage moduli of 10 wt.%- filled nanocomposites, (b) DMA tan δ curves of nanocomposites filled with 10 wt.% of differently treated silica fillers, and (c) tan δ peak temperatures for nanocomposites with 10-30 wt.% filler loadings.

The effect of filler loading in nanocomposites with different silica surfaces on composite T_g is shown in Figure 3-8c. It is clear that different filler surfaces result in very different T_g behaviors, and the filler types are ranked PDMS-silica, GPTS-silica, and pristine silica in the order of high to low T_g. PDMS-silica has a positive reinforcing effect on the epoxy composite for all the loading levels examined, with the maximum T_g enhancement of about 17˚C higher than that of neat epoxy at 20 wt.% loading. GPTS-silica also shows a positive effect on T_g enhancement at the initial 10 wt.% loading. However, the T_g enhancement effect is reduced with additional loading, and at 30 wt.% loading, T_g is lower than that of neat epoxy by about 3 ˚C. The T_g trend of pristine silica-composites suggest that the filler has a negative effect on T_g; all but the 10 wt.% loading sample exhibit lower T_g than that of neat epoxy, and the magnitude of T_g reduction increases

monotonically with filler loading. T_g of thermosetting polymer networks can be affected by a number of factors, such as monomer molecular and polymer network structures, crosslinking density, free volume, and filler-matrix interactions. In the present study, the surface of silica nanofillers are modified, and the changes in the observed material properties will be explained in terms of the effect of filler surface chemistry.

It has been reported that the T_g of nanocomposites can exhibit large deviation from that of bulk polymer, and that T_g increases when attractive filler-polymer interactions occur and decreases when poor interface result in free surfaces [66]. Because the filler-matrix interphase thickness is independent of filler size, the impact is particularly important with nanosized fillers due to the large surface area-volume ratio [75]. In our study, the observed trend in T_g can be explained by the reactions of functional groups on the silica surfaces, and the reaction availability of epoxy and anhydride hardener in the resin. The silanol groups on the surface of pristine silica and the amine groups on the PDMS-silica both can act as nucleophiles in the nucleophilic addition reactions with epoxide or anhydride, and in the dehydration reaction with hydroxyl in the opened anhydride rings (Figure 3-9 - Figure 3-14):

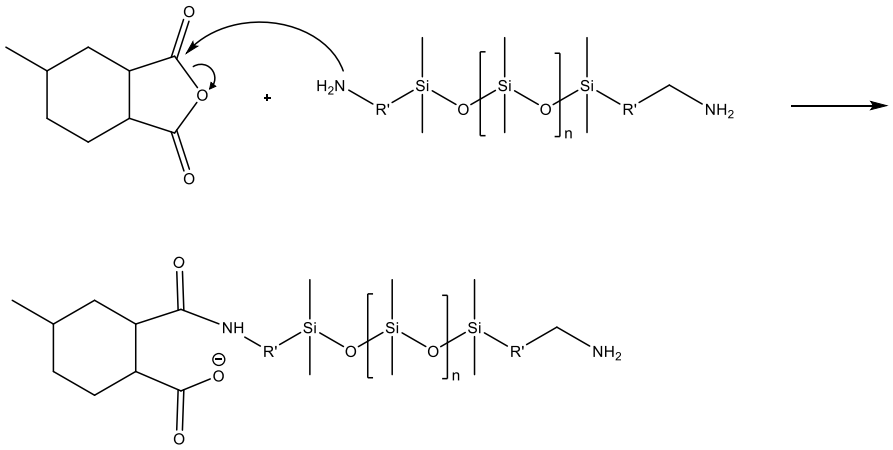

Figure 3-9. Nucleophilic addition reaction of the amine nitrogen with the anhydride ring.

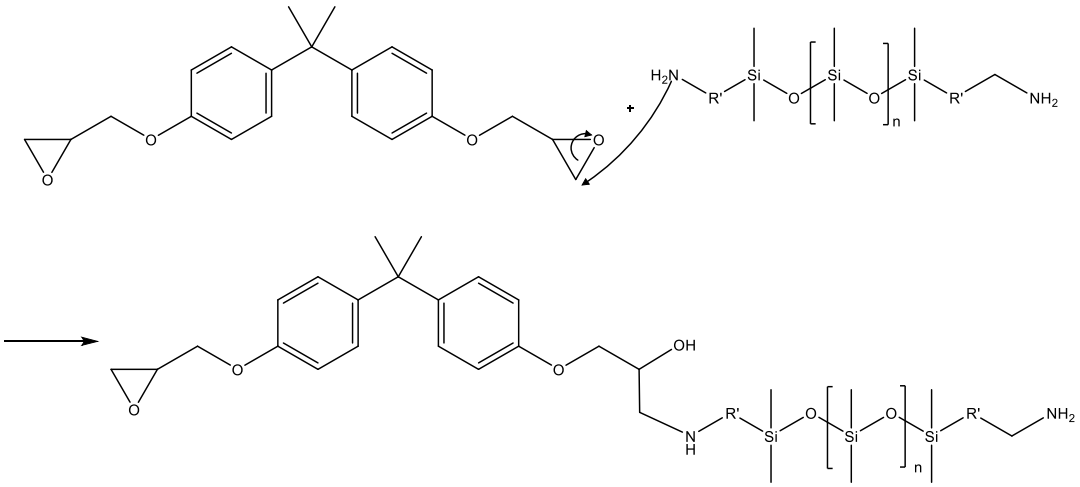

Figure 3-10. Nucleophilic addition reaction of the amine nitrogen with the epoxide ring from bisphenol-A epoxy.

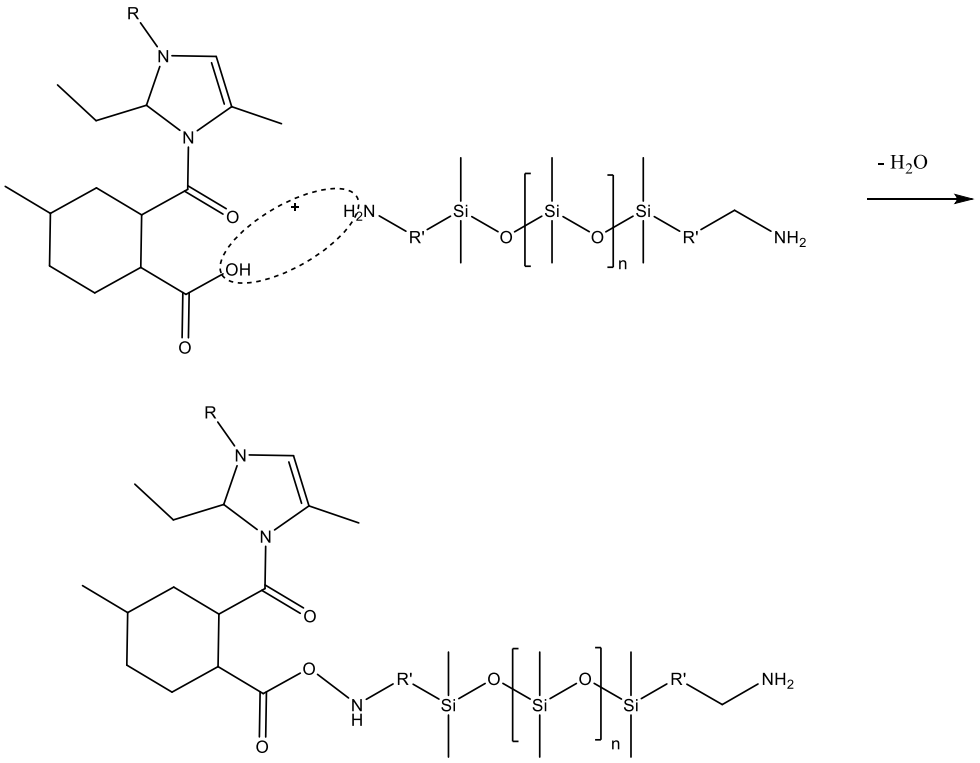

Figure 3-11. Dehydration reaction of amine nitrogen with hydroxyl in the opened anhydride ring.

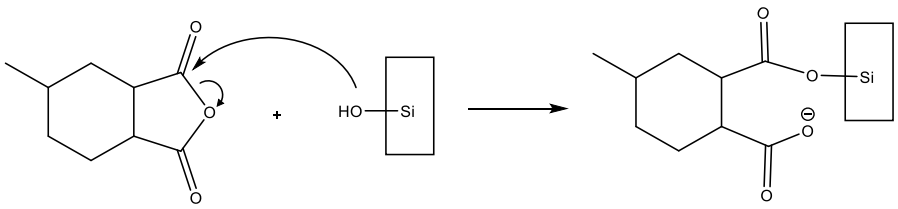

Figure 3-12. Nucleophilic addition reaction of the silanol group with the anhydride ring.

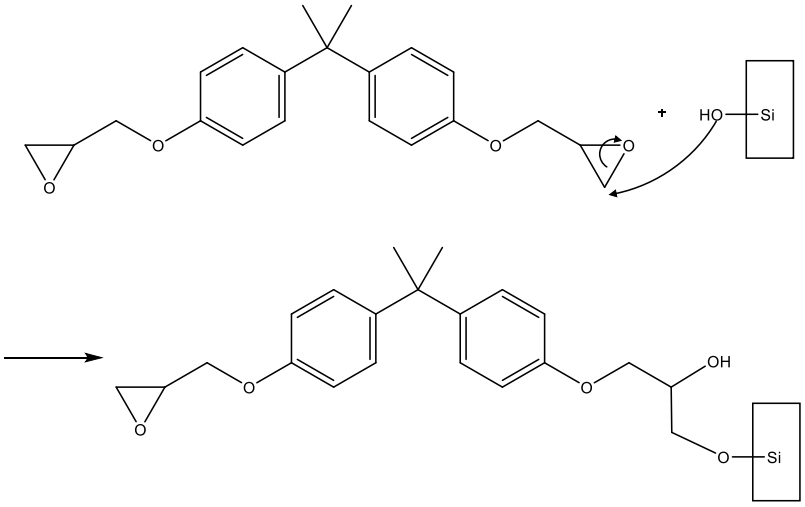

Figure 3-13. Nucleophilic addition reaction of the silanol group with the epoxide ring from bisphenol-A epoxy.

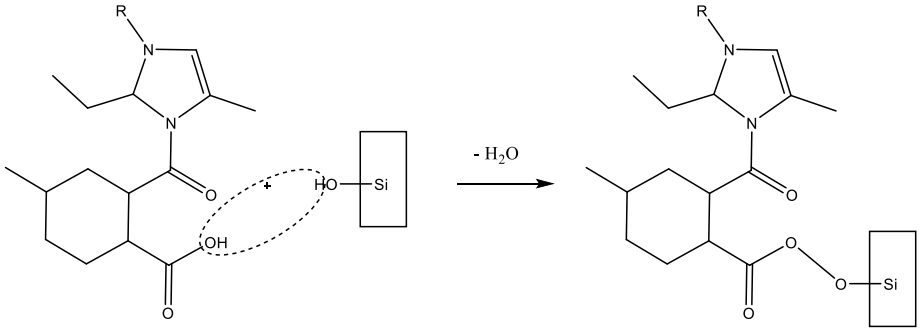

Figure 3-14. Dehydration reaction of silanol with hydroxyl in the opened anhydride ring.

However, the silanol group has weaker nucleophilicity due to the stronger electronegativity of the oxygen atom, and is also more polar and less compatible with the epoxy segments in the resin [114]. Therefore, the bonding interactions of PDMS-silica to the epoxy system is stronger than that of pristine silica. The stronger bonding of silica filler

to the epoxy matrix result in physical immobilization of the polymer chain in local region surrounding the filler particle, resulting in a higher T_g. In the PDMS-silica case, T_g is slightly increased from the 10 to 20 wt.% loading samples, in agreement with the expected improved interphase. In the 30 wt.% sample, it is suspected that the T_g reduction is resulted from the large amount of low-T_g PDMS in the nanocomposite.

The epoxide groups on GPTS-silica can react with the epoxy resin in two ways, with imidazole catalyst or the hydroxyl in the opened anhydride rings, as shown in the reaction schemes below (Figure 3-15 and Figure 3-16):

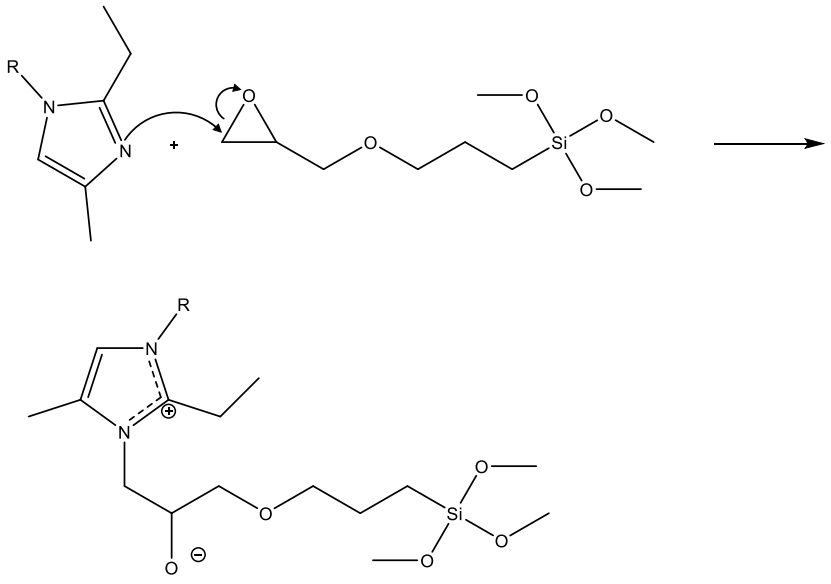

Figure 3-15. Nucleophilic addition reaction of the pyridine nitrogen in imidazole with the epoxide ring in GPTS. For simplicity reasons, the structure of imidazole catalyst is shortened with R = 2-cyanoethyl and GPTS is shown in its unhydrolyzed form and not attached to silica.

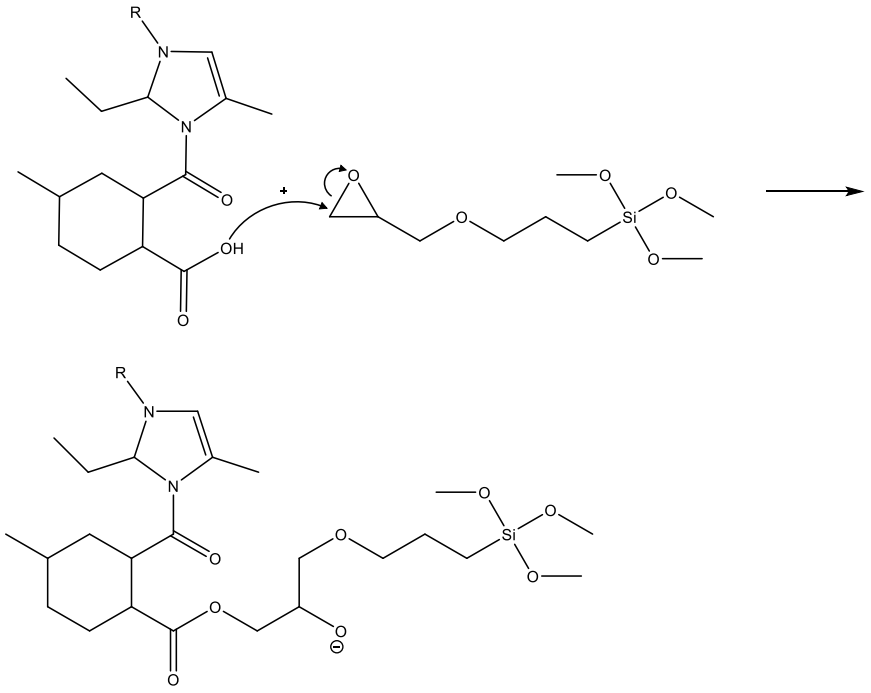

Figure 3-16. Nucleophilic addition reaction of the hydroxyl in opened anhydride ring with the epoxide ring in GPTS. For simplicity reasons, the structure of imidazole catalyst is shortened with R = 2-cyanoethyl and GPTS is shown in its unhydrolyzed form and not attached to silica.

It should be noted that the anhydride hardener is more volatile than the epoxy resin, as evidenced in the TGA curves (Figure 3-17):

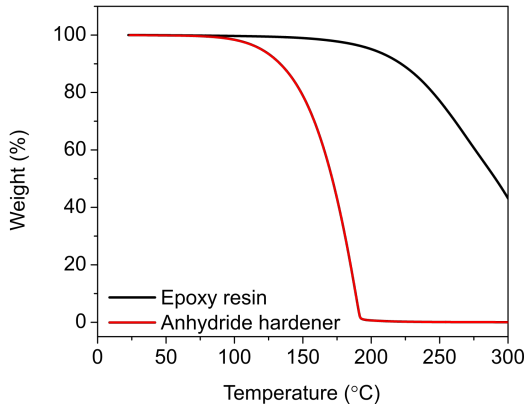

Figure 3-17. Dynamic TGA scans of HMPA and epoxy showing the higher volatility of HMPA.

The epoxy resin system is formulated to contain equimolar amounts of reactive epoxide and anhydride, and the loss of anhydride during curing process would lead to residual unreacted epoxide groups in the system. The epoxide groups on GPTS-silica surfaces contribute to further stoichiometric imbalance in the ratio of reactive epoxide group to anhydride group in the nanocomposite system, contributing to less perfect interphase region and fewer crosslinking sites in the epoxy resin matrix, leading to lower T_g [197].

In addition to weaker reactivity of its silanol groups than amino groups as discussed earlier, pristine silica fillers also contribute to low composite T_g by filler agglomeration (Figure 3-6a and d). When filler particles agglomerate, their interphase regions overlap and result in a reduced interphase volume in the composite, and less polymer chains is immobilized, leading to lower T_g [81]. In both pristine silica and GPTS-silica nanocomposite, the effect of the imperfect silica-polymer interface on the T_g reduction of

nanocomposite becomes more pronounced as filler loading increases because the total volume of the interphase region increases, which is in agreement with the experimental results for pristine silica and GPTS-silica composites.

The effect of filler surface modifications on the bulk properties of the nanocomposites is also examined with thermal expansion behaviors. The coefficient of thermal expansion (CTE) of composite materials not only provides information on the filler-matrix interphase, but is also an important parameter in the application of underfill for electronic package reliability. The CTE of cured epoxy resin below glass transition temperature is 64.9 ppm/K. With addition of low-CTE silica fillers (0.5 ppm/K), CTE of nanocomposite decreases accordingly, and can be modeled by rule of mixture, Turner, and Schapery models, which are detailed below. In the Reuss model, uniform stress in the composite is assume, and a simple rule of mixture can be used [198].

$$\alpha = \phi_m \alpha_m + \phi_f \alpha_f \tag{10}$$

where α is CTE of the composite, α_i and ϕ_i are CTE and volume fraction of phase i, respectively, and subscript i denotes the matrix or the filler phase. In this model, only the CTE of the individual phases are accounted for.

Turner model considers the mechanical interactions between the filler and matrix phases [199]:

$$\alpha = \frac{\phi_m K_m \alpha_m + \phi_f K_f \alpha_f}{\phi_m K_m + \phi_f K_f} \tag{11}$$

where K_i is the bulk modulus of phase *i*. Turner model assumes uniform strain throughout the composite, so the modulus of the individual phases is used in the equation. In this model, the high modulus of silica fillers contributes to reduction of CTE.

In the Schapery model [200], elastic energy principles are taken into account [201], and an upper and a lower bound of CTE are developed using the shear moduli of the phases:

$$\alpha^u = \alpha_m + \frac{K_f}{K^l}\frac{(K_m - K^l)(\alpha_f - \alpha_m)}{K_m - K_f}, \qquad \alpha^l = \alpha_m + \frac{K_f}{K^u}\frac{(K_m - K^u)(\alpha_f - \alpha_m)}{K_m - K_f} \tag{12}$$

where the superscripts *u* and *l* denote the upper and lower bounds, respectively. K^u and K^l are calculated using the Hashin and Shtrikman model [202]:

$$K^u = K_f + \frac{1-\phi}{\frac{1}{K_m - K_f} + \frac{3\phi}{3K_f + 4G_f}}, \qquad K^l = K_f + \frac{\phi}{\frac{1}{K_f - K_m} + \frac{3(1-\phi)}{3K_m + 4G_m}} \tag{13}$$

where G_i is the shear modulus of phase *i.* The values α, *K,* and *G* used for each of the two phases is summarized in Table 3-2.

Table 3-2. Material parameters used in the CTE calculations.

	Epoxy matrix	Silica filler
Density (g/cm^3)	1.225	2.196
α (ppm/K)	64.89	0.55
K (GPa)	2.4	36.7
G (GPa)	0.9	31.2

The modeled results, along with experimental results, are plotted in Figure 3-18:

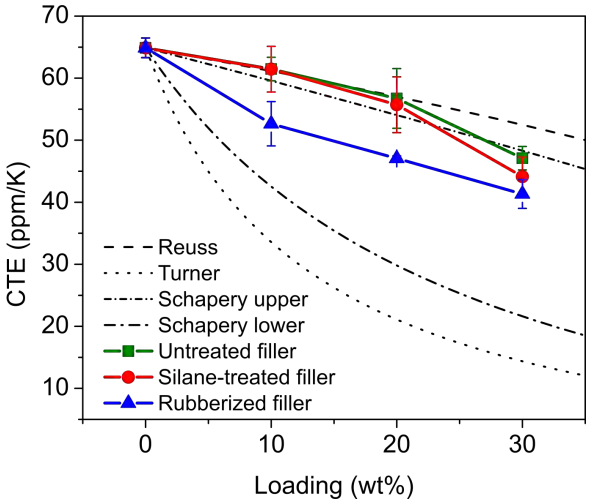

Figure 3-18. Modeled and experimentally measured CTE of silica nanocomposites with filler loading.

It is seen that the nanocomposites incorporating untreated or GPTS-treated silica fillers exhibit only moderate CTE reduction. At lower filler loading (10-20 wt.%), CTE of both

composites lie between the Reuss and Schapery upper bounds, with the GPTS-silica showing a slightly lower CTE. The rule of mixture does not consider interactions between the filer and matrix, and gives the highest CTE estimation of the models presented here. The result suggests that both pristine silica and GPTS-silica have weak interfacial interactions with the epoxy matrix, consistent with the analysis presented earlier. At 30 wt.%, CTE of both composites are reduced by about 10 ppm/K from that at 20 wt.%, and this can be attributed to the effect of reduced interparticle distance and percolation of interphase. In an ideal nanocomposite with cubic distribution and ideal dispersion, the interparticle distance τ can be calculated using the particle diameter d and volumetric filler loading ϕ [76]:

$$\tau = d\left[\left(\frac{\pi}{6\phi}\right)^{1/3} - 1\right] \tag{14}$$

Using the above equation, it is found that the interparticle distance of ideally dispersed nanosilica becomes shorter than particle diameter when filler loading reaches 7 vol.%, corresponding to 14 wt.%. Furthermore, when filler loading is higher than 15 vol.%, or 28 wt.%, the interparticle distance is shorter than the particle radius. At 30 wt.% loading, the interparticle distance is just below the particle radius, suggesting that it is on the order of the effective length of the particle attraction zone, and the nanocomposite in fact becomes a three-dimensional network of silica fillers and their interphase regions. Combined with the high surface to volume ratio derived from nanosized filler, the properties of the interphase region become significant with increased filler loading. Since both the pristine and GPTS-silica have reactive functional groups towards epoxy resin (silanol and epoxide,

respectively) via the reaction routes presented earlier (Figure 3-12 - Figure 3-16), the filler-matrix adhesion can limit the thermal motion of polymer chains using the large interphase region, resulting in much lower CTE at 30 wt.% silica loading.

On the other hand, nanocomposites incorporating PDMS-grafted silica exhibit CTE lower than the Schapery upper limit even at 10 wt.% loading, and the CTE continues to decrease to 41.3 ppm/K at 30 wt.% loading. At 10 and 20 wt.% loadings, the CTE of PDMS-silica filled nanocomposites are 52.6 and 47.1 ppm/K, respectively, and both are lower than those of corresponding silica- and GPTS-silica filled nanocomposites by 8 to 10 ppm/K. Grafted PDMS effectively increases the size of the interphase region, and with the good adhesion to epoxy by the reactive functional groups, nanocomposite CTE is greatly reduced. It should be noted that PDMS is in its rubbery phase at room temperature and its CTE is high, and PDMS grafting can lead to increased CTE. Indeed, at 30 wt.%, the CTE enhancements of incorporating PDMS-silica, as compared to incorporating silica or GPTS-silica, are reduced to 6 and 3 ppm/K, respectively. This can be attributed to 1) lower CTE in silica-filled and GPTS-silica filled nanocomposites due to interconnected interphase region, and 2) higher equivalent PDMS loading, both become more pronounced as filler loading increases.

3.3.3 Nanocomposites: fracture properties

The fractured surfaces of the nanocomposites were examined under SEM to study the effect of filler surface treatments on crack propagation and fracture behaviors of the composites. Representative SEM images of the 30 wt.%-filled composites are shown in

Figure 3-19. It is observed that large agglomerates of pristine silica nanoparticles are present in the epoxy composites. Figure 3-19a shows an agglomerate on the order of several micrometer diameter, which is slightly larger than the average agglomerate size obtained from DLS (Figure 3-6a). As epoxy resin monomers have higher molar mass and fewer polarizable groups per chain than solvent used for DLS studies, it is reasonable that pristine silica find fewer polar interactions with its silanol surface groups and that silica nanoparticles form larger agglomerates in order to minimize filler-matrix interactions. Compared to pristine silica, GPTS-silica and PDMS-silica both are much better dispersed in the epoxy matrix due to enhanced surface interactions. The fractography of the composite containing pristine silica fillers shows smooth and large fracture planes between step structures, which is similar to that observed in neat epoxy (Figure 3-20) and indicates brittle fracture behavior with small energy absorption along the crack path to delay the crack propagation. When GPTS-silica and PDMS-silica are incorporated into the epoxy matrix, the fracture surface becomes significantly rougher, indicating the crack front was distorted by the silica inclusions in the propagation. Additionally, the textured surfaces show a tear morphology, suggesting plastic deformations occurred in the polymer matrix by shear yielding, which absorbed more crack propagation energy. It is also observed that the cracks propagated along the filler-matrix interfaces in the pristine silica case, leaving well-defined and clean spherical voids behind and showing clean particles with little or no resin attached to the surface. Such features can be attributed to weak interfacial interactions between the pristine silica surface and epoxy resin. In the case of GPTS-silica and PDMS-silica, the particles on the fractured surface are largely embedded in the epoxy matrix, and

the voids left from particle debonding show a less defined morphology, suggesting a strong filler-matrix interphase and that crack propagated in the bulk epoxy matrix instead of the interphase.

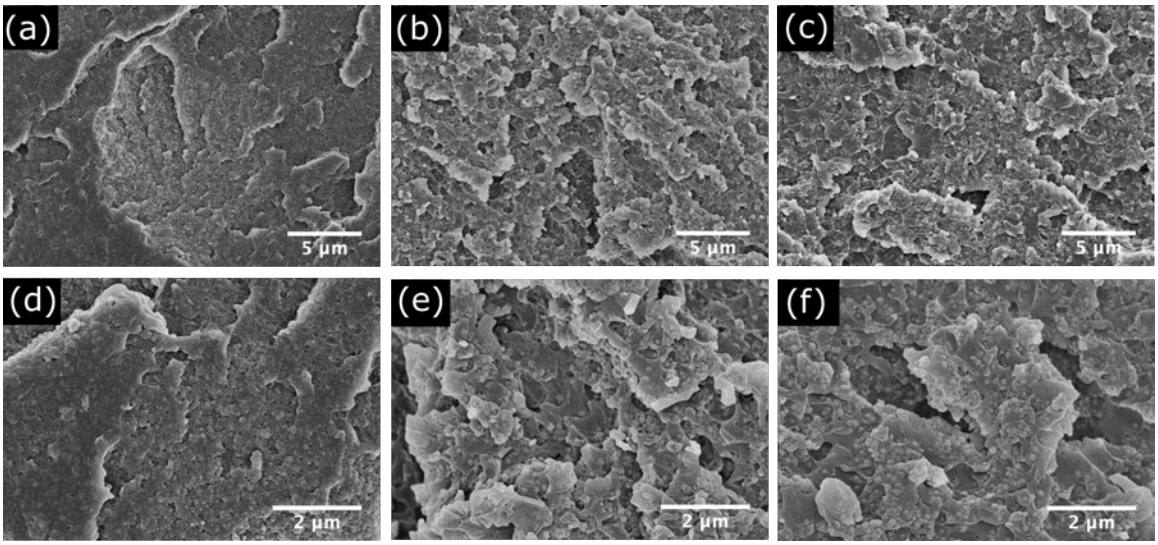

Figure 3-19. SEM images of fracture surfaces of nanocomposites filled with 30 wt.% of (a) pristine silica, (b) GPTS-silica, and (c) PDMS-silica. Higher magnification images of the same nanocomposites are shown in (d), (e), and (f), respectively.

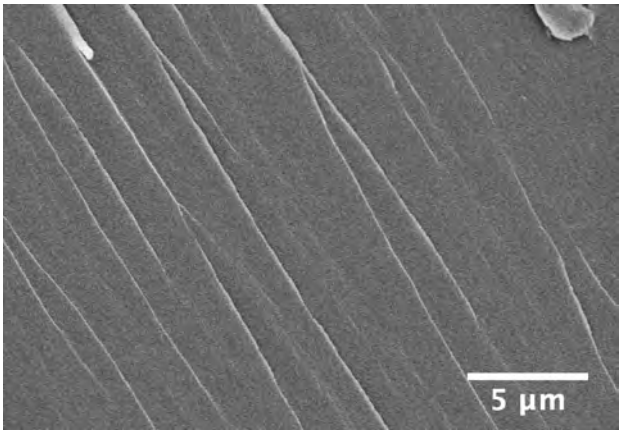

Figure 3-20. Fracture surface of neat epoxy observed under SEM.

It is an established method to measure the fracture toughness of polymer composites using nanoindentation [203]–[205]. A typical loading-unloading curve is shown in Figure 3-21a, where the maximum load (P_{max}), maximum depth (h_{max}), and contact stiffness (S) are used in the calculations for toughness. When the sharp nanoindenter tip is impressed onto a brittle material, radial cracks can be observed. The typical sample surface after nanoindentation test is shown in Figure 3-21b, where the length of impression b and the length of radial crack c are marked. The reduced modulus (E_r), modulus (E), and hardness (H) of nanocomposites are calculated based on the Oliver-Pharr method [206], [207]:

$$H = \frac{P_{max}}{A} \tag{15}$$

$$E_r = \frac{1}{2}\sqrt{\frac{\pi}{A}}S \tag{16}$$

$$\frac{1}{E_r} = \frac{1-\nu^2}{E} + \frac{1-\nu_i^2}{E_i} \tag{17}$$

where E_i (1140 GPa) and Poisson's ratio ν_i (0.07) are the elastic properties of the diamond indenter. The value of Poisson's ratio ν of the polymer materials is commonly is taken as 0.35 [208], which is used here for the nanocomposite. Subsequently, the stress intensity

factor K_c can be calculated using the relationship between fracture toughness of radial crack length [209]. The tip shape factor a is 0.016 for the Berkovich tip:

$$K_c = a\sqrt{\frac{E}{H}}\left(\frac{P_{max}}{c^{3/2}}\right) \tag{18}$$

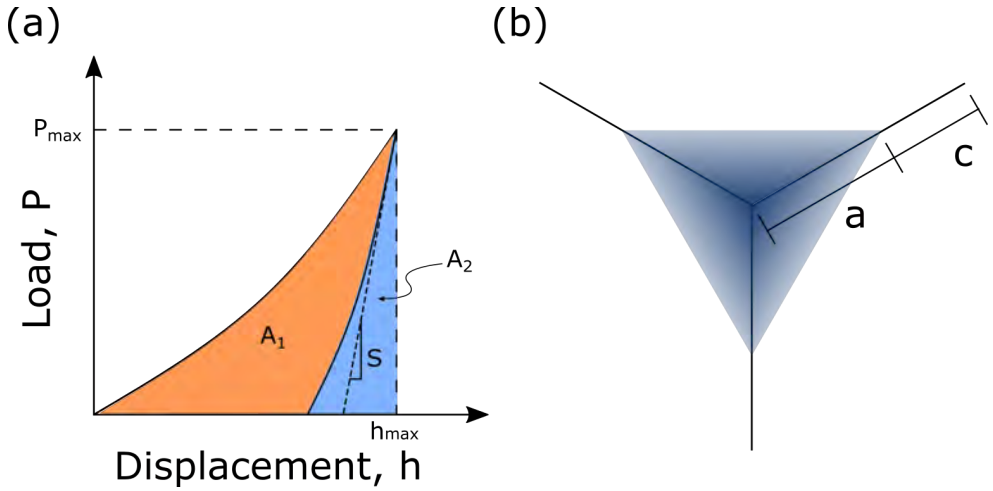

Figure 3-21. (a) The typical load-displacement curve in nanoindentation. (b) Schematic illustration of radial cracking at an indented site.

Neat epoxy and nanocomposite samples were polished and indented to quantify material toughness. However, although material properties were determined, no crack was observed. The impression left by indentation on neat epoxy is shown in Figure 3-22a, and those on nanocomposites containing 10 wt.% of silica with different surfaces are shown in Figure 3-22b-d. All of the indentation impressions showed clear outlines corresponding to the indenter tip, and no cracking could be detected using optical, laser, or atomic force

microscopy. It is believed that, under applied load, polymer chains yield and plastically deform instead of propagating cracks in the material to release the energy. Therefore, a different approach should be employed to analyze the stress-absorbing characteristics of the nanocomposites.

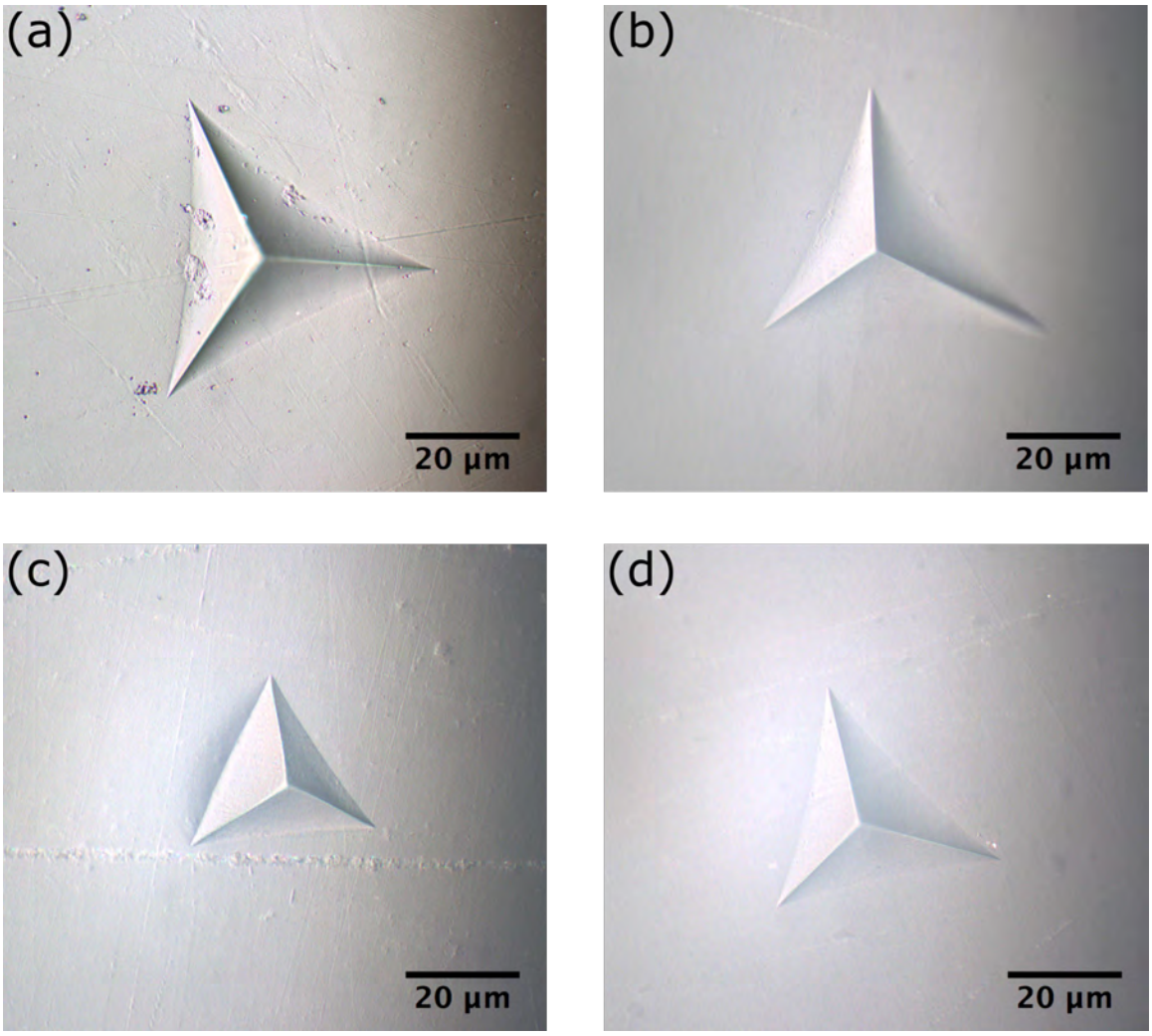

Figure 3-22. Indentation impressions (a) on neat epoxy, nanocomposites with (b) untreated silica, (c) GPTS-silica, and (d) PDMS-silica.

The indentation load – displacement curves of 10 wt.% loaded samples are shown in Figure 3-23. It is clear that the composite with untreated silica fillers was indented to the largest depth under the same applied force of 1 N. The large area under the loading curve (A_1) indicates plastic work done during indentation, and the sample is taken to be more plastic compared to the other samples at the same filler loading [210]. The nanocomposite with GPTS-silica shows steeper loading and unloading curves and much smaller plastic work, whereas the nanocomposite with PDMS-silica shows an indentation behavior between that containing untreated and GPTS-treated silica. The difference in the observed indentation results can be explained by the interfacial interactions between silica and epoxy matrix. As discussed earlier, the functional groups on the silica surface affect the interfacial interactions, which manifest in bulk material properties such as T_g and CTE. Compared to the GPTS- and PDMS-grafted silica, the untreated silica has the poorest interactions with epoxy and is expected to have free volume at the interface. Therefore, it can be reasoned that limited stress can be transferred from the epoxy matrix to silica fillers. Instead, the stress is released by plastic deformation in epoxy matrix. The poor filler dispersion of untreated silica further reduces stress-transfer capability because aggregation reduces the effective surface area of silica in contact with epoxy.

Compared to the nanocomposite incorporating untreated silica, those with GPTS-silica and PDMS-silica show a more visco-elastic character. Compared to untreated silica,

GPTS-silica has a more interacting surface with the epoxy resin indicated by the higher T_g of the nanocomposites. The favorably-interacting interface and covalent bonding across the interface lead to improved stress transfer across the filler-matrix interface. The improved stress transfer efficiency would require a larger force to deform the nanocomposite to the same degree as in the untreated silica case where the stress transfer efficiency is lower. The PDMS-silica case shows an indentation character between the untreated and GPTS-silica cases. It has been demonstrated that the interface between PDMS-silica and epoxy is well-interacting, and the increased plasticity behavior can be attributed to the stress-absorbing property of the rubbery PDMS. In this case, stress is released via the plastic deformation of the PDMS interlayer before it is transferred to the silica.

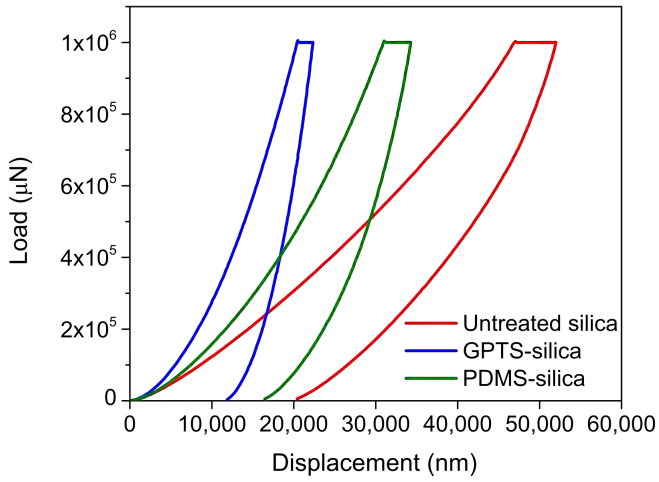

Figure 3-23. Indentation load – displacement curves of 10 wt.%-filled nanocomposite underfills with untreated silica, GPTS-silica, and PDMS-silica.

From the nanoindentation test, the plasticity index ψ can be obtained to characterize the elastic-plastic response of the nanocomposites under external stress and strain. The plasticity index can be calculated from the area under the loading curve, A_1, and the area under the unloading curve, A_2 (Figure 3-21a):

$$\psi = \frac{A_1 - A_2}{A_1} \tag{19}$$

The area under the loading curve is the work done during the indentation, and the area under the unloading curve is the energy released during unloading. The difference between A_1 and A_2 is the irreversible work done during the test. ψ = 0 indicates a fully elastic material, and ψ = 1 indicates a fully plastic material. For viscoelastic polymers, it is expected that $0 < \psi < 1$ [211].

The plasticity indices of neat epoxy and silica – epoxy nanocomposites were calculated from the indentation load – displacement curves and are summarized in Table 3-3 and Figure 3-24. The plasticity index for neat epoxy is 0.652 ± 0.002, and is the highest among the characterized materials because it contains no filler and the applied load mainly results in deformation of polymer chains. At each of the 10, 20, and 30 wt.% filler loadings, the plasticity index decreases in the order of untreated silica, PDMS-silica, and GPTS-silica. This trend agrees with the trend of indentation curves observed in Figure 3-23. The plasticity index decreases with increasing filler loading, and the interfacial interactions between silica and epoxy affects stress transfer and absorbing properties in the nanocomposites.

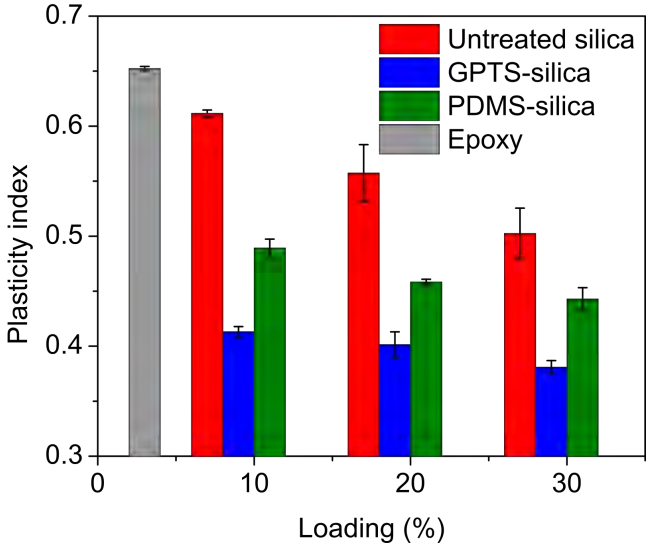

Figure 3-24. Plasticity indices of neat epoxy and nanocomposites containing silica of difference surfaces.

Table 3-3. Plasticity indices of neat epoxy, and nanocomposites with 10-30 wt.% of untreated silica, GPTS-silica, and PDMS-silica.

Loading	Untreated silica	GPTS-silica	PDMS-silica
0	0.652 ± 0.002	0.652 ± 0.002	0.652 ± 0.002
10	0.612 ± 0.003	0.413 ± 0.005	0.489 ± 0.008
20	0.557 ± 0.026	0.401 ± 0.012	0.458 ± 0.002
30	0.502 ± 0.023	0.381 ± 0.006	0.443 ± 0.010

3.4 Conclusion

In this work, we use a two-layer method to modify silica surfaces by chemical grafting of GPTS molecules and PDMS chains. Compared to pristine, untreated silica fillers, the surface modified nanoparticles exhibit improved particle dispersion properties. Because of kinetics of curing and stronger chemical interactions in the filler – matrix interphase region, epoxy-based composites incorporating modified silica fillers show higher T_g, higher modulus, and lower CTE. The effect of interphase properties becomes more pronounced with increasing filer loading due to the larger interphase volume and their percolation. Fractography also shows improved silica – epoxy bonding, and nanoindentation experiments indicate enhanced stress transfer across the filler – matrix interface in modified silica systems. Compared to GPTS – silica system, PDMS – silica shows larger stress absorption by the PDMS interlayer.

CHAPTER 4. SELF-PATTERNING OF UNDERFILL BY TAILORED HYDROPHILIC-SUPERHYDROPHOBIC SURFACES

4.1 Introduction

Manipulation of liquid on surfaces has applications in many areas, such as bioadhesion control [122], microfluidics [212], water collection [125], and nanomaterial positioning [213]. Recent reports have shown successful liquid manipulation using wettability difference between hydrophilic and hydrophobic surface patterns [128], [131], [135], [214], [215]. By preventing the fluid from wetting on the hydrophobic surface and allowing the liquid to wet only on the hydrophilic surface, water can be manipulated in microfluidic channels [137], [139], or split into microdroplets [131], and suspensions of fluorescein molecules and quantum dots can be self-assembled during flow in wetting-controlled surface patterns [128]. Manipulation of high-viscosity or particle-filled fluids such as polymer resins or composites is of great interest to developments in biomedical, electronic, and energy technologies, but demonstrations of polymer fluids or composite manipulation have not been reported.

One potential application of polymer fluid manipulation is the flow control of polymer composite underfill material in IC packages. Underfill is placed under the IC chip to fill the gap between the silicon chip and substrate or between stacked IC chips, and is a critical component to device reliability in electronic packaging by redistributing thermo-

mechanical stress of IC interconnections, providing rigidity, and dissipating heat generated from high-power chips [51], [174], [216]. With the microelectronic trend of packaging miniaturization, current packaging technologies are rapidly progressing towards low profile 3D IC stacking technologies, where memory, logic, microelectromechanical systems (MEMS), and radio frequency (RF) chips can be stacked on top of each other for module miniaturization, higher performance and lower cost [217]. In such an IC stack, underfill is used to fill the gaps between stacked IC chips to ensure their reliability, but the fine pitch and low chip-to-chip heights lead to new challenges in the underfilling process and materials (Figure 4-1) [218], [219].

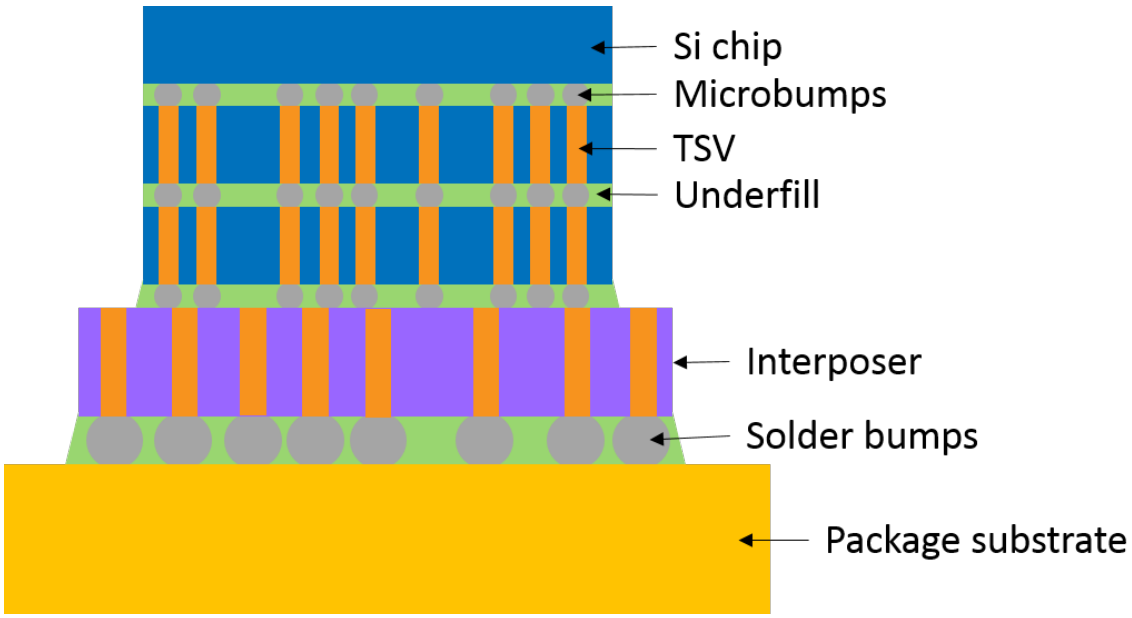

Figure 4-1. Schematic of 3D IC structure. Three device ships are stacked on top of and connected to the interposer by microbumps and through-Si-vias (TSVs). All bumps are encapsulated with underfill for package reliability. Front and back metal layers, and redistribution layer are omitted for simplicity.

Two types of underfilling technologies are generally available– post- and pre-applied processes. In the former, the capillary force draws a liquid underfill into the gap between a chip and a substrate. This process becomes challenging in reduced gap size and high density IC assemblies [220], [221]. In the latter, the liquid underfill is dispensed onto the substrate and then the chip is placed on the substrate and soldered to the bond pads via subsequent reflow process. The pre-applied underfilling process suits the high density and low profile assembly better, but faces the issue of filler trapping at the bond pads [222], impacting interconnection formation and signal transmittance between the chip and the outside (Figure 4-2a). In order to address this filler-trapping problem, attempts to modifying the underfill formulations or IC chip assembly process have been made. However, limited success from those approaches were reported. Employing nanosized filler particles in underfills reduces filler trapping, but the viscosity increases significantly [223], [224]. A double-layer underfilling process uses a high-viscosity and filler-free bottom layer to prevent the filled upper underfill layer from filler entrapment [222]. A two-step process slices through the underfill-covered solder posts before chip assembly [225]. However, the double layer and the two-step process are cumbersome and add to manufacturing cost. Up to now, filler entrapment remains an unsolved issue in pre-applied underfilling process.

Here we demonstrate, for the first time, a self-patterning underfilling technology to eliminate filler trapping by guiding the flow of underfill around bonding pads (Figure 4-2b). By making the bonding pads superhydrophobic and the passivation of the substrate hydrophilic, the underfill dewets from the bonding pads and therefore eliminates the filler

entrapment issue. This technology is facile and applicable to various commercially available underfill materials. However, compared with previous reports on fluid manipulation by wetting-controlled patterns, there are two additional challenges. 1) Previous reports have been limited to low viscosity fluids (< 0.01 Pa·s), whereas underfills have a significantly higher viscosity owing to high loadings of inorganic fillers. Thus, self-patterning of underfills would require a much higher driving force, namely a higher surface energy contrast between patterned substrate surface. 2) In applications in 3D microelectronic packaging, electrical continuity across the bonded Cu interconnects and process compatibility with existing fabrication methods should also be considered. In the current demonstration, we use a symmetric Si-Si structure similar to that in stacked IC packages, where the Si surface is passivated with Si_3N_4, and the top and bottom ICs are interconnected via soldered Cu bonding pads. We carefully fabricate superhydrophobic (SH) Cu bond pads and hydrophilic Si_3N_4 passivation surfaces that can achieve a large water contact angle difference of 119.9° (or epoxy/underfill contact angle difference of 91.6°) between the two substrates. Moreover, this surface modification is shown to be compatible with the bonding process and the commercial underfills on the market.

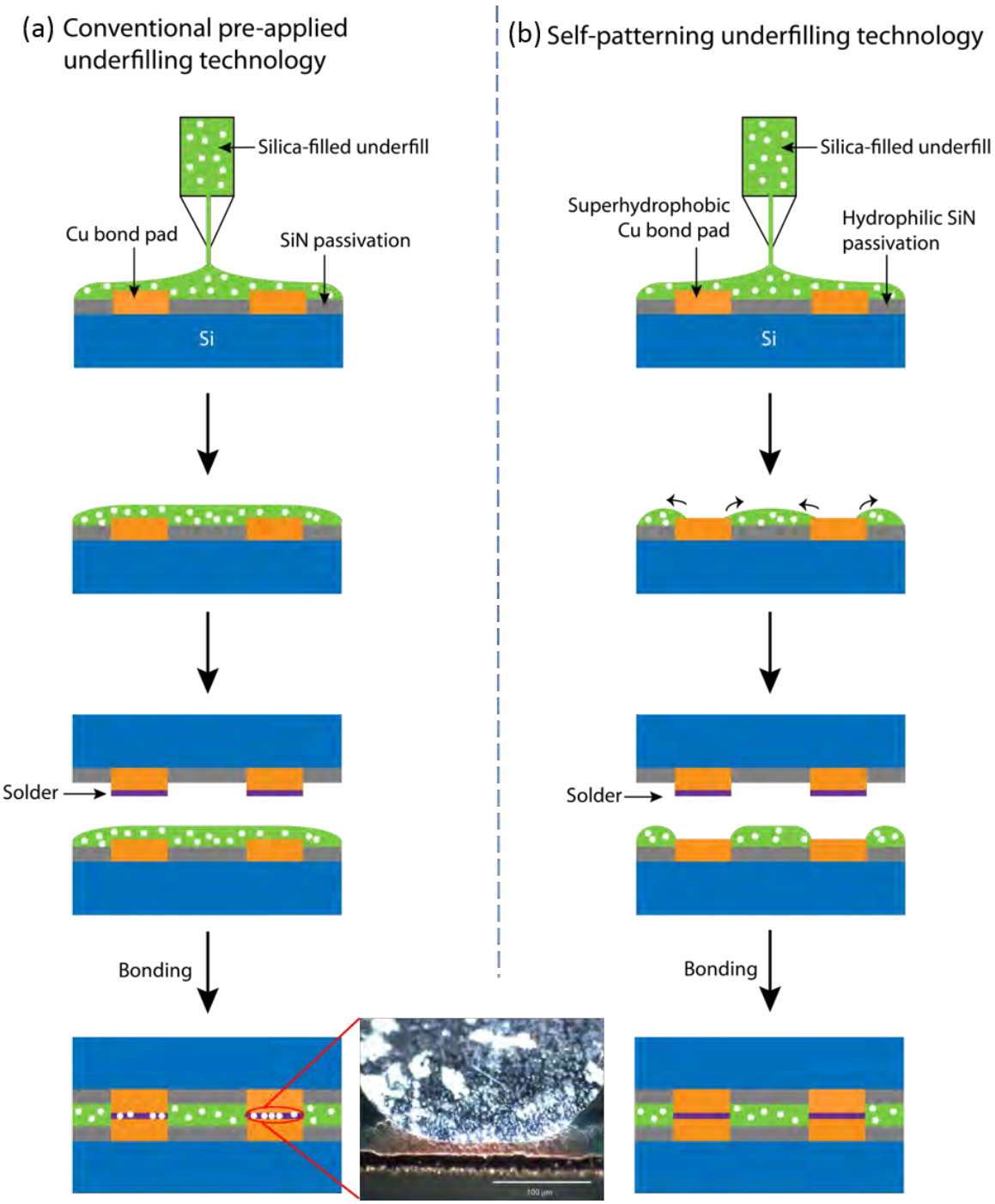

Figure 4-2. (a) Schematic illustration of conventional pre-applied underfilling process, where silica fillers are easily trapped between bond pads (insert), thus impacting the electrical interconnection and reliability. (b) Schematic illustration of the self-patterning

underfilling process, where the silica-filled underfill dewets from the bond pads and cover only the passivation surface.

4.2 Methods

4.2.1 Materials

Deionized (DI) water was produced from a Barnstead Smart 2 Pure Water Purification system (Thermo Scientific). Ammonium hydroxide solution (28%, Alpha Aesar), ethanol (Sigma Aldrich), formic acid (88%, BDH), *1H,1H,2H,2H*-perfluorooctyltrichlorosilane (97%, Sigma Aldrich), hexanes (BDH), and acetone (BDH) were used as received.

For underfill formulation, the epoxy resin was a mixture of diglycidyl ether of bispenol A (Shell Chemicals) and 3,4-epoxy cyclohexylmethyl-3,4-epoxy cyclohexyl carboxylate (Synasia). Hexahydro-4-methyl phthalic anhydride (Lindau Chemicals) and 1-cyanoethyl-2-ethyl-4-methylimidazole were used as curing agent and catalyst, respectively. Silica nanoparticles (100 nm, Nippon Shokubai) and microparticles (1 μm, Alpha Aesar), and γ-glycidoxypropyltrimethoxysilane were used as received.

4.2.2 Simulation model

A 3D fluid dynamics model of a three-region, 50 μm Si_3N_4 − 100 μm Cu − 50 μm Si_3N_4 surface was constructed using OpenFoam Extended 1.6. The width of the surface was 100 μm and the thickness was 1.5 μm. The dimensions of the three-region surface were selected based on the test vehicles used in experiments. Based on the volume of

underfill deposited per unit area in the experiments, a layer of fluid of 10μm thickness, 180μm length, and 100 μm width is placed on the surface as the initial condition. Gravitational force is applied on the system. For simulation of water flow, the density (1.000 g/cm^3), surface tension (72.8 mN/m), and viscosity (0.0009 Pa·s) of water is used. For simulation of underfill flow, experimentally obtained values of underfill density (1.342 g/cm^3), surface tension (46.13 mN/m), and viscosity (1.5 Pa·s) at the underfill dispense condition were used in the simulation. The water and underfill contact angles on the copper surface were varied from 10˚ to 140˚ at 10˚ increments.

4.2.3 Test vehicle fabrication and copper surface treatment

Test vehicles with circular Cu bonds pads of 100 μm diameter, 150 μm pitch and 15 μm height were prepared by electroless and electrolytic plating of Cu using commercially available plating baths. The substrate was CVD grown Si_3N_4 on Si wafer.

In a typical fabrication process, the hydrophilic surface of Si_3N_4 can be obtained by UV-ozone treatment (Novascan UV Ozone Cleaner), and was protected from the superhydrophobic treatment by a standard photolithography process using Microposit SC1827 and Microposit MF319 as photoresist and developer, respectively (Figure 4-3). After the Si_3N_4 protection layer was prepared, the test vehicle was immersed into a 0.03 M ammonia solution for 48 hours to create the surface roughness from $Cu(OH)_2$, and then rinsed with DI water and dried. The test vehicle was then immersed into a 3 mM solution of *1H,1H,2H,2H*-perfluorooctyltrichlorosilane in hexanes for one hour, followed by

subsequent baking at 100°C for one hour. The photoresist protection layer was removed with acetone rinse.

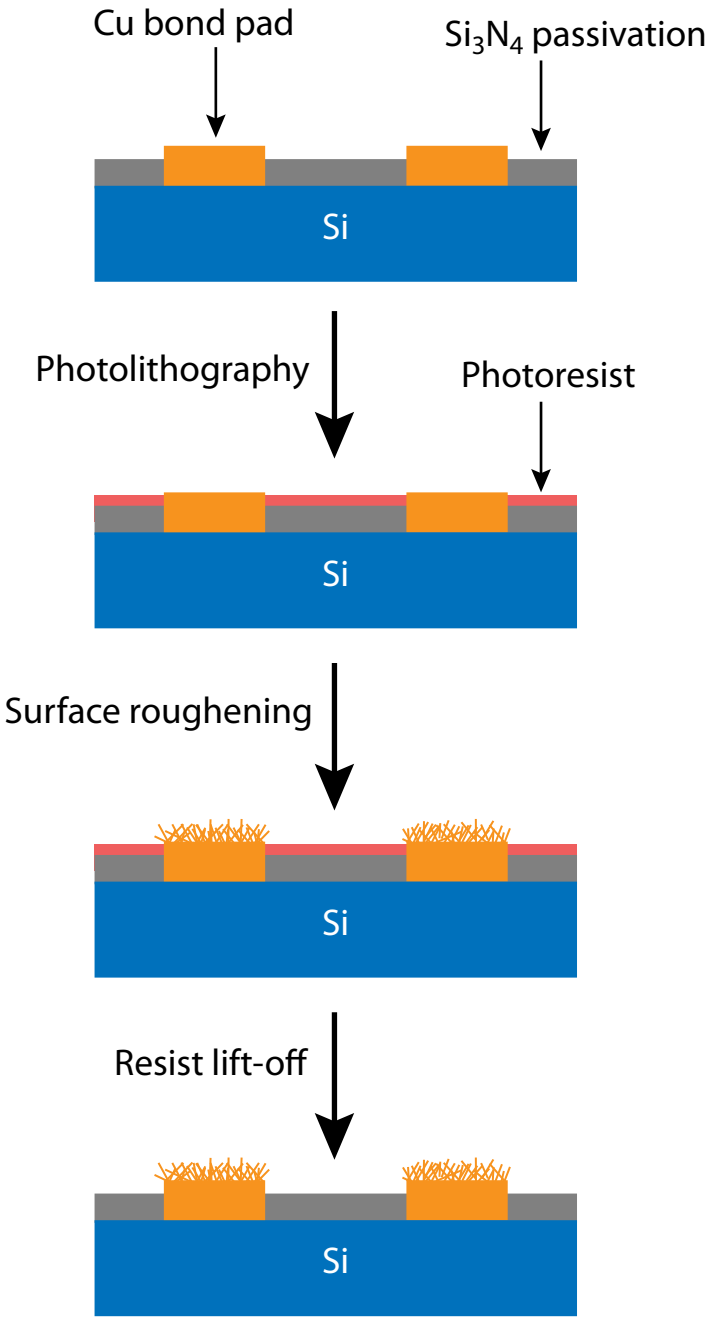

Figure 4-3. Schematic illustration of the superhydrophobic Cu fabrication process.

4.2.4 Underfill formulation and deposition

Silica particles were treated with γ-glycidoxypropyltrimethoxysilane to improve the dispersion of the silica in the underfill. In a typical process, 10 g of silica was dispersed in a water-ethanol mixture by stirring and sonication. Formic acid was added to adjust the pH to 4, and 0.5 g of the silane was added to the reaction mixture. The reaction was refluxed at 100°C for 1 day. The bimodal filler system was mixed at a 25%-75% ratio for the nano- and microparticles, respectively. The surface-modified silica was mixed with epoxy resin by stirring and sonication. Residual solvent from the silica surface treatment was removed by vacuum at elevated temperatures. The curing agent and catalyst were added subsequently and mixed by stirring.

The formulated underfill was deposited on heated test vehicles by spin-coating. A two-step program was used, with step 1) 500 rpm for 10 s, and 2) 3500 rpm for 1 m. The underfill was cured at 150°C for 1 h.

4.2.5 Solder bonding and reflow

For solder bonding tests, eutectic SnAg solder balls (Indium Corp.) were placed on the superhydrophobic Cu bond pads. No-clean flux (NR200, Alpha) was added on the Cu pad and the test assembly was heated on a hot plate to 260°C to allow the solder to melt and form metallic bonding with the Cu pad. For solder paste test, flux-containing, eutectic SnAg paste (Indium Corp.) was placed on the superhydrtophobic Cu bond pad and heated to 260°C on a hot plate. For H_2 flux condition, solder balls were secured on the superhydrophobic Cu bond pad by a clipped microscope cover glass, and the test assembly

was placed in a tube furnace. H_2 gas was allowed to flow for 30 min before heating the furnace to 260°C. The bonded samples were mounted in acrylic, cross-sectioned, polished to smooth surfaces, and finally etched (3 s in a mixture of 2 parts HCl, 5 parts HNO_3, and 93 parts isopropanol) [226] to reveal the intermetallic interface. For XPS characterizations, superhydrophobic Cu bond pads were subjected to the same chemical and temperature conditions, but no solder material was placed on the bond pads.

Reflow test of the superhydrophobic Cu was performed using a reflow oven (Omniflo 5-zone reflow oven) under nitrogen environment. The reflow profile was tested with a remote temperature sensor (Figure 4-4).

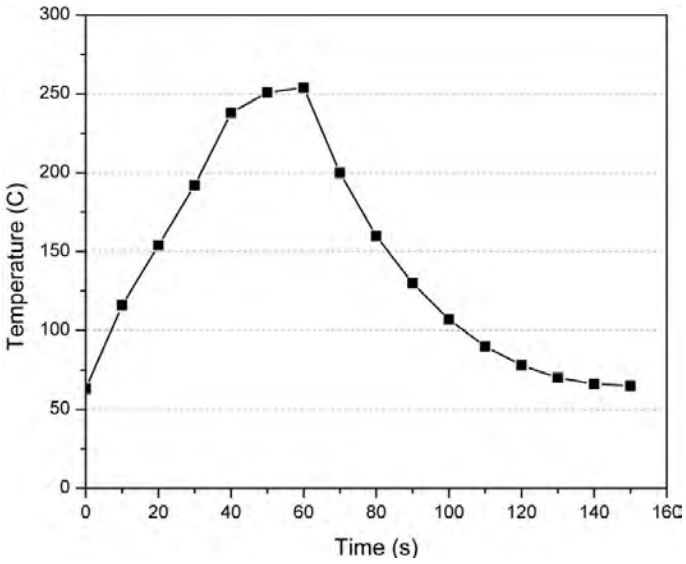

Figure 4-4. Temperature profile of the reflow process.

4.2.6 Characterization

X-ray diffraction (XRD) analyses of the surface-treated Cu pads were performed on a Panalytical Empyrean diffactometer using Cu Kα radiation (45 kV and 40 mA). A contact angle measurement system equipped with a Rame-Hart goniometer and a built-in CCD camera was used to evaluate the contact angles of test vehicle surfaces. The goniometer was also used to determine the surface tensions of underfills by a pendant drop method [227], [228]. Scanning electron microscopy (SEM) images and the corresponding energy dispersive x-ray spectroscopy (EDS) were obtained using a Hitachi SU8010 FE-SEM and a Zeiss Ultra60 FE-SEM using an acceleration voltage of 5-10 kV. X-ray photoelectron spectroscopy (XPS) was used to analyze the chemical states on the sample surfaces using a Thermo K-Alpha XPS. Kinetic curing analysis of underfill was performed on a differential scanning calorimeter (DSC Q2000, TA Instruments), at a ramping rate of 10°C/min.

4.3 Results and discussion

4.3.1 Simulation of fluid flow on patterned surfaces

The driving force for the epoxy to dewet from Cu and flow onto Si_3N_4 can be derived from the Wilhelmy balance method as [229]:

$$F = \gamma_{lv} p \cos(\theta_1 - \theta_2) - f_{friction} - f_{viscosity} > 0 \quad (20)$$

Where γ_{lv} is the liquid surface tension, p is the contact line parameter, and θ_1 and θ_2 are fluid contact angles on Si_3N_4 and Cu, respectively. Computational fluid dynamics simulation was used to estimate the minimum contact angle θ_2 on Cu bonding pads required

to dewet water or underfill. The flow result of a layer of water or underfill was simulated on a Si_3N_4 – Cu – Si_3N_4 surface using the surface tension and viscosity values measured at the dispense condition. Simulation results show that, to achieve self-patterning, the minimum water contact angle on Cu was 90˚, which is close to computational and experimental results reported by Zhao *et al.* [230]. For silica-filled underfill, the minimum contact angle on Cu was 110˚, indicating that a larger driving force is needed for viscous fluid flow (Figure 4-5). Since the measured water and underfill contact angles on Cu are both higher than the calculated minimum value, it is possible to achieve self-patterning by the above superhydrophobic-hydrophilic treatment.

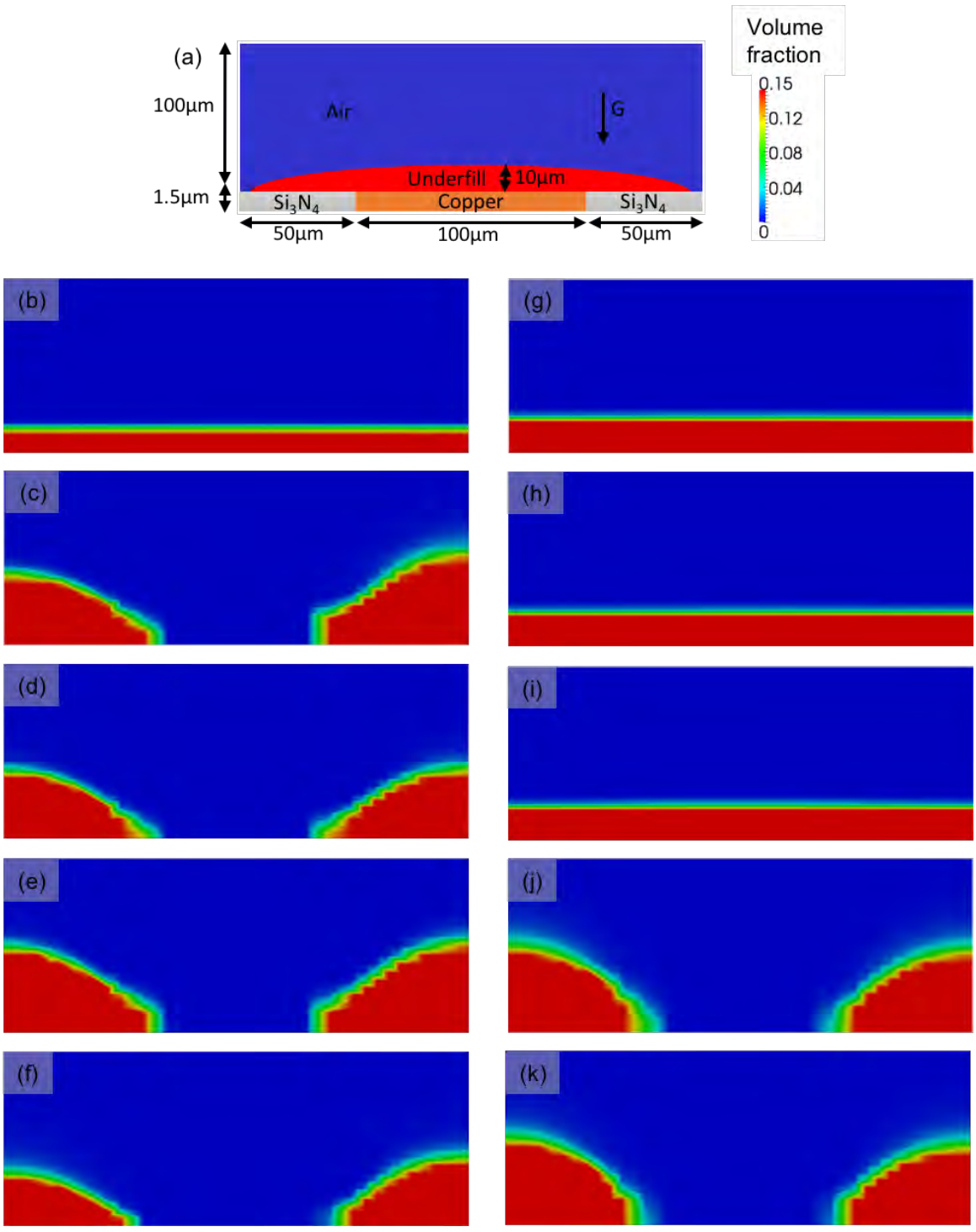

Figure 4-5. (a) Model setup for the numerical simulation. Simulation results show the volume fraction of water on the surface after it was allowed to flow on the surface when the water contact angle on copper is (b) 80˚, (c) 90˚, (d) 100˚, (e) 110˚, and (f) 120˚. The

spatial volume fraction of underfill on the surface is shown when the underfill contact angle on copper is (g) 80˚, (h) 90˚, (i) 100˚, (j) 110˚, and (k) 120˚.

4.3.2 Superhydrophobic copper surface

The hydrophilic surface of Si_3N_4 was obtained by UV-ozone treatment. A photoresist layer (Microposit SC1827) was subsequently coated on the Si_3N_4 surface to protect it during the SH treatment of Cu pads. Finally, the photoresist was removed after the whole treatment (Figure 4-3). The critical step is the SH treatment of Cu pads. The state of superhydrophobicity is defined as having water contact angle greater than 150º and hysteresis smaller than 10º [231]. Established methods to obtain SH surfaces generally include two parts— surface roughening and surface energy reduction. It has been reported that surface roughening of Cu substrates can be achieved by oxidation in aqueous solution of sodium hydroxide and ammonium persulfate [232], [233] or sodium hydroxide and potassium persulfate [123], producing $Cu(OH)_2$ microwires and microflowers. Although high water contact angles were demonstrated, the fabrication method is incompatible with Cu bonding pad fabrication, because the oxidation solution mixture can easily lift off the photoresist used as the Si_3N_4 protection, exposing the Si_3N_4 passivation surface and damage the surface energy contrast between $Si_3N_4$and Cu. Alternatively, spray-coating of fluorinated Cu particles has also been reported as a means to produce robust SH Cu surfaces [234]. Although the spray-coating method circumvents the concern of lifting-off the photoresist, the synthesized Cu particles are tens of microns in size, which is on the same order as the size of bonding pads used in this study. Therefore, the spray-coated Cu would

not be able to create surface roughness required to achieve SH Cu bonding pads. Here we use a mild surface oxidation method via ammonia treatment that does not affect the photoresist used for Si_3N_4 protection, but also creates nano- to micro-sized surface $Cu(OH)_2$ features that can be effective in obtaining SH Cu surfaces on Cu bonding pads. To obtain a low surface energy, the roughened surface is subsequently treated with a highly fluorinated SH molecule *1H,1H,2H,2H*-perfluorooctyltrichlorosilane (PFCS).

The morphology of the ammonia-treated Cu bond pads was characterized using SEM (Figure 4-6a). Surface roughness measurements show that the root mean square height (S_q) increased from 0.108 μm before the roughening procedure to 1.713 μm after 48 hours of treatment. The XRD pattern indicates that the surface species include $Cu(OH)_2$ and CuO, and the Cu substrate is also shown on the diffraction pattern due to the depth of x-ray penetration into the sample (Figure 4-6d). The Cu $2p_{3/2}$ XPS spectrum obtained from the roughened surface shows that the charge of surface Cu is bivalent, and confirms that the surface species is primarily consisted of the $Cu(OH)_2$ (934.8 eV). A small amount of CuO signal at 933.5 eV from the underlying surface is also detected due to surface oxidation (Figure 4-6e) [235], [236]. The formation of $Cu(OH)_2$ on Cu pads also lead to increased electrical resistance from 0.9 ± 0.4 Ω of Cu pad to 200-300 Ω of $Cu(OH)_2$-Cu pads. It is found that the treatment with PFCS does not alter the morphology or crystalline structure of $Cu(OH)_2$ (Figure 4-6b, d). In the C 1s XPS spectrum, the peak at 284.7 eV is assigned to the methyl group on the PFCS molecule. The CF_2 and CF_3 peaks are observed at 291.1 eV and 293.5 eV, respectively, and the ratio of the CF_2 to CF_3 peak areas is 5.4,

which is close to the expected value of 5, indicating the successful grafting of PFCS to the Cu pad surface (Figure 4-6f) [237], [238].

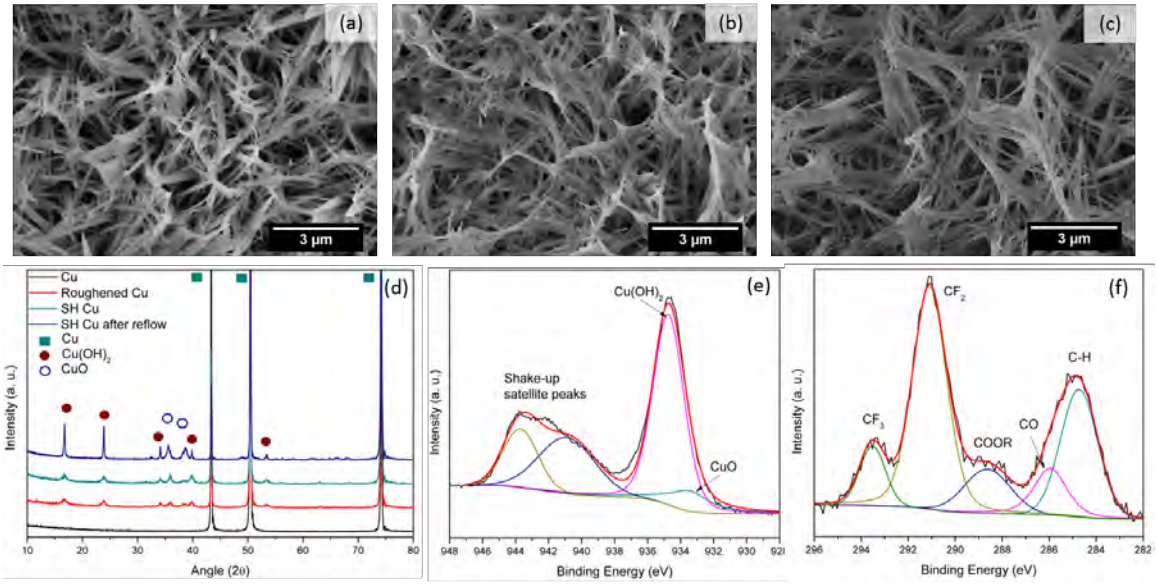

Figure 4-6. SEM images of (a) roughened Cu surfaces after the 48-hr roughening by ammonia solution, (b) SH Cu surface after the PFCS treatment, and (c) SH Cu after the thermal reflow process. (d) XRD patterns of Cu bond pads before treatment (black), after the roughening (red), after roughening and SH treatment (green), and after the typical thermal reflow process (blue). $Cu(OH)_2$ and CuO formed after the roughening treatment and remained after SH treatment and thermal treatment of solder reflow profile. (e) High resolution Cu $2p_{3/2}$ XPS spectrum of Cu bond pads after roughening treatment shows both $Cu(OH)_2$ and CuO. (f) High-resolution C 1s XPS spectrum of Cu bond pads after SH treatment indicates the successful grafting of PFCS on the Cu surface. The CO and COOR peaks are due to atmospheric exposure [237].

Surface wettability of roughened Cu, SH Cu, and Si_3N_4 was examined with droplets of water, epoxy, and underfill material. (Table 4-1). The underfill material used in this

study is a silica/epoxy based nanocomposite with a filler loading of 20 wt.%. The room-temperature surface tension of water, epoxy, and underfill are 72 mN/m, 42-46 mN/m, and 43-45 mN/m, and the room-temperature viscosities are 8.90×10^{-4} Pa·s, 1.8 Pa·s, and 4.5 Pa·s, respectively. The water contact angle on roughened Cu increased from 18.8° to 165.5° after the Cu surface was treated with PFCS. On the same Cu surfaces, the epoxy and underfill contact angle increased from 13.7° to 114.3°. The Si_3N_4 surface exhibits water contact angle of 45.6˚, and the epoxy and underfill contact angle of 22.7°. The differences in contact angles on SH-Cu and Si_3N_4 of water and epoxy/underfill are 119.9° and 91.6°, respectively. These differences can be attributed to the differences in surface energies, which becomes the driving force in the self-patterning and dewetting process of epoxy-based underfills. Moreover, a series of both commercial and in-house prepared underfills show similar surface tension values, rendering a wide applicability of the current method to various underfills on the market (Table 4-2).

Table 4-1. Water and epoxy/underfill contact angles after different surface treatment.

	Roughened Cu	**Superhydrophobic Cu**	**Si_3N_4 passivation layer**	**Difference between bonding pad and substrate**
Water	18.8 ± 2.2	165.5 ± 4.6	45.6 ± 6.2	119.9
Epoxy and underfill	13.7 ± 1.4	114.3 ± 12.0	22.7 ± 2.7	91.6

Table 4-2. Surface tension values of commercial and in-house prepared underfill materials. Formulations of commercial underfills are unknown. In-house prepared underfills were formulated with cycloaliphatic and bisphenol-A type epoxies and anhydride-based hardener. Underfill A contains added coupling agent and silica fillers, and underfill B contains alumina fillers.

Underfill	**Test temperature (°C)**	**Surface tension (mN/m)**	**Reference**
Epoxy resin	25	46.16	This work
A	25	43.59	This work
B	25	44.61	This work
Hitachi CEL-C-3720	25	44.62	This work
C	80	35.4	[239]
D	80	49.4	[239]
E	26	40.7	[240]
F	31	36.4	[240]
G	30	36.4	[240]
H	25	37.3	[240]
I	21	38.3	[240]
J	30	40.3	[241]
K	25	39.1	[242]
L	25	39.3	[242]
M	25	39.1	[242]
N	25	40.1	[242]

Table 4-2 continued.

O	**25**	**35.7**	**[242]**
P	25	37.8	[242]
Q	25	38.5	[242]
R	23	51	[243]
S	23	44	[243]

4.3.3 Self-patterning demonstration

The results of the simulations were confirmed with experimental demonstrations of self-patterned underfill on test vehicles consisted of circular 100μm-diameter Cu pads on Si_3N_4-passivated Si wafer. Due to the small Reynolds number (<< 1) of epoxy underfills [244], they were spin-coated onto the TVs at elevated temperatures. The underfill materials used in this study is a silica/epoxy based nanocomposite with minimum viscosity in the range of 0.1 – 1.5 Pa·s at the dispense temperature. The effect of SH surface treatment on reducing filler entrapment on the Cu bond pads is shown in Figure 4-7. Large amounts of silica fillers were trapped on top of the untreated, as-plated Cu bond pads (Figure 4-7a), whereas the SH-treated Cu bond pad was fully exposed without silica fillers under the same underfilling conditions (Figure 4-7b). Furthermore, underfill self-patterning was successfully demonstrated over a large area. As shown in Figure 4-7c, the silica-containing underfill only wetted the Si_3N_4 passivation surfaces surrounding the circular Cu bond pads. Although a high-magnification SEM image (Figure 4-7d) shows that ~ 4 μm peripheral

region of the Cu pad had some trapped fillers, that region was minimal on a bond pad of 100 μm diameter and does not interfere with the bonding of Cu pad and solder. Aside from the peripheral, the bond pad inside was completely free of silica fillers, and a high-quality bonding can be achieved. The EDS analysis further confirmed that the Cu bond pads were free of silica fillers; the Si signal, which could be attributed to the silica fillers, was only present in the Si_3N_4 area (Figure 4-7e), and Cu mapping shows exposed Cu pads available for interconnect bonding (Figure 4-7f). The experimental demonstration closely matched the simulation results, and to the best of our knowledge, this is the first demonstration of fluid manipulation of polymer composites by combined hydrophobic/hydrophilic surface patterns.

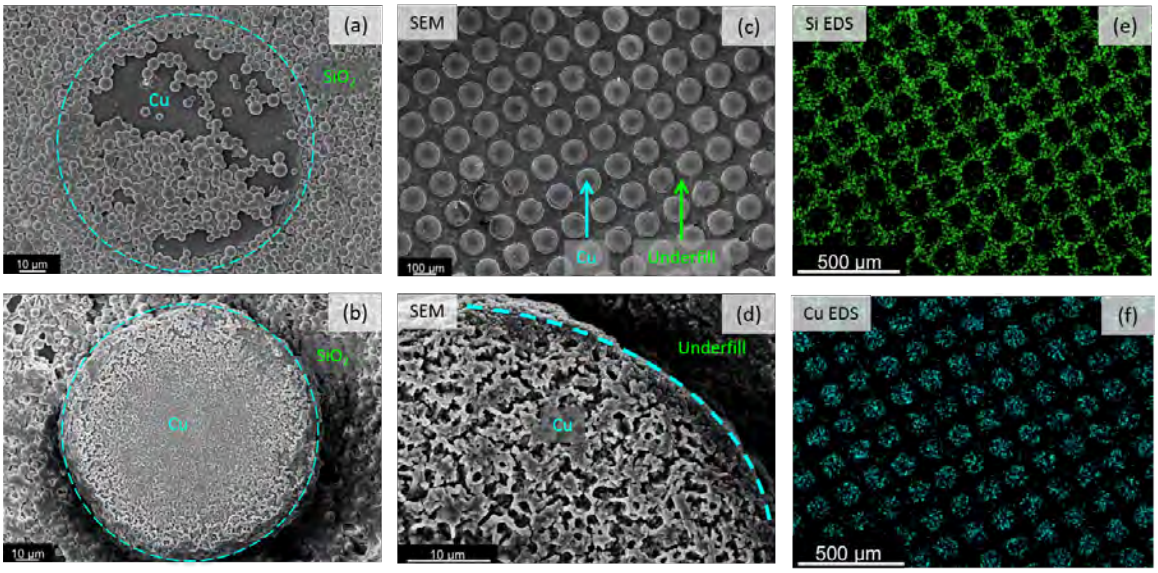

Figure 4-7. SEM images of (a) an untreated Cu bond pad (aqua outline) after underfilling, where silica fillers are easily trapped on the bond pad, and (b) SH Cu bond pad (aqua outline) after underfilling, where the bond pad is fully exposed. The same underfilling conditions were used. (c) SEM image showing self-patterning of underfill on a large area, where the underfill only wets the hydrophilic substrate and dewets from all Cu bond pads. (d) High resolution SEM shows that silica filler only gather around the perimeter of the Cu bond pad without getting on the surface of the bond pad. (e) Si and (f) Cu EDS maps indicate that silica fillers cover the Si_3N_4 passivation, and Cu pad surfaces are fully exposed after underfilling.

Furthermore, self-patterning of underfill on hydrophobic – hydrophilic surface patterns were tested in interconnects. We first used a Cu pillar – Cu bond pad structure. The structure would allow us to observe the effect of having both the top and bottom Cu surfaces treated SH on reducing filler entrapment. A commercial underfill with 50-65 wt.% filler content was used here. Because solder was not used in this case, and with the high melting point of metallic Cu (> 1000˚C), metallurgical bonding was not expected for the <

250˚C thermocompression bonding. When the Cu surfaces were not treated to be SH, a thick layer of trapped silica fillers from pre-applied underfill is observed between the Cu pillar and the bond pad (Figure 4-8a-b). In the case of SH Cu pillar and SH Cu bond pad, the number of trapped fillers is reduced (Figure 4-8c-d). In solder-bonded interconnects, where the Cu pillar is solder-capped, similar observations can be made (Figure 4-9). Significant filler entrapment is observed in the interconnect with non-treated Cu bond pad, whereas the interconnect employing SH Cu bond pad shows reduced filler entrapment and metallurgical bonding between Cu pad and eutectic SnAg solder.

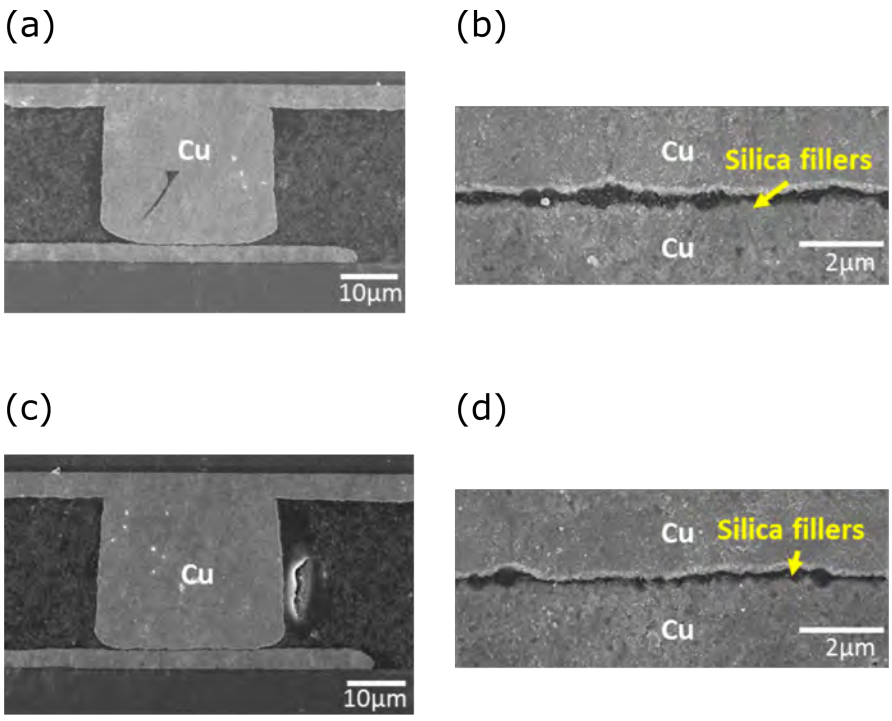

Figure 4-8. SEM cross-sectional images of Cu pillar on Cu bonding pad after thermocompression bonding for (a) non-treated Cu surfaces (b) at higher magnification, and (c) SH Cu surfaces (d) at higher magnification.

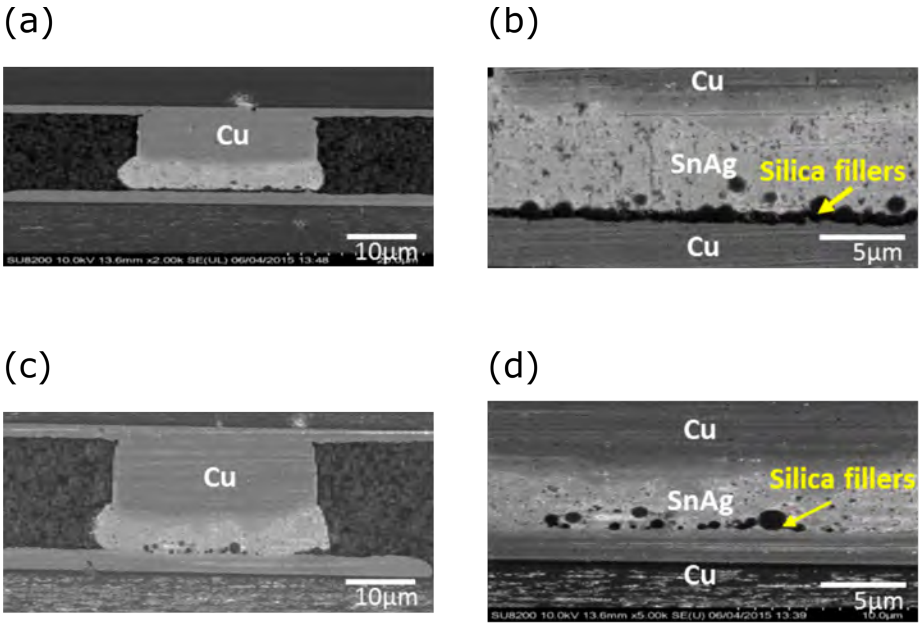

Figure 4-9. SEM cross-sectional images of Cu pillar capped with eutectic SnAg solder on Cu bonding pad after thermocompression bonding for (a) non-treated Cu bond pad (b) at higher magnification, and (c) SH Cu bond pad (d) at higher magnification.

4.3.4 Compatibility with interconnection bonding process

In addition to showing the feasibility of self-patterning underfill, the compatibility of the self-patterning surface treatment with the current interconnection bonding process is demonstrated. This includes two aspects: 1) the surface treatment does not affect the bonding of solder to SH Cu, and 2) the surface treatment does not affect the underfill curing.

Commercially available, eutectic SnAg solder was used to bond to the surface-treated SH Cu bond pads. Without an added flux, the SH $Cu(OH)_2$ structures on the surface remain after the typical solder reflow process (Figure 4-4), as demonstrated by the

unchanged morphology (Figure 4-6c), XRD pattern (Figure 4-6d) and XPS results (Figure 4-6d). The enhanced CuO peaks in the XRD pattern are due to the thermal decomposition of $Cu(OH)_2$ into CuO at elevated temperature. However, when a conventional flux is added, the $Cu(OH)_2$ can be converted to CuO during flux activation stage [245], and subsequently reduced to Cu by solder flux for solder bonding. Three commonly used types of solder-flux combinations were tested respectively: 1) solder ball with no-clean flux, 2) solder pastes with built-in flux, and 3) solder ball and hydrogen gas, which is the major component in conventional reductive forming gases. In all three cases, the solders wetted the pads to form metallurgical bonding with Cu. In cross-sectional SEM images, the typical scallop-like intermetallic compound (Sn_6Cu_5) is clearly observed at the solder − Cu interface (Figure 4-10a-c). Cu $2p_{3/2}$ XPS spectra show that the fluxing species reduced the surface species to metallic Cu, at 932.62 eV (Figure 4-10e-f) [246]. In addition, the resistance across the bonding sites was measured after soldering. It was shown above that the surface roughening treatment increases the resistance of Cu pad from 0.9 ± 0.4 Ω to 200-300 Ω. After fluxing, the electrical resistance of bonded solder-Cu was reduced to 2 ± 0.9 Ω, indicating that with the flux, the SH treatment of Cu pads for underfill patterning will not affect the interconnection bonding.

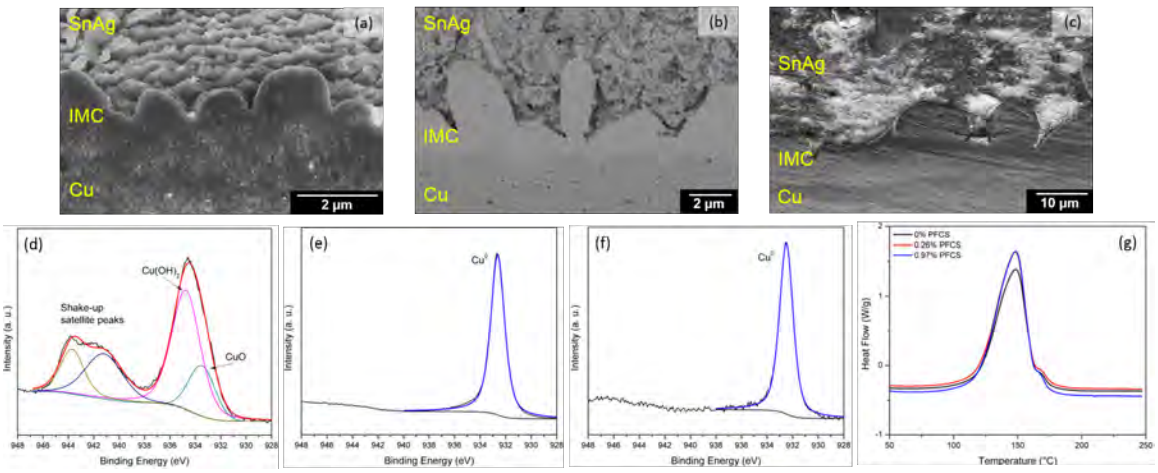

Figure 4-10. SEM image of the SnAg solder and Cu pad interface after reflow, and the formation of the intermetallic compound shows good metallurgical bonding under (a) solder ball with no-clean flux, (b) solder paste with built-in flux, and (c) solder ball with hydrogen gas environment. The soldering material was preferentially etched by an acid-isopropanol solution to better show the intermetallic compounds in the image. High resolution Cu $2p_{3/2}$ XPS spectra of SH Cu after (d) thermal reflow process without chemical fluxing agents, (e) reflow with no-clean flux, and (f) reflow under hydrogen gas. (g) Curing behaviors of underfill measured by dynamic DSC method. The shoulder at 168°C is due to the reactivity difference between two epoxy base resins.

The effect of the SH chemical modifications on the underfill material was studied with differential scanning calorimetry (DSC) (Figure 4-10g). Up to ~1 wt.% of PFCS was added to epoxy-based underfills to simulate the diffusion of the molecules into the underfill in bonded packages, and the DSC results showed negligible changes in the curing behavior. For samples consisting 0% to 1% PFCS, the heats of curing lie within 330 J/g to 340 J/g, and the curing reactions all peaked at around 148.5°C. Because the 0.97 wt.% addition of PFCS was in large excess compared to the concentration of PFCS on the Cu pad surface,

it can be reasoned that the diffusion of the SH molecules into the underfill in packages would have negligible effects on the curing behavior of the underfill.

4.4 Conclusion

In this work, we report a novel underfilling method to eliminate filler entrapment of pre-applied underfill in low profile and fine pitch IC packaging. In this method, underfill self-patterning was achieved by fabricating superhydrophobic Cu bond pads and hydrophilic passivation layer. It is shown that such surface modifications do not interfere the interconnection bonding and the curing behavior of underfills. Compared to conventional underfilling processes, this technology can reduce filler trapping at the bond pads, thus improving the reliability of interconnects in high density 3D IC packaging.

CHAPTER 5. FUTURE WORK

Based on the studies presented in this thesis, the following is recommended for future study:

1. Investigation of degradation of LED encapsulant under lighted condition. The study of encapsulant reliability presented in this thesis suggested minimal material degradation under high-humidity thermocycling conditions. The test was performed using encapsulant coatings instead of LED packages. Testing with actual LED packages will allow us to study the environmental effects on encapsulant discoloration, adhesion strength and delamination, and light output over time.
2. Investigation of mixing rubberized filler and silane-treated filler for underfill with low-CTE and enhanced stress absorbing capability. As discussed in Chapter 3, the CTE reduction in underfills with PDMS-silica slows down when filler loading approaches 30 wt.% due to the increased volume fraction of the rubbery phase. The addition of silane-treated filler is expected to further reduce the underfill CTE. This study can also give insight on the interactions between fillers of reactive surfaces and their effects on composite properties.
3. Investigation of superoleophobic Cu surface for elimination of filler entrapment in fine pitch packages. In Chapter 4, reduction of filler entrapment was demonstrated with superhydrophobic Cu bond pads. However, filler entrapment was not entirely eliminated, suggesting that the driving force for self-patterning was not enough. In fine-pitch package designs, the remaining fillers would lead to more significant

reliability issues. Further reduction in the surface energy of Cu bond pad can render it superoleophobic and increase the driving force for self-patterning of underfill.

4. Modification of epoxy resin with cyanate ester for high-temperature operation. More details and preliminary results are presented in the following section.

5.1 Modification of epoxy resin with cyanate ester for high-temperature operation

5.1.1 Background

The temperature under the hood in automotive can reach 175-250˚C, and high-power modules can lead to localized hot spot over 250˚C [247]. As the result, the electronic industry has seen an increasing demand for organic packaging materials that meet the property requirements for long cycling operations in such high-temperature environments. Epoxy-based molding compound (EMC) has usually been the outermost encapsulation in electronic packages to protect the electronic system from short circuiting, dust, and moisture over a few decades. EMCs generally consist of ~90% silica filler, ~10% polymer resin, and additives including toughening agent, mold releasing agent, flame retardant, adhesion promoter, and coloring agent.For automotive electronics, the molding material should offer high-temperature stability, high reliability beyond Automotive Electronics Council grade 0 thermal cycling conditions (-40˚C to 150˚C), high toughness, good adhesion to neighboring surfaces, high electrical resistivity, low processing viscosity, fast-cure behavior, and flame retardancy.

Currently, EMCs generally fail under high-temperature storage tests beyond 175˚C. Commercially-available molding materials are not compatible for long-term operation

under high-temperature in automotive electronics, and more advanced material is needed to meet the above-mentioned material requirements. In a high-temperature aging environment, chain scission occurs in polymers, producing oxygen radicals that subsequently lead to chain bridging, and finally the moduli of the molding compound increase. Additional failure modes induced by high-temperature environment include delamination, dimensional instability, moisture absorption, cracking, mass loss, loss of toughness, and creep, which refers to thermal-induced polymer chain reorientation. Traditional strategies to improve the thermal stability of EMCs include enhancing crosslinking and interlocking of polymer chains, and increasing aromaticity in the polymer structure. EMC composites containing multi-aromatic epoxy resins and curing agents show increased T_g. However, it is still challenging for epoxy-based molding compounds to survive above 200˚C for more than 1,000 hours.

One measure of the heat resistance ability of a resin is its glass transition temperature (T_g), which is determined by the network structure as well as the crosslinking density of the thermosetting polymer resin [248]. High T_g is beneficial in terms of thermal-mechanical stress and operation temperature range. During thermal cycling and thermal shock, the mechanical stress experienced by the package is a product of modulus, CTE, and temperature change. The CTE above T_g (α_2) is much larger than that below T_g (α_1), resulting in a much larger thermal stress with the same temperature and modulus changes. Also, T_g shows the temperature at which polymer chains begin to slide past each other and material properties change. Although thermal degradation of polymers may not start at T_g,

the material property changes associated with T_g often lead to compromised package reliability, and it is preferred to keep the operation temperature below T_g.

Conventional epoxy molding compounds have T_g around 150-180°C, which has been reported to be insufficient for high-temperature operation of under-the-hood electronics. While efforts have been made to improve the performance of epoxy resin in various aspects including its toughness, thermal conductivity and flame-retardant property [249]–[251], high-temperature reliable epoxy resin still remains a challenge to make.

Cyanate ester resin is known of its good heat resistance ability due to the formation of *s*-triazine rings during the curing procedure [252], [253]. For example, polymers of bisphenol E cyanate ester is reported to have T_g above 250°C [254], whereas conventional EMCs have T_g around 150-180°C. Compared with other high-temperature stable polymers such as polyimide and bismaleimide, cyanate ester has several advantages such as stronger adhesion, lower moisture uptake, and better processability. Compared to epoxy resin, cyanate ester resins also offer many advantages, especially under high temperature conditions (Table 5-1): better adhesion, lower moisture absorption, better resistance against thermo-oxidative degradation, mechanical properties, and less outgassing. In addition, the addition curing reaction of cyanate ester produces no volatile during cure, and cyanate ester resin can be similarly processed as epoxy resins using the conventional molding process [255].

Table 5-1. Comparison of epoxy, cyanate ester, and combined resins for properties important to molding compounds. Color symbols: green = good, yellow = fair, red = poor.

	Epoxy	Cyanate ester	CE + epoxy
HT adhesion			
T_g			
Moisture absorption			
Thermo-oxidative stability			
HT mechanical properties			
HT outgassing			
RT toughness			
Dielectric loss			
Viscosity and processability			
Volatiles during cure			
Cost			

We propose to use cyanate ester-epoxy co-polymer network, in which the triazine cores in epoxy resin synthesized from cyanate ester play a critical role in increasing T_g and enhancing the thermal stability of the molding compound. The triazine group is produced in the trimerization reaction of cyanate ester monomers (Figure 5-1), and cyanate ester can also react with epoxide to give oxazoline the copolymer structure (Figure 5-2).

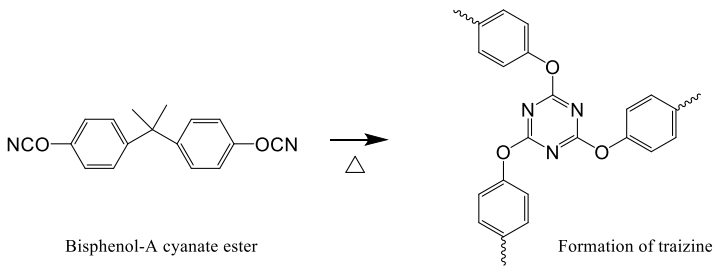

Bisphenol-A cyanate ester Formation of traizine

Figure 5-1. Trimerization of bisphenol A cyanate ester monomers to yield *s*-triazine core.

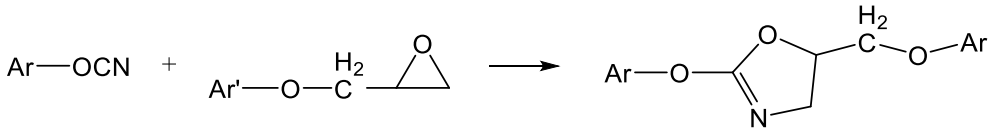

Figure 5-2. Reaction of cyanate ester functional group with epoxide to form cyanate ester-epoxy copolymer via oxazoline bonding.

5.1.2 Cyanate ester resins

Cyanate ester resin was selected as the high-temperature stable polymeric additive to epoxy. Due to the *in-situ* formation of triazine moieties during the thermal curing process, cyanate ester resins have good thermal stability and commonly have T_g of 250-300˚C. Neat cyanate ester monomers of bisphenol A and bisphenol E structure were cured and their T_g were measured using DSC. The DSC Tg of bisphenol A cyanate ester at 289˚C is 45˚C higher than that of the bisphenol E counterpart (244˚C) (Figure 5-3). The higher T_g of bisphenol A cyanate ester is expected due to additional steric hindrance from the additional methyl group on the carbon bridge as compared to bisphenol E cyanate ester. It should be noted that both cyanate ester resins exhibit much higher T_g than typical epoxy resins (150-180˚C).

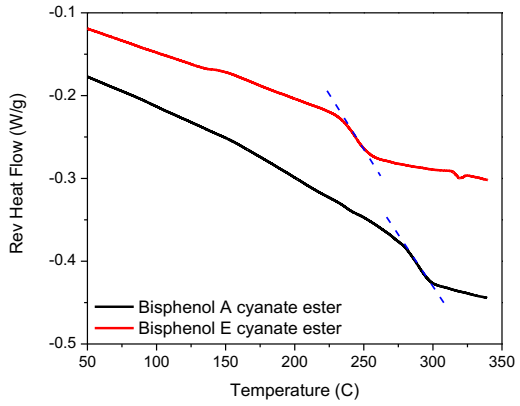

Figure 5-3. DSC scans showing the Tg of cured neat cyanate ester resins.

5.1.3 Epoxy-cyanate ester copolymer

Preliminary work demonstrates that cyanate ester-epoxy copolymer resin shows enhanced glass transition temperatures. The copolymer of cyanate ester and epoxy resins show the same T_g trend as discussed above. Dynamic mechanical analysis (DMA) characterization shows the copolymer with bisphenol A cyanate ester is ~ 25˚C higher in T_g than the copolymer with bisphenol E type cyanate ester (Figure 5-4).

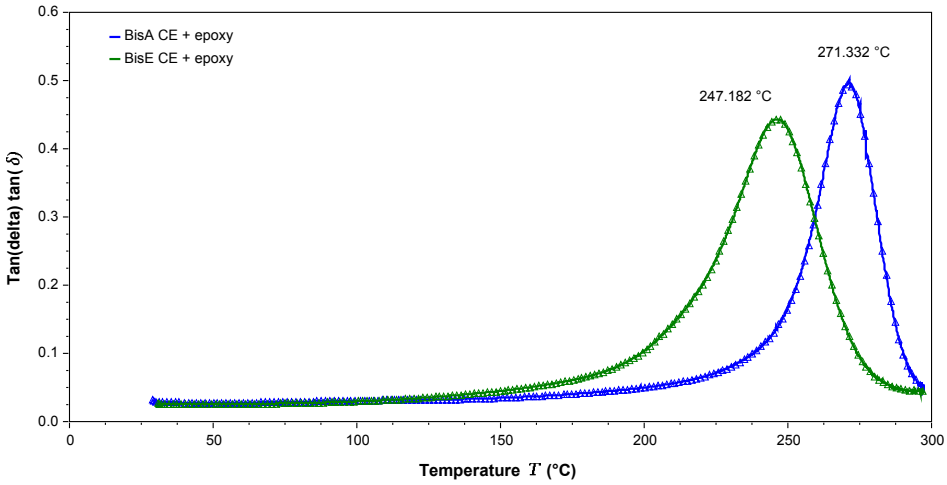

Figure 5-4. DMA curves of copolymers with bisphenol A and bisphenol E type cyanate esters.

In Fourier-transform infrared (FTIR) spectra (Figure 5-5a), the uncured sample shows a characteristic cyanate C≡N peak at 2237 and 2272 cm^{-1}, and an epoxide peak at 903 cm^{-1}. The spectrum of the cured sample shows diminished cyanate and epoxide peaks, suggesting reacted resin. Furthermore, the spectrum shows new peaks corresponding to the formation of triazine ring (1560 cm^{-1}), isocyanurate (1457 cm^{-1}), and cyanurate -O- (1367 cm^{-1}). We observed from the preliminary results that with increased amount of cyanate ester, and thus increased amount of aromatic triazine rings in the crosslinked polymer structure, the T_g of polymer resin increases (Figure 5-5b).

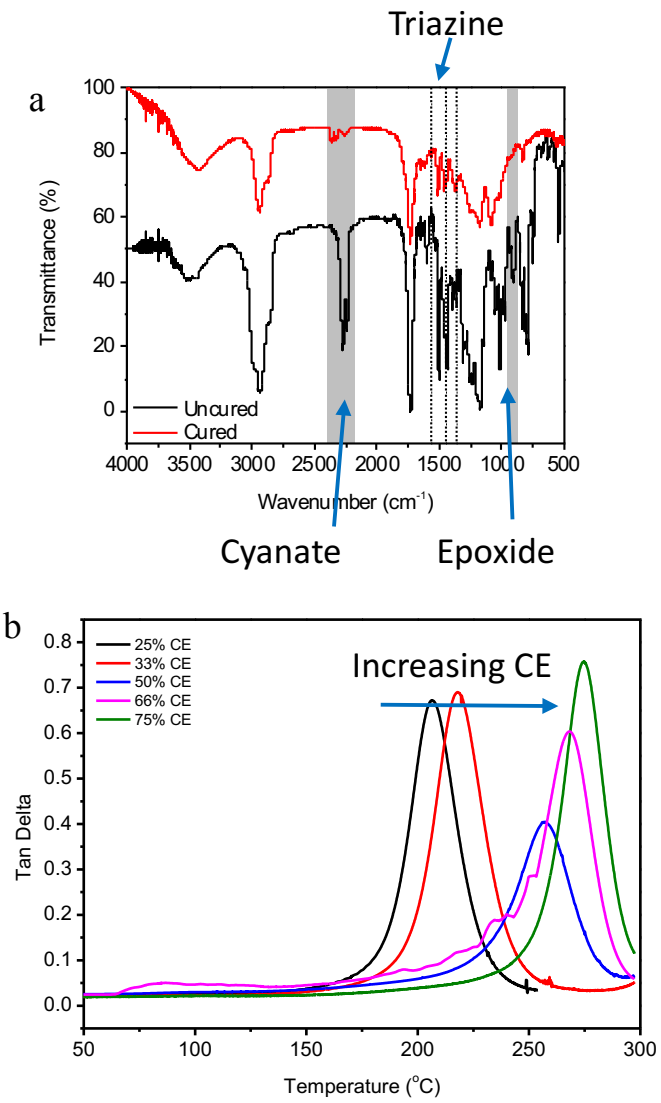

Figure 5-5. (a) FTIR of uncured (black) and cured (red) epoxy-cyanate ester blended resin. (b) T_g of cured polymer resins with increasing molar amount of cyanate ester (CE) in epoxy resin.

5.1.4 Thermal stability

Cyanate ester-epoxy copolymers were subjected to high-temperature environments using thermogravimetric analyzer (TGA). As shown in Figure 5-6a, degradation and rapid mass loss temperature is shifted to higher temperature with increased cyanate ester content. The decomposition temperature, defined as the temperature where 10% of mass loss is observed, increase by ~50˚C from the pure epoxy sample (352˚C) to pure cyanate ester sample (409˚C). In high-temperature storage test at 250˚C under nitrogen atmosphere, the cyanate ester-epoxy copolymer shows improved thermal stability compared to neat epoxy. During 5 hours of testing, neat biphenyl epoxy lost 6.59% weight, whereas the copolymer lost only 1.88%, which is roughly 3.5 times of the loss observed in epoxy. Additionally, polyimide is subjected to the same test environment as a high-temperature stable reference material, and the result suggest that the copolymer show thermal stability comparable to polyimide (Figure 5-6b).

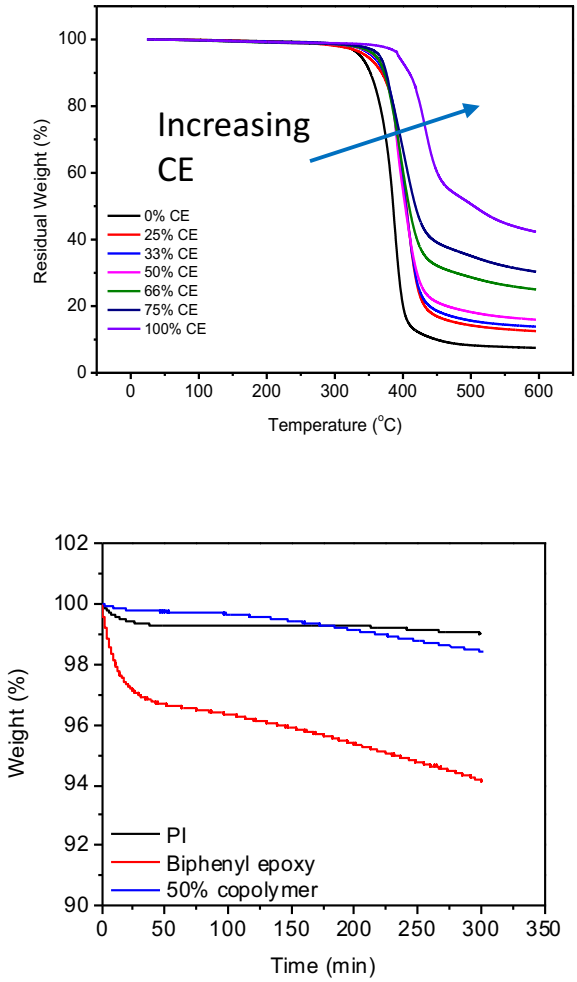

Figure 5-6. (a) Dynamic TGA scans of resins containing 0-100% cyanate ester from room temperature to 600˚C under nitrogen. (b) Isothermal TGA scans of cured polyimide, biphenyl epoxy, and cyanate ester-epoxy copolymer at 250˚C.

5.1.5 Summary and future work

The increasingly demanding need of automotive electronics poses stringent stability requirements for epoxy-based encapsulating compounds. We propose to modify epoxy resin by copolymerization with cyanate ester to improve the thermal stability of molding compounds because cyanate ester monomers trimerize to produce high-

temperature stable triazine groups in the network structure. It was shown that neat cyanate ester resin exhibit higher T_g than neat epoxy resin, which is expected due to the formation of triazines. Enhanced T_g and improved resin thermal stability is successfully demonstrated in the cyanate ester-epoxy copolymers. Initial thermal stability tests suggest the copolymers exhibit improved thermal stability in terms of higher thermal degradation temperature and lower mass loss under high-temperature storage conditions. Additional work is recommended to better understand the polymer structure in the copolymers and to study their high-temperature performance for electronic packages:

1. Determine the efficiency of triazine formation compared to the competing reaction between epoxide and cyanate ester to form oxazoline. The exact loading of triazine in the polymer network is important in predicting the thermal stability.

2. Adhesion of cyanate ester-epoxy copolymers to Si should be characterized. High-temperature effects on the adhesion performance is critical for the proper functioning of encapsulants. If delamination occurs, the encapsulant loses its ability to mechanically couple different parts of the package. Changes in adhesion strength can also be correlated with failure modes including dimensional stability and moisture absorption.

3. Moisture absorption of molding material should be studied and reduced with silica fillers. Absorbed moisture can result in localized pressure when

temperature approaches and goes above 100˚C, leading to failures such as popcorn cracking and delamination.

4. Long-term thermal aging test to determine the activation energy of thermal oxidation of epoxy and copolymer resins. Mass loss, density change, bending strength, are examples of material properties that change exponentially with time and can be used in the Arrhenius equation.

REFERENCES

[1] R. R. Tummala, E. J. Rymaszewski, and A. G. Klopfenstein, Eds., *Microelectronics Packaging Handbook*. Boston, MA: Springer US, 1997.

[2] R. R. Tummala, *Fundamentals of microsystems packaging*. McGraw-Hill, 2001.

[3] N. Toan, "Electronics Assembly," *Henkel Loctite Vietnam*, 2013.

[4] M. H. Chang, D. Das, P. V. Varde, and M. Pecht, "Light emitting diodes reliability review," *Microelectron. Reliab.*, vol. 52, no. 5, pp. 762–782, 2012.

[5] M. Ma, F. W. Mont, X. Yan, J. Cho, E. F. Schubert, G. B. Kim, and C. Sone, "Effects of the refractive index of the encapsulant on the light-extraction efficiency of light-emitting diodes," *Opt. Express*, vol. 19 Suppl 5, no. September, pp. A1135-40, Sep. 2011.

[6] E. K. Macdonald and M. P. Shaver, "Intrinsic high refractive index polymers," no. November 2014, 2015.

[7] T. Higashihara and M. Ueda, "Recent progress in high refractive index polymers," *Macromolecules*, vol. 48, no. 7, pp. 1915–1929, 2015.

[8] Y. Cheng, C. Lu, and B. Yang, "A Review on High Refractive Index Nanocomposites for Optical Applications," *Recent Patents Mater. Sci.*, vol. 4, no. 1, pp. 15–27, 2011.

[9] Y. Cheng, C. Lü, Z. Lin, Y. Liu, C. Guan, H. Lü, and B. Yang, "Preparation and properties of transparent bulk polymer nanocomposites with high nanophase contents," *J. Mater. Chem.*, vol. 18, no. 34, p. 4062, 2008.

[10] P. Tao, Y. Li, R. W. Siegel, and L. S. Schadler, "Transparent dispensible high-refractive index ZrO 2 /epoxy nanocomposites for LED encapsulation," *J. Appl. Polym. Sci.*, vol. 130, no. 5, pp. 3785–3793, Dec. 2013.

[11] P. Tao, Y. Li, A. Rungta, A. Viswanath, J. Gao, B. C. Benicewicz, R. W. Siegel, and L. S. Schadler, "TiO2 nanocomposites with high refractive index and transparency," *J. Mater. Chem.*, vol. 21, no. 46, p. 18623, 2011.

[12] B. M. Novak, "Hybrid Nanocomposite Materials- between inorganic glasses and organic polymers," *Adv. Mater.*, vol. 5, no. 6, pp. 422–433, Jun. 1993.

[13] B. Cai, O. Sugihara, H. I. Elim, T. Adschiri, and T. Kaino, "A novel preparation of high-refractive-index and highly transparent polymer nanohybrid composites," *Appl. Phys. Express*, vol. 4, no. 9, 2011.

[14] Y. H. Kim, J. Y. Bae, J. Jin, and B. S. Bae, "Sol-gel derived transparent zirconium-phenyl siloxane hybrid for robust high refractive index LED encapsulant," *ACS Appl. Mater. Interfaces*, vol. 6, no. 5, pp. 3115–3121, 2014.

[15] J. S. Kim, S. Yang, and B. S. Bae, "Thermally stable transparent sol-gel based siloxane hybrid material with high refractive index for light emitting diode (LED) encapsulation," *Chem. Mater.*, vol. 22, no. 11, pp. 3549–3555, 2010.

[16] J. L. H. Chau, C.-T. Tung, Y.-M. Lin, and A.-K. Li, "Preparation and optical properties of titania/epoxy nanocomposite coatings," *Mater. Lett.*, vol. 62, no. 19, pp. 3416–3418, Jul. 2008.

[17] G. Zhang, M. Chen, J. Zhang, B. He, H. Yang, and B. Yang, "Effective increase in the refractive index of novel transparent silicone hybrid films by introduction of functionalized silicon nanoparticles," *RSC Adv.*, vol. 5, no. 76, pp. 62128–62133, 2015.

[18] S. Takahashi, S. Hotta, A. Watanabe, N. Idota, K. Matsukawa, and Y. Sugahara, "Modification of TiO2 Nanoparticles with Oleyl Phosphate via Phase Transfer in the Toluene–Water System and Application of Modified Nanoparticles to Cyclo-Olefin-Polymer-Based Organic–Inorganic Hybrid Films Exhibiting High Refractive Indices," *ACS Appl. Mater. Interfaces*, vol. 9, no. 2, pp. 1907–1912, 2017.

[19] C. P. Wong, "MICROELECTRONICS: Flip the Chip," *Science*, vol. 290, no. 5500, pp. 2269–2270, Dec. 2000.

[20] B. Fennell, S. Lee, and D. F. Baldwin, "Rotational solder self-alignment mechanics modeling for a flip chip in the presence of a viscous fluid," *Microelectron. Reliab.*, vol. 65, pp. 217–224, Oct. 2016.

[21] Y. . Chan, P. . Tu, and K. . Hung, "Study of the self-alignment of no-flow underfill for micro-BGA assembly," *Microelectron. Reliab.*, vol. 41, no. 11, pp. 1867–1875, Nov. 2001.

[22] Z. Zhang, S. Luo, and C. P. Wong, “Flip Chip Underfill: Materials, Process, and Reliability,” in *Advanced Flip Chip Packaging*, H.-M. Tong, Y.-S. Lai, and C. P. Wong, Eds. Boston, MA: Springer US, 2013, pp. 155–199.

[23] Z. Zhang and C. P. Wong, “Recent Advances in Flip-Chip Underfill: Materials, Process, and Reliability,” *IEEE Trans. Adv. Packag.*, vol. 27, no. 3, pp. 515–524, Aug. 2004.

[24] B. Han and Y. Guo, “Thermal Deformation Analysis of Various Electronic Packaging Products by Moiré and Microscopic Moiré Interferometry,” *J. Electron. Packag.*, vol. 117, no. 3, p. 185, 1995.

[25] Y. Tsukada, S. Tsuchida, and Y. Mashimoto, “Surface laminar circuit packaging,” in *1992 Proceedings 42nd Electronic Components & Technology Conference*, 1992, pp. 22–27.

[26] J. B. Nysaether, P. Lundstrom, and J. Liu, “Measurements of solder bump lifetime as a function of underfill material properties,” *IEEE Trans. Components, Packag. Manuf. Technol. Part A*, vol. 21, no. 2, pp. 281–287, Jun. 1998.

[27] L. Fan, K.-S. Moon, and C. P. Wong, “Adhesion of underfill and components in flip chip encapsulation,” *J. Adhes. Sci. Technol.*, vol. 16, no. 2, pp. 213–223, Jan. 2002.

[28] Man-Lung Sham and Jang-Kyo Kim, “Effects of flux residue and thermomechanical stresses on delamination failure in flip chip packages,” in *International Symposium on Electronic Materials and Packaging*, 2000, pp. 274–281.

[29] Sejin Han and K. K. Wang, "Analysis of the flow of encapsulant during underfill encapsulation of flip-chips," *IEEE Trans. Components, Packag. Manuf. Technol. Part B*, vol. 20, no. 4, pp. 424–433, 1997.

[30] W.-B. Young and W.-L. Yang, "Underfill of Flip-Chip: The Effect of Contact Angle and Solder Bump Arrangement," *IEEE Trans. Adv. Packag.*, vol. 29, no. 3, pp. 647–653, Aug. 2006.

[31] I. J. Rasiah, P. S. Ho, M. Manoharan, C. L. Ng, and M. Chau, "Rheological analysis of an underfill material," in *Proceedings of 2nd Electronics Packaging Technology Conference*, 1998, pp. 354–358.

[32] Wen-Bin Young and Wen-Lin Yang, "Underfill viscous flow between parallel plates and solder bumps," *IEEE Trans. Components Packag. Technol.*, vol. 25, no. 4, pp. 695–700, Dec. 2002.

[33] Daqing Max Shi, K. McKeen, and B. Jenson, "Advances in flip chip underfill material cure rates and reliability," in *Proceedings. 4th International Symposium on Advanced Packaging Materials Processes, Properties and Interfaces*, 1998, pp. 29–32.

[34] R. W. Pennisi and M. V. Papageorge, "Adhesive and encapsulant material with fluxing properties," US 5128746, 1992.

[35] Z. Q. Zhang, S. H. Shi, and C. P. Wong, "Development of no-flow underfill materials for lead-free solder bumped flip-chip applications," *IEEE Trans.*

Components Packag. Technol., vol. 24, no. 1, pp. 59–66, 2001.

[36] C.-P. Wong and S.-H. Shi, "No-flow underfill of epoxy resin, anhydride, fluxing agent and surfactant," US6180696, 1998.

[37] "http://www.puiaudio.com/images/reflow_profile.jpg." .

[38] V. Jayaram, S. McCann, T.-C. Huang, S. Kawamoto, R. Pulugurtha, V. Smet, and R. Tummala, "Thermocompression Bonding Process Design and Optimization for Warpage Mitigation of Ultra-Thin Low-CTE Package Assemblies," in *2016 IEEE 66th Electronic Components and Technology Conference (ECTC)*, 2016, pp. 101–107.

[39] Kyoung-sik Moon, Lianhua Fan, and C. P. Wong, "The effect of toughening of no-flow underfill on fillet cracking of flip-chip device," in *Proceedings International Symposium on Advanced Packaging Materials Processes, Properties and Interfaces (IEEE Cat. No.01TH8562)*, 2001, pp. 333–340.

[40] K. Moon, L. Fan, and C. P. Wong, "Enhancement of Antifillet Cracking Performance for No- Flow Underfill by Toughening Method," 2002.

[41] V. Jíšová, "Curing mechanism of epoxides by imidazoles," *J. Appl. Polym. Sci.*, vol. 34, no. 7, pp. 2547–2558, 1987.

[42] Y. R. Ham, S. H. Kim, Y. J. Shin, D. H. Lee, M. Yang, J. H. Min, and J. S. Shin, "A comparison of some imidazoles in the curing of epoxy resin," *J. Ind. Eng. Chem.*,

vol. 16, no. 4, pp. 556–559, 2010.

[43] B. Ellis, Ed., *Chemistry and Technology of Epoxy Resins*. Dordrecht: Springer Netherlands, 1993.

[44] J. M. Barton and P. M. Shepherd, "The Curing Reaction of an Epoxide Resin with 2-Ethyl-4-methylimidazole, a Calorimetric Study of the Kinetics of Formation of Epoxide-Imidazole Adducts," *Die Makromol. Chemie*, vol. 176, pp. 919–930, 1975.

[45] F. Ricciardi, W. A. Romanchick, and M. M. Joullie, "Mechanism of imidazole catalysis in the curing of epoxy resins," *J. Polym. Sci. Polym. Chem. Ed.*, vol. 21, no. 5, pp. 1475–1490, May 1983.

[46] J. J. Licari and D. W. Swanson, *Adhesives technology for electronic applications: materials, processing, reliability*. William Andrew Pub, 2011.

[47] J. Qu and C. P. Wong, "Effective elastic modulus of underfill material for flip-chip applications," *IEEE Trans. Components Packag. Technol.*, vol. 25, no. 2, pp. 53–55, 2002.

[48] C. P. Wong and R. S. Bollampally, "Comparative study of thermally conductive fillers for use in liquid encapsulants for electronic packaging," *IEEE Trans. Adv. Packag.*, vol. 22, no. 1, pp. 54–59, 1999.

[49] Z. Lin, A. Mcnamara, Y. Liu, K. Moon, and C.-P. Wong, "Exfoliated hexagonal boron nitride-based polymer nanocomposite with enhanced thermal conductivity for

electronic encapsulation," *Compos. Sci. Technol.*, vol. 90, pp. 123–128, Jan. 2014.

[50] Z. Lin, Y. Liu, S. Raghavan, K. Moon, S. K. Sitaraman, and C. Wong, "Magnetic alignment of hexagonal boron nitride platelets in polymer matrix: toward high performance anisotropic polymer composites for electronic encapsulation.," *ACS Appl. Mater. Interfaces*, vol. 5, no. 15, pp. 7633–40, Aug. 2013.

[51] G. Hong, T. M. Schutzius, S. Zimmermann, B. R. Burg, J. Zürcher, T. Brunschwiler, G. Tagliabue, B. Michel, and D. Poulikakos, "In Situ Assembly in Confined Spaces of Coated Particle Scaffolds as Thermal Underfills with Extraordinary Thermal Conductivity," *ACS Appl. Mater. Interfaces*, vol. 7, no. 1, pp. 838–844, Jan. 2015.

[52] G. D. SCOTT, "Packing of Spheres: Packing of Equal Spheres," *Nature*, vol. 188, no. 4754, pp. 908–909, Dec. 1960.

[53] E. Santiso and E. Müller, "Dense packing of binary and polydisperse hard spheres," *Mol. Phys.*, vol. 100, no. 15, pp. 2461–9, 2002.

[54] S. M. K. Rassouly, "The packing density of `perfect' binary mixtures," *Powder Technol.*, vol. 103, no. 2, pp. 145–150, Jul. 1999.

[55] F. Zok, F. F. Lange, and J. R. Porter, "Packing Density of Composite Powder Mixtures," *J. Am. Ceram. Soc.*, vol. 74, no. 8, pp. 1880–1885, Aug. 1991.

[56] J. Bae, W. Kim, S. Cho, and S. Lee, "The properties of AlN-filled epoxy molding compounds by the effects of filler size distribution," vol. 5, pp. 5907–5913, 2000.

[57] C.-P. Wong and S.-H. Shi, “No-flow underfill of epoxy resin, anhydride, fluxing agent and surfactant,” US 6180696, 1998.

[58] Z. Zhang, P. Zhu, and C. P. Wong, “Flip-Chip Underfill: Materials, Process, and Reliability,” in *Materials for Advanced Packaging*, D. Lu and C. P. Wong, Eds. Cham: Springer International Publishing, 2017, pp. 331–371.

[59] B. Pukánszky, “Interfaces and interphases in multicomponent materials: past, present, future,” *Eur. Polym. J.*, vol. 41, no. 4, pp. 645–662, Apr. 2005.

[60] J. A. Forrest, K. Dalnoki-Veress, J. R. Stevens, and J. R. Dutcher, “Effect of Free Surfaces on the Glass Transition Temperature of Thin Polymer Films,” *Phys. Rev. Lett.*, vol. 77, no. 10, pp. 2002–2005, Sep. 1996.

[61] J. S. Sharp and J. A. Forrest, “Free Surfaces Cause Reductions in the Glass Transition Temperature of Thin Polystyrene Films,” *Phys. Rev. Lett.*, vol. 91, no. 23, p. 235701, Dec. 2003.

[62] M. E. Mackay, T. T. Dao, A. Tuteja, D. L. Ho, B. Van Horn, H.-C. Kim, and C. J. Hawker, “Nanoscale effects leading to non-Einstein-like decrease in viscosity,” *Nat. Mater.*, vol. 2, no. 11, pp. 762–766, 2003.

[63] P. Rittigstein and J. M. Torkelson, “Polymer–nanoparticle interfacial interactions in polymer nanocomposites: Confinement effects on glass transition temperature and suppression of physical aging,” *J. Polym. Sci. Part B Polym. Phys.*, vol. 44, no. 20, pp. 2935–2943, Oct. 2006.

[64] B. J. Ash, L. S. Schadler, and R. W. Siegel, “Glass transition behavior of alumina/polymethylmethacrylate nanocomposites,” *Mater. Lett.*, vol. 55, no. 1–2, pp. 83–87, Jul. 2002.

[65] X. Qin, W. Xia, R. Sinko, and S. Keten, “Tuning Glass Transition in Polymer Nanocomposites with Functionalized Cellulose Nanocrystals through Nanoconfinement,” *Nano Lett.*, vol. 15, no. 10, pp. 6738–6744, 2015.

[66] P. Rittigstein, R. D. Priestley, L. J. Broadbelt, and J. M. Torkelson, “Model polymer nanocomposites provide an understanding of confinement effects in real nanocomposites.,” *Nat. Mater.*, vol. 6, no. April, pp. 278–282, 2007.

[67] C. J. Ellison and J. M. Torkelson, “The distribution of glass-transition temperatures in nanoscopically confined glass formers,” *Nat. Mater.*, vol. 2, no. 10, pp. 695–700, Sep. 2003.

[68] D. Ciprai, K. Jacob, and R. Tannenbaum, “Characterization of polymer nanocomposite interphase and its impact on mechanical properties,” *Macromolecules*, vol. 39, no. 19, pp. 6565–6573, 2006.

[69] J.-S. Jang, B. Bouveret, J. Suhr, and R. F. Gibson, “Combined numerical/experimental investigation of particle diameter and interphase effects on coefficient of thermal expansion and young’s modulus of SiO2/epoxy nanocomposites,” *Polym. Compos.*, vol. 33, no. 8, pp. 1415–1423, Aug. 2012.

[70] A. S. Blivi, F. Benhui, J. Bai, D. Kondo, and F. Bédoui, “Experimental evidence of

size effect in nano-reinforced polymers: Case of silica reinforced PMMA," *Polym. Test.*, vol. 56, pp. 337–343, 2016.

[71] T. V. M. Ndoro, M. C. Böhm, and F. Müller-Plathe, "Interface and interphase dynamics of polystyrene chains near grafted and ungrafted silica nanoparticles," *Macromolecules*, vol. 45, no. 1, pp. 171–179, 2012.

[72] A. P. Holt, P. J. Griffin, V. Bocharova, A. L. Agapov, A. E. Imel, M. D. Dadmun, J. R. Sangoro, and A. P. Sokolov, "Dynamics at the Polymer/Nanoparticle Interface in Poly(2-vinylpyridine)/Silica Nanocomposites," *Macromolecules*, vol. 47, no. 5, pp. 1837–1843, Mar. 2014.

[73] N. Jouault, J. F. Moll, D. Meng, K. Windsor, S. Ramcharan, C. Kearney, and S. K. Kumar, "Bound Polymer Layer in Nanocomposites," *ACS Macro Lett.*, vol. 2, no. 5, pp. 371–374, May 2013.

[74] C. Antonelli, B. Serrano, J. Baselga, R. Ozisik, and J. C. Cabanelas, "Interfacial characterization of epoxy/silica nanocomposites measured by fluorescence," *Eur. Polym. J.*, vol. 62, pp. 31–42, Jan. 2015.

[75] D. Brown, V. Marcadon, P. Ml, N. D. Albrola, and P. Me, "Effect of Filler Particle Size on the Properties of Model Nanocomposites Effect of Filler Particle Size on the Properties of Model Nanocomposites," *Macromolecules*, vol. 41, pp. 1499–1511, 2008.

[76] H. Zhang, Z. Zhang, K. Friedrich, and C. Eger, "Property improvements of in situ

epoxy nanocomposites with reduced interparticle distance at high nanosilica content," *Acta Mater.*, vol. 54, no. 7, pp. 1833–1842, 2006.

[77] E. Petrovicova, R. Knight, L. S. Schadler, and T. E. Twardowski, "Nylon 11/silica nanocomposite coatings applied by the HVOF process. II. Mechanical and barrier properties," *J. Appl. Polym. Sci.*, vol. 78, no. 13, pp. 2272–2289, Dec. 2000.

[78] S. E. Harton, S. K. Kumar, H. Yang, T. Koga, K. Hicks, H. Lee, J. Mijovic, M. Liu, R. S. Vallery, and D. W. Gidley, "Immobilized Polymer Layers on Spherical Nanoparticles," *Macromolecules*, vol. 43, no. 7, pp. 3415–3421, Apr. 2010.

[79] Y. Sun, Z. Zhang, K.-S. Moon, and C. P. Wong, "Glass transition and relaxation behavior of epoxy nanocomposites," *J. Polym. Sci. Part B Polym. Phys.*, vol. 42, no. 21, pp. 3849–3858, Nov. 2004.

[80] B. Natarajan, Y. Li, H. Deng, L. C. Brinson, and L. S. Schadler, "Effect of Interfacial Energetics on Dispersion and Glass Transition Temperature in Polymer Nanocomposites," *Macromolecules*, vol. 46, no. 7, pp. 2833–2841, Apr. 2013.

[81] R. Qiao, H. Deng, K. W. Putz, and L. C. Brinson, "Effect of particle agglomeration and interphase on the glass transition temperature of polymer nanocomposites," *J. Polym. Sci. Part B Polym. Phys.*, vol. 49, no. 10, pp. 740–748, 2011.

[82] T. Ramanathan, S. Stankovich, D. A. Dikin, H. Liu, H. Shen, S. T. Nguyen, and L. C. Brinson, "Graphitic nanofillers in PMMA nanocomposites—An investigation of particle size and dispersion and their influence on nanocomposite properties," *J.*

Polym. Sci. Part B Polym. Phys., vol. 45, no. 15, pp. 2097–2112, Aug. 2007.

[83] K. Putz, R. Krishnamoorti, and P. F. Green, "The role of interfacial interactions in the dynamic mechanical response of functionalized SWNT–PS nanocomposites," *Polymer*, vol. 48, no. 12, pp. 3540–3545, Jun. 2007.

[84] Y. Yang, A. Oztekin, S. Neti, and S. Mohapatra, "Particle agglomeration and properties of nanofluids," *J. Nanoparticle Res.*, vol. 14, no. 5, p. 852, May 2012.

[85] F. Duan, D. Kwek, and A. Crivoi, "Viscosity affected by nanoparticle aggregation in Al2O3-water nanofluids," *Nanoscale Res. Lett.*, vol. 6, no. 1, p. 248, Jun. 2011.

[86] Y.-P. Zhu, T.-Y. Ma, Y.-L. Liu, T.-Z. Ren, and Z.-Y. Yuan, "Metal phosphonate hybrid materials: from densely layered to hierarchically nanoporous structures," *Inorg. Chem. Front.*, vol. 1, no. 5, p. 360, 2014.

[87] C. S. Pauly, A.-C. Genix, J. G. Alauzun, M. Sztucki, J. Oberdisse, and P. Hubert Mutin, "Surface modification of alumina-coated silica nanoparticles in aqueous sols with phosphonic acids and impact on nanoparticle interactions," *Phys. Chem. Chem. Phys.*, vol. 17, no. 29, pp. 19173–19182, 2015.

[88] A. Bulusu, S. A. Paniagua, B. A. MacLeod, A. K. Sigdel, J. J. Berry, D. C. Olson, S. R. Marder, and S. Graham, "Efficient Modification of Metal Oxide Surfaces with Phosphonic Acids by Spray Coating," *Langmuir*, vol. 29, no. 12, pp. 3935–3942, Mar. 2013.

[89] M.-A. Neouze and U. Schubert, “Surface Modification and Functionalization of Metal and Metal Oxide Nanoparticles by Organic Ligands,” *Monatshefte für Chemie - Chem. Mon.*, vol. 139, no. 3, pp. 183–195, Mar. 2008.

[90] J. De Roo, F. Van den Broeck, K. De Keukeleere, J. C. Martins, I. Van Driessche, and Z. Hens, “Unravelling the Surface Chemistry of Metal Oxide Nanocrystals, the Role of Acids and Bases,” *J. Am. Chem. Soc.*, vol. 136, no. 27, pp. 9650–9657, Jul. 2014.

[91] L. T. Zhuravlev, “The surface chemistry of amorphous silica. Zhuravlev model,” *Colloids Surfaces A Physicochem. Eng. Asp.*, vol. 173, no. 1–3, pp. 1–38, 2000.

[92] L. T. Zhuravlev, “Concentration of hydroxyl groups on the surface of amorphous silicas,” *Langmuir*, vol. 3, no. 3, pp. 316–318, May 1987.

[93] N. Herzer, S. Hoeppener, U. S. Schubert, U. S. Schubert, V. Stadler, J. Su, M. Mrksich, G. M. Whitesides, G. M. Whitesides, P. E. Laibinis, C. J. Hawker, C. Teichert, W. Kern, G. Trimmel, and G. Hadziioannou, “Fabrication of patterned silane based self-assembled monolayers by photolithography and surface reactions on silicon-oxide substrates,” *Chem. Commun.*, vol. 46, no. 31, p. 5634, 2010.

[94] E. P. Plueddemann, *Silane Coupling Agents*. Boston, MA: Springer US, 1982.

[95] J. J. Gooding and S. Ciampi, “The molecular level modification of surfaces: from self-assembled monolayers to complex molecular assemblies,” *Chem. Soc. Rev.*, vol. 40, no. 5, p. 2704, 2011.

[96] R. Maoz, H. Cohen, and J. Sagiv, “Specific Nonthermal Chemical Structural Transformation Induced by Microwaves in a Single Amphiphilic Bilayer Self-Assembled on Silicon,” *Langmuir*, vol. 14, no. 21, pp. 5988–5993, Oct. 1998.

[97] G. Balasundaram, M. Sato, and T. J. Webster, “Using hydroxyapatite nanoparticles and decreased crystallinity to promote osteoblast adhesion similar to functionalizing with RGD,” *Biomaterials*, vol. 27, no. 14, pp. 2798–2805, 2006.

[98] D. Bikiaris, P. Matzinos, A. Larena, V. Flaris, and C. Panayiotou, “Use of silane agents and poly(propylene-g-maleic anhydride) copolymer as adhesion promoters in glass fiber/polypropylene composites,” *J. Appl. Polym. Sci.*, vol. 81, no. 3, pp. 701–709, Jul. 2001.

[99] I. Mannelli, R. Reigada, I. Suárez, D. Janner, A. Carrilero, P. Mazumder, F. Sagués, V. Pruneri, and M. Lakadamyali, “Functionalized Surfaces with Tailored Wettability Determine Influenza A Infectivity,” *ACS Appl. Mater. Interfaces*, vol. 8, no. 24, pp. 15058–15066, Jun. 2016.

[100] Y. Xie, C. A. S. Hill, Z. Xiao, H. Militz, and C. Mai, “Silane coupling agents used for natural fiber/polymer composites: A review,” *Compos. Part A Appl. Sci. Manuf.*, vol. 41, no. 7, pp. 806–819, 2010.

[101] S. P. Pujari, L. Scheres, A. T. M. Marcelis, and H. Zuilhof, “Covalent surface modification of oxide surfaces,” *Angew. Chemie - Int. Ed.*, vol. 53, no. 25, pp. 6322–6356, 2014.

[102] H.-J. Kang, W. Meesiri, and F. D. Blum, “Nuclear magnetic resonance studies of the hydrolysis and molecular motion of aminopropylsilane,” *Mater. Sci. Eng. A*, vol. 126, no. 1–2, pp. 265–270, Jun. 1990.

[103] M.-C. B. Salon, G. Gerbaud, M. Abdelmouleh, C. Bruzzese, S. Boufi, and M. N. Belgacem, “Studies of interactions between silane coupling agents and cellulose fibers with liquid and solid-state NMR,” *Magn. Reson. Chem.*, vol. 45, no. 6, pp. 473–483, Jun. 2007.

[104] R. M. Pasternack, S. R. Amy, and Y. J. Chaba, “Attachment of 3- Aminopropyl triethoxysilane on Silicon Oxide Surfaces: Dependence on Solution Temperature,” *Langmuir*, vol. 24, no. 9, pp. 12963–12971, 2008.

[105] G. Soliveri, V. Pifferi, R. Annunziata, L. Rimoldi, V. Aina, G. Cerrato, L. Falciola, G. Cappelletti, and D. Meroni, “Alkylsilane–SiO2 Hybrids. A Concerted Picture of Temperature Effects in Vapor Phase Functionalization,” *J. Phys. Chem. C*, vol. 119, no. 27, pp. 15390–15400, Jul. 2015.

[106] I. Haller, “Covalently attached organic monolayers on semiconductor surfaces,” *J. Am. Chem. Soc.*, vol. 100, no. 26, pp. 8050–8055, Dec. 1978.

[107] A. Markov, K. Greben, D. Mayer, A. Offenhäusser, and R. Wördenweber, “In Situ Analysis of the Growth and Dielectric Properties of Organic Self-Assembled Monolayers: A Way To Tailor Organic Layers for Electronic Applications,” *ACS Appl. Mater. Interfaces*, vol. 8, no. 25, pp. 16451–16456, Jun. 2016.

[108] C. Pick, C. Argento, G. Drazer, and J. Frechette, "Micropatterned Charge Heterogeneities via Vapor Deposition of Aminosilanes," *Langmuir*, vol. 31, no. 39, pp. 10725–10733, Oct. 2015.

[109] F. Zhang, K. Sautter, A. M. Larsen, D. A. Findley, R. C. Davis, H. Samha, and M. R. Linford, "Chemical Vapor Deposition of Three Aminosilanes on Silicon Dioxide: Surface Characterization, Stability, Effects of Silane Concentration, and Cyanine Dye Adsorption," *Langmuir*, vol. 26, no. 18, pp. 14648–14654, Sep. 2010.

[110] Y. Sun, Z. Zhang, and C. P. Wong, "Study on mono-dispersed nano-size silica by surface modification for underfill applications.," *J. Colloid Interface Sci.*, vol. 292, no. 2, pp. 436–44, Dec. 2005.

[111] Y. Li, B. Han, S. Wen, Y. Lu, H. Yang, L. Zhang, and L. Liu, "Effect of the temperature on surface modification of silica and properties of modified silica filled rubber composites," *Compos. Part A Appl. Sci. Manuf.*, vol. 62, pp. 52–59, 2014.

[112] D. Sun, X. Miao, K. Zhang, H. Kim, and Y. Yuan, "Triazole-forming waterborne polyurethane composites fabricated with silane coupling agent functionalized nano-silica," *J. Colloid Interface Sci.*, vol. 361, no. 2, pp. 483–490, Sep. 2011.

[113] K.-C. Chang, C.-Y. Lin, H.-F. Lin, S.-C. Chiou, W.-C. Huang, J.-M. Yeh, and J.-C. Yang, "Thermally and mechanically enhanced epoxy resin-silica hybrid materials containing primary amine-modified silica nanoparticles," *J. Appl. Polym. Sci.*, vol. 108, no. 3, pp. 1629–1635, May 2008.

[114] Q. Guo, P. Zhu, G. Li, J. Wen, T. Wang, D. (Daniel) Lu, R. Sun, and C. Wong, "Study on the effects of interfacial interaction on the rheological and thermal performance of silica nanoparticles reinforced epoxy nanocomposites," *Compos. Part B Eng.*, vol. 116, pp. 388–397, May 2017.

[115] X. Huang, Y. Zheng, P. Jiang, and Y. Yin, "Influence of nanoparticle surface treatment on the electrical properties of cycloaliphatic epoxy nanocomposites," *IEEE Trans. Dielectr. Electr. Insul.*, vol. 17, no. 2, pp. 635–643, 2010.

[116] Y. Li, J. Yu, and Z.-X. Guo, "The influence of silane treatment on nylon 6/nano-SiO2in situ polymerization," *J. Appl. Polym. Sci.*, vol. 84, no. 4, pp. 827–834, Apr. 2002.

[117] Zhuqing Zhang and C. P. Wong, "Double-layer no-flow underfill materials and process," *IEEE Trans. Adv. Packag.*, vol. 26, no. 2, pp. 199–205, May 2003.

[118] T. Nonaka, S. Niizeki, N. Asahi, and K. Fujimaru, "Low temperature touch down and suppressing filler trapping bonding process with a wafer level pre-applied underfilling film adhesive," in *2012 IEEE 62nd Electronic Components and Technology Conference*, 2012, pp. 444–449.

[119] D. J. Duffy, M. Desai, H. Bhavsar, L. Xin, J. Liu, and B. Tolla, "Rheology design considerations for one step chip attach materials (OSCA) used for conventional mass reflow processing," in *2015 IEEE 65th Electronic Components and Technology Conference (ECTC)*, 2015, pp. 180–186.

[120] F. Svec, P. A. Levkin, and J. M. J. Frechet, "Superhydrophobic and superhydrophilic materials, surfaces and methods," US Patent 20110033663, 2009.

[121] P. A. Levkin, F. Svec, and J. M. J. Fréchet, "Porous Polymer Coatings: a Versatile Approach to Superhydrophobic Surfaces," *Adv. Funct. Mater.*, vol. 19, no. 12, pp. 1993–1998, Jun. 2009.

[122] F. L. Geyer, E. Ueda, U. Liebel, N. Grau, and P. A. Levkin, "Superhydrophobic-Superhydrophilic Micropatterning: Towards Genome-on-a-Chip Cell Microarrays," *Angew. Chemie Int. Ed.*, vol. 50, no. 36, pp. 8424–8427, Aug. 2011.

[123] Q. Pan, H. Jin, and H. Wang, "Fabrication of superhydrophobic surfaces on interconnected Cu(OH)2 nanowires via solution-immersion," *Nanotechnology*, vol. 18, no. 35, p. 355605, Sep. 2007.

[124] T. Liu, Y. Yin, S. Chen, X. Chang, and S. Cheng, "Super-hydrophobic surfaces improve corrosion resistance of copper in seawater," *Electrochim. Acta*, vol. 52, no. 11, pp. 3709–3713, Mar. 2007.

[125] K. Ji, J. Zhang, J. Chen, G. Meng, Y. Ding, and Z. Dai, "Centrifugation-Assisted Fog-Collecting Abilities of Metal-Foam Structures with Different Surface Wettabilities," *ACS Appl. Mater. Interfaces*, vol. 8, no. 15, pp. 10005–10013, Apr. 2016.

[126] M. A. Osman and B. A. Keller, "Wettability of native silver surfaces," *Appl. Surf. Sci.*, vol. 99, no. 3, pp. 261–263, Jul. 1996.

[127] F. De Angelis, F. Gentile, F. Mecarini, G. Das, M. Moretti, P. Candeloro, M. L. Coluccio, G. Cojoc, A. Accardo, C. Liberale, R. P. Zaccaria, G. Perozziello, L. Tirinato, A. Toma, G. Cuda, R. Cingolani, and E. Di Fabrizio, "Breaking the diffusion limit with super-hydrophobic delivery of molecules to plasmonic nanofocusing SERS structures," *Nat. Photonics*, vol. 5, no. 11, pp. 682–687, Sep. 2011.

[128] E. Miele, M. Malerba, M. Dipalo, E. Rondanina, A. Toma, F. De Angelis, E. Rondanina, A. Toma, F. De Angelis, and F. De Angelis, "Controlling wetting and self-assembly dynamics by tailored hydrophobic and oleophobic surfaces," *Adv. Mater.*, vol. 26, no. 24, pp. 4179–4183, Jun. 2014.

[129] Y. Kaizuma, "Hydrophilic Silicon Oxide Film by Pulsed Plasma CVD," *J. Vac. Soc. Japan*, vol. 50, no. 10, pp. 635–638, 2007.

[130] S. H. Kim, S. Nam, J. Jang, K. Hong, C. Yang, D. S. Chung, C. E. Park, and W.-S. Choi, "Effect of the hydrophobicity and thickness of polymer gate dielectrics on the hysteresis behavior of pentacene-based field-effect transistors," *J. Appl. Phys.*, vol. 105, no. 10, p. 104509, May 2009.

[131] T. Kobayashi, K. Shimizu, Y. Kaizuma, and S. Konishi, "Novel combination of hydrophilic/hydrophobic surface for large wettability difference and its application to liquid manipulation," *Lab Chip*, vol. 11, no. 4, pp. 639–644, Feb. 2011.

[132] S. Suzuki, A. Nakajima, M. Sakai, J.-H. Song, N. Yoshida, Y. Kameshima, and K.

Okada, “Sliding acceleration of water droplets on a surface coated with fluoroalkylsilane and octadecyltrimethoxysilane,” *Surf. Sci.*, vol. 600, no. 10, pp. 2214–2219, May 2006.

[133] Y. Wu, M. Kouno, N. Saito, F. Andrei Nae, Y. Inoue, and O. Takai, “Patterned hydrophobic–hydrophilic templates made from microwave-plasma enhanced chemical vapor deposited thin films,” *Thin Solid Films*, vol. 515, no. 9, pp. 4203–4208, Mar. 2007.

[134] Y. Wu, H. Sugimura, Y. Inoue, and O. Takai, “Preparation of hard and ultra water-repellent silicon oxide films by microwave plasma-enhanced CVD at low substrate temperatures,” *Thin Solid Films*, vol. 435, no. 1–2, pp. 161–164, Jul. 2003.

[135] T. Ishizaki, N. Saito, and O. Takai, “Correlation of Cell Adhesive Behaviors on Superhydrophobic, Superhydrophilic, and Micropatterned Superhydrophobic/Superhydrophilic Surfaces to Their Surface Chemistry,” *Langmuir*, vol. 26, no. 11, pp. 8147–8154, Jun. 2010.

[136] J. Frahn, G. Malsch, H. Matuschewski, U. Schedler, and H.-H. Schwarz, “Separation of aromatic/aliphatic hydrocarbons by photo-modified poly(acrylonitrile) membranes,” *J. Memb. Sci.*, vol. 234, no. 1–2, pp. 55–65, May 2004.

[137] D. Zahner, J. Abagat, F. Svec, J. M. J. Fréchet, and P. A. Levkin, “A Facile Approach to Superhydrophilic-Superhydrophobic Patterns in Porous Polymer Films,” *Adv. Mater.*, vol. 23, no. 27, pp. 3030–3034, Jul. 2011.

[138] V. Krishnamurthy and I. L. Kamel, “Argon plasma treatment of glass surfaces,” *J. Mater. Sci.*, vol. 24, no. 9, pp. 3345–3352, Sep. 1989.

[139] M. J. Hancock, J. He, J. F. Mano, and A. Khademhosseini, “Surface-Tension-Driven Gradient Generation in a Fluid Stripe for Bench-Top and Microwell Applications,” *Small*, vol. 7, no. 7, pp. 892–901, Apr. 2011.

[140] Z. Luo, G. Qi, K. Chen, M. Zou, L. Yuwen, X. Zhang, W. Huang, and L. Wang, “Microwave-Assisted Preparation of White Fluorescent Graphene Quantum Dots as a Novel Phosphor for Enhanced White-Light-Emitting Diodes,” *Adv. Funct. Mater.*, vol. 26, no. 16, pp. 2739–2744, Apr. 2016.

[141] E. F. Schubert, “Solid-State Light Sources Getting Smart,” *Science*, vol. 308, no. 5726, pp. 1274–1278, 2005.

[142] S. Reineke, F. Lindner, G. Schwartz, N. Seidler, K. Walzer, B. Lüssem, and K. Leo, “White organic light-emitting diodes with fluorescent tube efficiency,” *Nature*, vol. 459, no. 7244, pp. 234–238, May 2009.

[143] E. F. Schubert, T. Gessmann, J. K. Kim, E. F. Schubert, T. Gessmann, J. K. Kim, and J. K. Schubert, E. F., Gessmann, T. and Kim, “Light emitting diodes,” in *Kirk-Othmer Encyclopedia of Chemical Technology.*, Hoboken, NJ, USA: John Wiley & Sons, Inc., 2005, pp. 1–31.

[144] S. Chhajed, W. Lee, J. Cho, E. F. Schubert, and J. K. Kim, “Strong light extraction enhancement in GaInN light-emitting diodes by using self-organized nanoscale

patterning of p-type GaN," *Appl. Phys. Lett.*, vol. 98, no. 7, p. 71102, Feb. 2011.

[145] A. Keppens, W. R. Ryckaert, G. Deconinck, and P. Hanselaer, "Modeling high power light-emitting diode spectra and their variation with junction temperature," *J. Appl. Phys.*, vol. 108, no. 4, 2010.

[146] N. Han, T. Viet Cuong, M. Han, B. Deul Ryu, S. Chandramohan, J. Bae Park, J. Hye Kang, Y.-J. Park, K. Bok Ko, H. Yun Kim, H. Kyu Kim, J. Hyoung Ryu, Y. S. Katharria, C.-J. Choi, and C.-H. Hong, "Improved heat dissipation in gallium nitride light-emitting diodes with embedded graphene oxide pattern," *Nat. Commun.*, vol. 4, p. 1452, Feb. 2013.

[147] M. Meneghini, L.-R. Trevisanello, G. Meneghesso, and E. Zanoni, "A Review on the Reliability of GaN-Based LEDs," *IEEE Trans. Device Mater. Reliab.*, vol. 8, no. 2, pp. 323–331, Jun. 2008.

[148] F. W. Mont, J. K. Kim, M. F. Schubert, E. F. Schubert, and R. W. Siegel, "High-refractive-index TiO2-nanoparticle-loaded encapsulants for light-emitting diodes," *J. Appl. Phys.*, vol. 103, no. 8, p. 83120, 2008.

[149] S. Yang, J.-S. Kim, J. Jin, S.-Y. Kwak, and B.-S. Bae, "Cycloaliphatic epoxy oligosiloxane-derived hybrid materials for a high-refractive index LED encapsulant," *J. Appl. Polym. Sci.*, vol. 122, no. 4, pp. 2478–2485, Nov. 2011.

[150] J.-S. Kim, S. Yang, and B.-S. Bae, "Thermally Stable Transparent Sol−Gel Based Siloxane Hybrid Material with High Refractive Index for Light Emitting Diode

(LED) Encapsulation," *Chem. Mater.*, vol. 22, no. 11, pp. 3549–3555, Jun. 2010.

[151] D. W. Mosley, G. Khanarian, D. M. Conner, D. L. Thorsen, T. Zhang, and M. Wills, "High refractive index thermally stable phenoxyphenyl and phenylthiophenyl silicones for light-emitting diode applications," *J. Appl. Polym. Sci.*, vol. 131, no. 3, 2014.

[152] Y. H. Kim, J. Y. Bae, J. Jin, and B. S. Bae, "Sol-gel derived transparent zirconium-phenyl siloxane hybrid for robust high refractive index LED encapsulant," *ACS Appl. Mater. Interfaces*, vol. 6, pp. 3115–3121, 2014.

[153] N. Nakayama and T. Hayashi, "Preparation and characterization of TiO2 and polymer nanocomposite films with high refractive index," *J. Appl. Polym. Sci.*, vol. 105, no. 6, pp. 3662–3672, Sep. 2007.

[154] T. C. Monson, M. a. Rodriguez, J. L. Leger, T. E. Stevens, and D. L. Huber, "A simple low-cost synthesis of brookite TiO2 nanoparticles," *J. Mater. Res.*, vol. 28, no. 3, pp. 348–353, Nov. 2012.

[155] Y. H. Kim, Y.-W. Lim, D. Lee, Y. H. Kim, and B.-S. Bae, "A highly adhesive siloxane LED encapsulant optimized for high thermal stability and optical efficiency," *J. Mater. Chem. C*, vol. 4, no. 46, pp. 10791–10796, Nov. 2016.

[156] R. Yamazaki and M. Yoshitake, "Curable silicone composition, cured product thereof, and optical semiconductor device," US9048406, 2013.

[157] G. Wilkinson, F. G. A. Stone, and E. W. Abel, Eds., *Comprehensive organometallic chemistry: the synthesis, reactions, and structures of organometallic compounds*. Pergamon Press, 1982.

[158] M. Andriot, J. V Degroot, R. Meeks, E. Gerlach, M. Jungk, a. T. Wolf, S. Cray, T. Easton, a. Mountney, S. Leadley, S. H. Chao, a. Colas, F. de Buyl, a. Dupont, J. L. Garaud, F. Gubbels, J. P. Lecomte, B. Lenoble, S. Stassen, C. Stevens, X. Thomas, and G. Shearer, "Silicones in Industrial Applications," *Inorg. Polym.*, pp. 61–161, 2007.

[159] L. Miao, P. Jin, K. Kaneko, a Terai, N. Nabatova-Gabain, and S. Tanemura, "Preparation and characterization of polycrystalline anatase and rutile TiO2 thin films by rf magnetron sputtering," *Appl. Surf. Sci.*, vol. 212–213, pp. 255–263, May 2003.

[160] A. Di Paola, G. Cufalo, M. Addamo, M. Bellardita, R. Campostrini, M. Ischia, R. Ceccato, and L. Palmisano, "Photocatalytic activity of nanocrystalline TiO2 (brookite, rutile and brookite-based) powders prepared by thermohydrolysis of TiCl4 in aqueous chloride solutions," *Colloids Surfaces A Physicochem. Eng. Asp.*, vol. 317, no. 1–3, pp. 366–376, Mar. 2008.

[161] Y. Liu, Z. Lin, Z. Zhao, C.-C. C. Tuan, K. S. Moon, S. Yoo, J. Choi, C. P. Wong, X. Zhao, C.-C. C. Tuan, K. S. Moon, S. Yoo, M. G. Jang, and C. P. Wong, "High Refractive Index and Transparent Nanocomposites as Encapsulant for High Brightness LED Packaging," *Trans. Components, Packag. Manuf. Technol.*, vol. 4,

no. 7, pp. 1125–1130, 2014.

[162] J. Brandrup, E. H. Immergut, and E. A. Grulke, *Polymer handbook*. Wiley-Interscience, 2003.

[163] H. Fox, P. Taylor, and W. Zisman, "Polyorganosiloxanes...Surface Active Properties," *Ind. Eng. Chem.*, vol. 39, no. 11, pp. 1401–1409, Nov. 1947.

[164] Y. Liu, Z. Lin, Z. Zhao, C.-C. Tuan, K.-S. Moon, S. Yoo, J. Choi, C.-P. P. Wong, X. Zhao, and M.-G. Jang, "High Refractive Index and Transparent Nanocomposites as Encapsulant for High Brightness LED Packaging," *Trans. Components, Packag. Manuf. Technol.*, vol. 4, no. 7, pp. 1125–1130, Jul. 2014.

[165] N. M. Kovalchuk, A. Trybala, V. Starov, O. Matar, and N. Ivanova, "Fluoro- vs hydrocarbon surfactants: Why do they differ in wetting performance?," *Adv. Colloid Interface Sci.*, vol. 210, pp. 65–71, Aug. 2014.

[166] J. Millette, D. S. Scott, D. Radlein, J. Piskorz, P. Majerski, I. G. Reilly, and T. J. W. Debruijn, "Surface Tensions of Hydrocarbons and Bitumens at High Temperatures and Pressures," *Can. J. Chem. Eng.*, vol. 82, no. 5, pp. 1004–1013, May 2008.

[167] T. Darmanin and F. Guittard, "Fluorophobic Effect for Building up the Surface Morphology of Electrodeposited Substituted Conductive Polymers," *Langmuir*, vol. 25, no. 10, pp. 5463–5466, May 2009.

[168] D. M. Lemal, "Perspective on Fluorocarbon Chemistry," *J. Org. Chem.*, vol. 69, no.

1, pp. 1–11, 2004.

[169] S. Alexander, G. N. Smith, C. James, S. E. Rogers, F. Guittard, M. Sagisaka, and J. Eastoe, “Low-Surface Energy Surfactants with Branched Hydrocarbon Architectures,” *Langmuir*, vol. 30, no. 12, pp. 3413–3421, Apr. 2014.

[170] T. Nishino, M. Meguro, K. Nakamae, M. Matsushita, and Y. Ueda, “The Lowest Surface Free Energy Based on -CF3 Alignment,” *Langmuir*, vol. 15, no. 13, pp. 4321–4323, Jun. 1999.

[171] S. Alexander, J. Eastoe, A. M. Lord, F. Guittard, and A. R. Barron, “Branched Hydrocarbon Low Surface Energy Materials for Superhydrophobic Nanoparticle Derived Surfaces,” *ACS Appl. Mater. Interfaces*, vol. 8, no. 1, pp. 660–666, Jan. 2016.

[172] W. A. ZISMAN, “Relation of the Equilibrium Contact Angle to Liquid and Solid Constitution,” in *Contact Angle, Wettability, and Adhesion*, 1964, pp. 1–51.

[173] F. W. Mont, J. K. Kim, M. F. Schubert, E. F. Schubert, and R. W. Siegel, “High-refractive-index TiO2-nanoparticle-loaded encapsulants for light-emitting diodes,” *J. Appl. Phys.*, vol. 103, no. 8, p. 83120, Apr. 2008.

[174] C. P. Wong, “MICROELECTRONICS: Flip the Chip,” *Science*, vol. 290, no. 5500, pp. 2269–2270, Dec. 2000.

[175] K. M. F. Shahil and A. A. Balandin, “Graphene-multilayer graphene

nanocomposites as highly efficient thermal interface materials.," *Nano Lett.*, vol. 12, no. 2, pp. 861–7, Feb. 2012.

[176] R. Zhang, W. Lin, K. Lawrence, and C. P. Wong, "Highly reliable, low cost, isotropically conductive adhesives filled with Ag-coated Cu flakes for electronic packaging applications," *Int. J. Adhes. Adhes.*, vol. 30, no. 6, pp. 403–407, Sep. 2010.

[177] H. Zou, S. Wu, and J. Shen, "Polymer/Silica Nanocomposites: Preparation, Characterization, Properties, and Applications," *Chem. Rev.*, vol. 108, no. 9, pp. 3893–3957, Sep. 2008.

[178] C. P. Wong and R. S. Bollampally, "Thermal conductivity, elastic modulus, and coefficient of thermal expansion of polymer composites filled with ceramic particles for electronic packaging," *J. Appl. Polym. Sci.*, vol. 74, pp. 3396–3403, 1999.

[179] S. Kang, S. Il Hong, C. R. Choe, M. Park, S. Rim, and J. Kim, "Preparation and characterization of epoxy composites filled with functionalized nanosilica particles obtained via sol–gel process," *Polymer*, vol. 42, no. 3, pp. 879–887, 2001.

[180] S. Sprenger, "Epoxy resin composites with surface-modified silicon dioxide nanoparticles: A review," *J. Appl. Polym. Sci.*, vol. 130, no. 3, pp. 1421–1428, 2013.

[181] Q. Guo, P. Zhu, G. Li, L. Huang, Y. Zhang, D. D. Lu, R. Sun, and C. Wong, "One-pot synthesis of bimodal silica nanospheres and their effects on the rheological and thermal–mechanical properties of silica–epoxy composites," *RSC Adv.*, vol. 5, no.

62, pp. 50073–50081, 2015.

[182] C.-C. Tuan, N. P. James, Z. Lin, Y. Chen, Y. Liu, K.-S. Moon, Z. Li, and C. P. Wong, "Self-Patterning of Silica/Epoxy Nanocomposite Underfill by Tailored Hydrophilic-Superhydrophobic Surfaces for 3D Integrated Circuit (IC) Stacking," *ACS Appl. Mater. Interfaces*, vol. 9, no. 10, pp. 8437–8442, Mar. 2017.

[183] J. Jancar, "Review of the role of the interphase in the control of composite performance on micro- and nano-length scales," *J. Mater. Sci.*, vol. 43, no. 20, pp. 6747–6757, 2008.

[184] V. Hristov and J. Vlachopoulos, "Effects of polymer molecular weight and filler particle size on flow behavior of wood polymer composites," *Polym. Compos.*, vol. 29, no. 8, pp. 831–839, Aug. 2008.

[185] R. S. Tate, D. S. Fryer, S. Paqualini, M. F. Montague, J. J. De Pablo, and P. F. Nealey, "Extraordinary elevation of the glass transition temperature of thin polymer films grafted to silicon oxide substrates," *J. Chem. Phys.*, vol. 115, no. 21, pp. 9982–9990, 2001.

[186] J. Moll and S. K. Kumar, "Glass Transitions in Highly Attractive Highly Filled Polymer Nanocomposites," *Macromolecules*, vol. 45, no. 2, pp. 1131–1135, Jan. 2012.

[187] Z. Wang, Q. Lv, S. Chen, C. Li, S. Sun, and S. Hu, "Effect of Interfacial Bonding on Interphase Properties in SiO2/Epoxy Nanocomposite: A Molecular Dynamics

Simulation Study," *ACS Appl. Mater. Interfaces*, vol. 8, no. 11, pp. 7499–7508, Mar. 2016.

[188] T. Kawaguchi and R. A. Pearson, "The effect of particle-matrix adhesion on the mechanical behavior of glass filled epoxies: Part 1. A study on yield behavior and cohesive strength," *Polymer*, vol. 44, no. 15, pp. 4229–4238, 2003.

[189] L. J. Broutman and B. Das Agarwal, "A theoretical study of the effect of an interfacial layer on the properties of composites," *Polym. Eng. Sci.*, vol. 14, no. 8, pp. 581–588, Aug. 1974.

[190] I. Zaman, T. T. Phan, H. C. Kuan, Q. Meng, L. T. Bao La, L. Luong, O. Youssf, and J. Ma, "Epoxy/graphene platelets nanocomposites with two levels of interface strength," *Polymer*, vol. 52, no. 7, pp. 1603–1611, 2011.

[191] I. Luzinov, D. Julthongpiput, A. Liebmann-Vinson, T. Cregger, M. D. Foster, and V. V Tsukruk, "Epoxy-Terminated Self-Assembled Monolayers: Molecular Glues for Polymer Layers," *Langmuir*, vol. 16, no. 2, pp. 504–516, Jan. 2000.

[192] A. Zengin and T. Caykara, "Formation and properties of surface-anchored amine-terminated poly(dimethylsiloxane) assemblies with tunable physico-chemical characteristics," *Thin Solid Films*, vol. 519, no. 10, pp. 3135–3140, 2011.

[193] F. M. Wisser, M. Abele, M. Gasthauer, K. M??ller, N. Moszner, and G. Kickelbick, "Detection of surface silanol groups on pristine and functionalized silica mixed oxides and zirconia," *J. Colloid Interface Sci.*, vol. 374, no. 1, pp. 77–82, 2012.

[194] M. Patel, W. Feng, K. Savaram, M. R. Khoshi, R. Huang, J. Sun, E. Rabie, C. Flach, R. Mendelsohn, E. Garfunkel, and H. He, "Microwave Enabled One-Pot, One-Step Fabrication and Nitrogen Doping of Holey Graphene Oxide for Catalytic Applications," *Small*, vol. 11, no. 27, pp. 3358–3368, Jul. 2015.

[195] M. Zhao, L. Meng, L. Ma, G. Wu, Y. Wang, F. Xie, and Y. Huang, "Interfacially reinforced carbon fiber/epoxy composites by grafting melamine onto carbon fibers in supercritical methanol," *RSC Adv.*, vol. 6, no. 35, pp. 29654–29662, 2016.

[196] R. Rohini and S. Bose, "Tailored interface and enhanced elastic modulus in epoxy-based composites in presence of branched poly(ethyleneimine) grafted multiwall carbon nanotubes," *Phys. Chem. Chem. Phys.*, vol. 17, no. 12, pp. 7907–7913, 2015.

[197] B. Kim, J. Choi, S. Yang, S. Yu, and M. Cho, "Influence of crosslink density on the interfacial characteristics of epoxy nanocomposites," *Polymer*, vol. 60, pp. 186–197, Mar. 2015.

[198] A. Reuss, "Berechnung der Fließgrenze von Mischkristallen auf Grund der Plastizitätsbedingung für Einkristalle," *ZAMM - Zeitschrift für Angew. Math. und Mech.*, vol. 9, no. 1, pp. 49–58, 1929.

[199] P. S. Turner, "Thermal-expansion stresses in reinforced plastics," *J. Res. Natl. Bur. Stand.*, vol. 37, no. 4, p. 239, Oct. 1946.

[200] R. A. Schapery, "Thermal Expansion Coefficients of Composite Materials Based on Energy Principles," *J. Compos. Mater.*, vol. 2, no. 3, pp. 380–404, Jul. 1968.

[201] C. Karch, “Micromechanical Analysis of Thermal Expansion Coefficients,” *Model. Numer. Simul. Mater. Sci.*, vol. 4, no. 3, pp. 104–118, 2014.

[202] Z. Hashin and S. Shtrikman, “A variational approach to the theory of the elastic behaviour of multiphase materials,” *J. Mech. Phys. Solids*, vol. 11, no. 2, pp. 127–140, 1963.

[203] L. Shen, L. Wang, T. Liu, and C. He, “Nanoindentation and morphological studies of epoxy nanocomposites,” *Macromol. Mater. Eng.*, vol. 291, no. 11, pp. 1358–1366, 2006.

[204] R. Lach, L. Antonova Gyurova, and W. Grellmann, “Application of indentation fracture mechanics approach for determination of fracture toughness of brittle polymer systems,” *Polym. Test.*, vol. 26, no. 1, pp. 51–59, 2007.

[205] J. Choi, C. M. Hui, J. Pietrasik, H. Dong, K. Matyjaszewski, and M. R. Bockstaller, “Toughening fragile matter: mechanical properties of particle solids assembled from polymer-grafted hybrid particles synthesized by ATRP,” *Soft Matter*, vol. 8, no. 15, p. 4072, 2012.

[206] C. Oliver and M. Pharr, “An improved technique for determining hardness and elastic modulus using load and displacement sensing indentation experiments,” *Journal of Materials Research*, vol. 7, no. 11. pp. 1564–1583, 1992.

[207] W. C. Oliver and G. M. Pharr, “Measurement of hardness and elastic modulus by instrumented indentation: Advances in understanding and refinements to

methodology," *J. Mater. Res.*, vol. 19, no. 1, pp. 3–20, 2004.

[208] M. Krumova, A. Flores, F. J. Baltá Calleja, and S. Fakirov, "Elastic properties of oriented polymers, blends and reinforced composites using the microindentation technique," *Colloid Polym. Sci.*, vol. 280, no. 7, pp. 591–598, 2002.

[209] D. B. Marshall, B. R. Lawn, and A. G. Evans, "Elastic/Plastic Indentation Damage in Ceramics: The Lateral Crack System," *J. Am. Ceram. Soc.*, vol. 65, no. 11, pp. 561–566, Nov. 1982.

[210] Y. Zamani Ketek Lahijania, M. Mohseni, and S. Bastani, "Characterization of mechanical behavior of UV cured urethane acrylate nanocomposite films loaded with silane treated nanosilica by the aid of nanoindentation and nanoscratch experiments," *Tribol. Int.*, vol. 69, pp. 10–18, 2014.

[211] M. M. Shokrieh, M. R. Hosseinkhani, M. R. Naimi-Jamal, and H. Tourani, "Nanoindentation and nanoscratch investigations on graphene-based nanocomposites," *Polym. Test.*, vol. 32, no. 1, pp. 45–51, 2013.

[212] G. Chitnis, Z. Ding, C.-L. Chang, C. A. Savran, and B. Ziaie, "Laser-treated hydrophobic paper: an inexpensive microfluidic platform," *Lab Chip*, vol. 11, no. 6, p. 1161, 2011.

[213] A. Dev, B. Dev Choudhury, A. Abedin, and S. Anand, "Fabrication of Periodic Nanostructure Assemblies by Interfacial Energy Driven Colloidal Lithography," *Adv. Funct. Mater.*, vol. 24, no. 29, pp. 4577–4583, Aug. 2014.

[214] X. Han, J. Hou, J. Xie, J. Yin, Y. Tong, C. Lu, and H. Möhwald, "Synergism of Dewetting and Self-Wrinkling To Create Two-Dimensional Ordered Arrays of Functional Microspheres," *ACS Appl. Mater. Interfaces*, vol. 8, no. 25, pp. 16404–16411, 2016.

[215] E. Ueda and P. A. Levkin, "Emerging applications of superhydrophilic-superhydrophobic micropatterns," *Adv. Mater.*, vol. 25, no. 9, pp. 1234–1247, 2013.

[216] J. H. Lau, S. W. Ricky Lee, and C. Chang, "Effects of underfill material properties on the reliability of solder bumped flip chip on board with imperfect underfill encapsulants," *IEEE Trans. Components Packag. Technol.*, vol. 23, no. 2, pp. 323–333, 2000.

[217] R. R. Tummala and M. Swaminathan, *Introduction to system-on-package (SOP): miniaturization of the entire system*. McGraw-Hill, 2008.

[218] J. H. Lau, "Overview and Outlook of Three-Dimensional Integrated Circuit Packaging, Three-Dimensional Si Integration, and Three-Dimensional Integrated Circuit Integration," *J. Electron. Packag.*, vol. 136, no. 4, p. 40801, Oct. 2014.

[219] J. W. Wan, W. J. Zhang, and D. J. Bergstrom, "A Theoretical Analysis of the Concept of Critical Clearance Toward a Design Methodology for the Flip-Chip Package," *J. Electron. Packag.*, vol. 129, no. 4, p. 473, 2007.

[220] J. W. Wan, W. J. Zhang, and D. J. Bergstrom, "Experimental verification of models for underfill flow driven by capillary forces in flip-chip packaging," *Microelectron.*

Reliab., vol. 48, no. 3, pp. 425–430, Mar. 2008.

[221] T. J. Spencer, T. Osborn, and P. A. Kohl, "High-Frequency Chip Connections," *Science*, vol. 320, no. 5877, pp. 756–757, May 2008.

[222] Z. Zhang and C. P. Wong, "Flip-chip underfill: Materials, process and reliability," *Mater. Adv. Packag.*, vol. 27, no. 3, pp. 307–337, 2009.

[223] K. Gross, S. Hackett, W. Schultz, and W. Thompson, "Nanocomposite underfills for flip-chip applications," in *53rd Electronic Components and Technology Conference, 2003. Proceedings.*, 2003, pp. 951–956.

[224] Y. Sun, Z. Zhang, and C. P. Wong, "Study on mono-dispersed nano-size silica by surface modification for underfill applications.," *J. Colloid Interface Sci.*, vol. 292, no. 2, pp. 436–44, Dec. 2005.

[225] T. Nonaka, S. Niizeki, N. Asahi, and K. Fujimaru, "Low temperature touch down and suppressing filler trapping bonding process with a wafer level pre-applied underfilling film adhesive," in *2012 IEEE 62nd Electronic Components and Technology Conference*, 2012, pp. 444–449.

[226] R. Ghaffarian, "Characterization and failure analyses of lead-free solder defects," in *Lead-free Solder Interconnect Reliability*, 1st ed., Materials Park, OH: ASM International, 2005, pp. 227–248.

[227] C. E. Stauffer, "The Measurement of Surface Tension by the Pendant Drop

Technique," *J. Phys. Chem*, vol. 69, no. 6, pp. 1933–1938, Jun. 1965.

[228] Y. Rotenberg, L. Boruvka, and A. W. Neumann, "Determination of surface tension and contact angle from the shapes of axisymmetric fluid interfaces," *J. Colloid Interface Sci.*, vol. 93, no. 1, pp. 169–183, 1983.

[229] Y. Yuan and T. R. Lee, "Contact Angle and Wetting Properties," in *Surface Science Techniques*, Springer Berlin Heidelberg, 2013, pp. 3–34.

[230] B. Zhao, J. S. Moore, and D. J. Beebe, "Surface-Directed Liquid Flow Inside Microchannels," *Science*, vol. 291, no. 5506, pp. 1023–1026, Feb. 2001.

[231] A. Lafuma and D. Quéré, "Superhydrophobic states," *Nat. Mater.*, vol. 2, no. 7, pp. 457–60, Jul. 2003.

[232] J. Ou, W. Hu, S. Liu, M. Xue, F. Wang, and W. Li, "Superoleophobic textured copper surfaces fabricated by chemical etching/oxidation and surface fluorination.," *ACS Appl. Mater. Interfaces*, vol. 5, no. 20, pp. 10035–41, Oct. 2013.

[233] F. Zhang, W. Bin Zhang, Z. Shi, D. Wang, J. Jin, and L. Jiang, "Nanowire-Haired Inorganic Membranes with Superhydrophilicity and Underwater Ultralow Adhesive Superoleophobicity for High-Efficiency Oil/Water Separation," *Adv. Mater.*, vol. 25, no. 30, pp. 4192–4198, Aug. 2013.

[234] J. Yang, Z. Zhang, X. Men, X. Xu, and X. Zhu, "A simple approach to fabricate superoleophobic coatings," *New J. Chem.*, vol. 35, no. 3, pp. 576–580, Sep. 2011.

[235] M. C. Biesinger, B. P. Payne, A. P. Grosvenor, L. W. M. Lau, A. R. Gerson, and R. S. C. Smart, "Resolving surface chemical states in XPS analysis of first row transition metals, oxides and hydroxides: Cr, Mn, Fe, Co and Ni," *Appl. Surf. Sci.*, vol. 257, no. 7, pp. 2717–2730, 2011.

[236] P. Keil, R. Frahm, and D. Lützenkirchen-Hecht, "Native oxidation of sputter deposited polycrystalline copper thin films during short and long exposure times: Comparative investigation by specular and non-specular grazing incidence X-ray absorption spectroscopy," *Corros. Sci.*, vol. 52, no. 4, pp. 1305–1316, Apr. 2010.

[237] E. Hoque, J. A. Derose, R. Houriet, P. Hoffmann, and H. J. Mathieu, "Stable perfluorosilane self-assembled monolayers on copper oxide surfaces: Evidence of siloxy-copper bond formation," *Chem. Mater.*, vol. 19, no. 4, pp. 798–804, 2007.

[238] E. Hoque, J. A. DeRose, P. Hoffmann, and H. J. Mathieu, "Robust perfluorosilanized copper surfaces," *Surf. Interface Anal.*, vol. 38, no. 2, pp. 62–68, Feb. 2006.

[239] P. Fine, B. Cobb, and L. Nguyen, "Flip chip underfill flow characteristics and prediction," *IEEE Trans. Components Packag. Technol.*, vol. 23, no. 3, pp. 420–427, 2000.

[240] D. R. Gamota and C. M. Melton, "Advanced encapsulant materials systems for flip-chip-on-board assemblies. I. Encapsulant materials with improved manufacturing properties. II. Materials to integrate the reflow and underfilling processes," in

Nineteenth IEEE/CPMT International Electronics Manufacturing Technology Symposium, 1996, pp. 1–9.

[241] L. Zheng and Ying Sun, "An Examination of Underfill Flow in Large Dies With Nonuniform Bump Patterns," *IEEE Trans. Components Packag. Technol.*, vol. 33, no. 1, pp. 196–205, Mar. 2010.

[242] Shijian Luo and C. P. Wong, "Effect of UV/ozone treatment on surface tension and adhesion in electronic packaging," *IEEE Trans. Components Packag. Technol.*, vol. 24, no. 1, pp. 43–49, Mar. 2001.

[243] S. H. Lee, H. J. Lee, J.-M. Kim, and Y. E. Shin, "Dynamic Filling Characteristics of a Capillary Driven Underfill Process in Flip-Chip Packaging," *Mater. Trans.*, vol. 52, no. 10, pp. 1998–2003, 2011.

[244] Y. Huang, D. Bigio, and M. G. Pecht, "Fill Pattern and Particle Distribution of Underfill Material," *IEEE Trans. Components Packag. Technol.*, vol. 27, no. 3, pp. 493–498, Sep. 2004.

[245] D. P. Singh, A. K. Ojha, and O. N. Srivastava, "Synthesis of Different Cu(OH)2 and CuO (Nanowires, Rectangles, Seed-, Belt-, and Sheetlike) Nanostructures by Simple Wet Chemical Route," *J. Phys. Chem. C*, vol. 113, no. 9, pp. 3409–3418, Mar. 2009.

[246] E. Cano, C. L. Torres, and J. M. Bastidas, "An XPS study of copper corrosion originated by formic acid vapour at 40% and 80% relative humidity," *Mater. Corros.*, vol. 52, no. 9, pp. 667–676, Sep. 2001.

[247] R. W. Johnson, J. L. Evans, P. Jacobsen, J. R. Thompson, and M. Christopher, "The changing automotive environment: High-temperature electronics," *IEEE Trans. Electron. Packag. Manuf.*, vol. 27, no. 3, pp. 164–176, 2004.

[248] A. Hale, C. W. Macosko, and H. E. Bair, "Glass transition temperature as a function of conversion in thermosetting polymers," *Macromolecules*, vol. 24, no. 9, pp. 2610–2621, Apr. 1991.

[249] H. Ali-Asgari Dehaghi, S. Mazinani, D. Zaarei, M. Kalaee, H. Jabari, and N. Sedaghat, "Thermal and morphological characteristics of solution blended epoxy/NBR compound," *J. Therm. Anal. Calorim.*, vol. 114, no. 1, pp. 185–194, Oct. 2013.

[250] C. H. Lin, Y. C. Chou, W. F. Shiao, and M. W. Wang, "High temperature, flame-retardant, and transparent epoxy thermosets prepared from an acetovanillone-based hydroxyl poly(ether sulfone) and commercial epoxy resins," *Polymer*, vol. 97, pp. 300–308, Aug. 2016.

[251] S. Barrau, P. Demont, C. Maraval, A. Bernes, and C. Lacabanne, "Glass Transition Temperature Depression at the Percolation Threshold in Carbon Nanotube-Epoxy Resin and Polypyrrole-Epoxy Resin Composites," *Macromol. Rapid Commun.*, vol. 26, no. 5, pp. 390–394, Mar. 2005.

[252] G. Yu, C. Liu, J. Wang, X. Li, and X. Jian, "Heat-resistant aromatic S-triazine-containing ring-chain polymers based on bis(ether nitrile)s: Synthesis and

properties," *Polym. Degrad. Stab.*, vol. 95, no. 12, pp. 2445–2452, 2010.

[253] D. R. Anderson, J. M. Holovka, and X. Corporation, "Thermally Resistant Polymers Containing the s-Triazine Ring," *J. Polym. Sci. Part A Polym. Chem.*, vol. 4, pp. 1689–1702, 1966.

[254] X. Sheng, M. Akinc, and M. R. Kessler, "Cure kinetics of thermosetting bisphenol E cyanate ester," *J. Therm. Anal. Calorim.*, vol. 93, no. 1, pp. 77–85, 2008.

[255] D. A. Shimp, "Technologically driven applications for cyanate ester resins," in *Chemistry and Technology of Cyanate Ester Resins*, Dordrecht: Springer Netherlands, 1994, pp. 282–327.